GEOCHEMISTRY AND PETROLOGY OF LAVAS FROM THE MANUS BASIN EXTENSIONAL TRANSFORM ZONE AND MANUS SPREADING CENTER: IMPLICATIONS FOR SOURCE COMPOSITIONS AND METASOMATIC PROCESSES IN BACK-ARC BASINS

A THESIS SUBMITTED TO THE GRADUATE DIVISION OF THE UNIVERSITY OF HAWAII IN PARTIAL FULFILLMENT OF THE REQUIREMENTS FOR THE DEGREE OF

MASTER OF SCIENCE

IN GEOLOGY AND GEOPHYSICS

MAY 1989

By

Lori Ann S.M. Liu

Thesis Committee:

John M. Sinton, Chairman
Michael O. Garcia
Brian Taylor

We certify that we have read this thesis and that, in our opinion, it is satisfactory in scope and quality as a thesis for the degree of Master of Science in Geology and Geophysics.

THESIS COMMITTEE

_____
Chairman

_____

_____

ACKNOWLEDGEMENTS

This study is part of the Manus Back-Arc Basin Project that was initiated by Brian Taylor and John Sinton. Special thanks to John Sinton, for giving me the opportunity to work on a great project such as the Manus Basin. His enthusiasm got me interested in the project and his knowledge and guidance kept me on the right track.

I also want to thank my committee members, Mike Garcia and Brian Taylor, for their assistance. Tom Benke and Jill Mahoney helped in the sample preparation process. Gail Yamada and JoAnn Sinton made the majority of thin sections. Tom Tatnall provided photography services.

I would also like to thank Bruce Chappell at the Australian National University for XRF and INAA analyses and making his laboratories open to me. Thanks are also due to the various HIG and ANU faculty, students, and staff who have helped in many ways, especially discussions with and/or assistance from Rob Yonover, Bob Mallonee, Gordon Tribble, Suki Smaglik, Keith Crook, and Crisse Pratt.

A very special thanks to Bob Harman, who put up with the often frustrating trip to obtaining a post-graduate degree.

This study was funded by NSF grants OCE-8511288 and OCE-8723036.

ABSTRACT

Lavas representative of three distinct types of magma occur in the Manus Basin, a back-arc basin in the eastern Bismarck Sea. Lavas with geochemical characteristics similar to those of the island arc association are erupted from tectonic features situated closest to the active arc. Farther from the active arc, lavas similar to those from mid-ocean ridges (MORB) and back-arc basins (BABB) are erupted. Manus MORB lavas are compositionally similar to normal-MORB (N-MORB), but have even lower concentrations of incompatible elements, especially TiO_2, K_2O, Al_2O_3, Sr, and Ba. Manus BABB lavas have higher concentrations of incompatible elements, especially K_2O, Al_2O_3, Rb, Sr, Ba, LREE and H_2O, and lower concentrations of FeO^* and TiO_2 compared to Manus MORB.

Relative to the source for Manus MORB, the source for Manus BABB is enriched in Rb > Ba > K > La > Sr, and depleted in Yb > Y > Zr > V > Ti. An unusual lava type with extreme enrichments in large ion lithophile elements and H_2O occurs on the shoalest portion of the Manus Spreading Center. The element enrichments in this lava type (X-BABB) are similar to those in BABB except that Zr is enriched in X-BABB relative to MORB. The order of element enrichment in BABB is similar to that in aqueous fluids. Interaction between aqueous fluids derived from the shallow part of the subducted lithospheric slab and the overlying mantle probably produced peridotites containing hydrous veins. Melting of this veined peridotite could lead to the generation of Manus BABB with its characteristic element enrichments.

An evaluation of the major element compositions of Manus MORB and BABB suggests that Manus BABB are the result of higher extents of (hydrous) melting at lower pressures than Manus MORB. This indicates that BABB diapirs

rise along cooler adiabats than those for Manus MORB. If higher extents of melting correlate with crustal thickness, the preferential eruption of Manus BABB at shoaler depths than Manus MORB can be attributed to the higher extents of melting for Manus BABB.

TABLE OF CONTENTS

LIST OF TABLES

LIST OF ILLUSTRATIONS

I. INTRODUCTION

The Manus Basin is the only currently active site of fast back-arc spreading. It is an ideal area in which to study tectonic and petrologic evolution, and magma genesis in a fast-spreading back-arc basin. Previous geophysical data collected from the Manus Basin are poor quality. There have been no extensive attempts to recover volcanic samples from the Manus Basin. This study represents the first investigation of magmas related to various styles of spreading (Mallonee, 1989) in the Manus Back-Arc Basin.

GENERAL SETTING OF THE BISMARCK SEA

The Bismarck Sea is composed of several major tectonic elements. Since the mid-Eocene (45 Ma), Papua New Guinea, the Manus Trench, New Ireland, Djaul Island, Manus Island, the Solomon Islands, New Britain, the Ontong Java Plateau, the New Britain Trench, the Solomon Sea Plate, the Indo-Australian Plate and the Pacific Plate have all interacted, directly or indirectly, to produce the Bismarck Sea (Fig.1). Falvey and Pritchard (1985), working with paleomagnetic data, suggested that the New Britain Arc, the Huon Peninsula, Manus Island, and the North Solomon Islands formed a mid-Eocene arc (Fig.2). Between 45 and 39 Ma, this arc rotated about 75^{o} counter-clockwise to form a new arc that was almost perpendicular to the northeast coast of Papua New Guinea. About 30 Ma, New Britain, the Huon Peninsula, and the Manus Island Arc rotated clockwise about 60^{o} to form a nearly straight line with the North Solomon Islands Arc (Falvey and Pritchard, 1985).

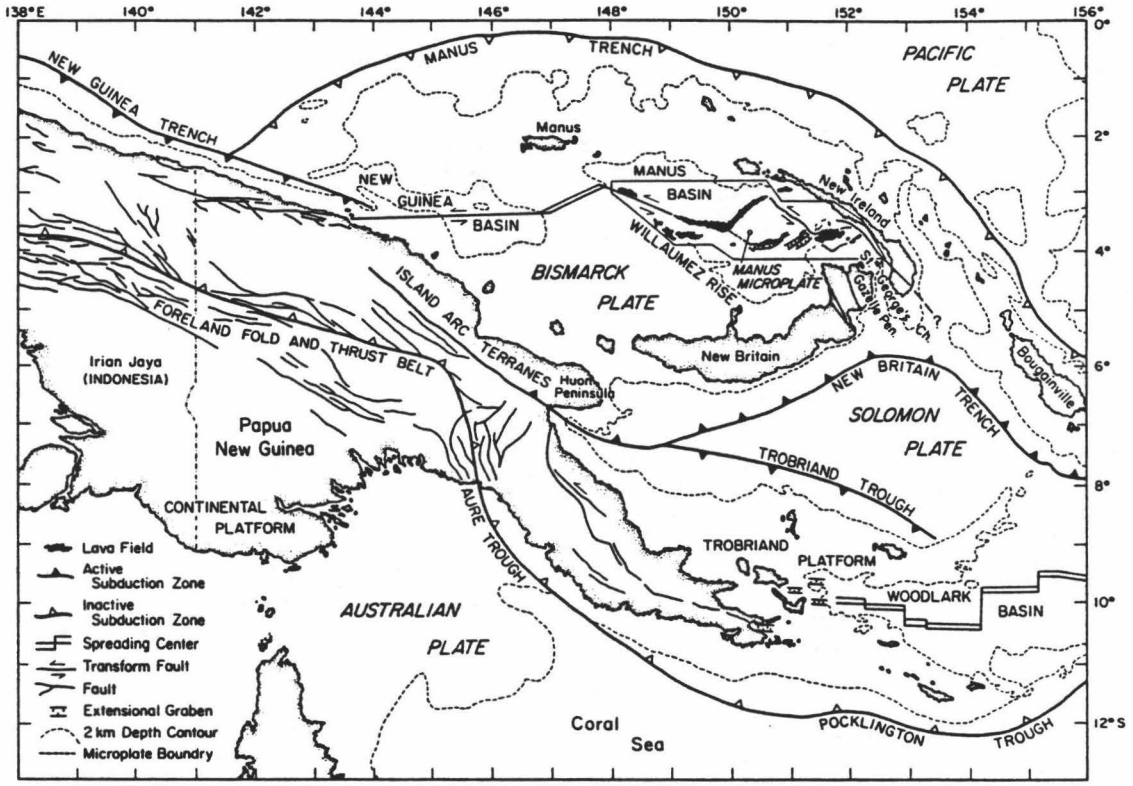

Figure 1. Tectonic features of Western Melanesia. The Manus Basin, in the northeastern Bismarck Sea, is a back-arc basin associated with the active New Britain Arc. Survey area of the Manus Basin is enclosed, showing the extent of lava fields, transforms, and grabens (From Mallonee, 1989).

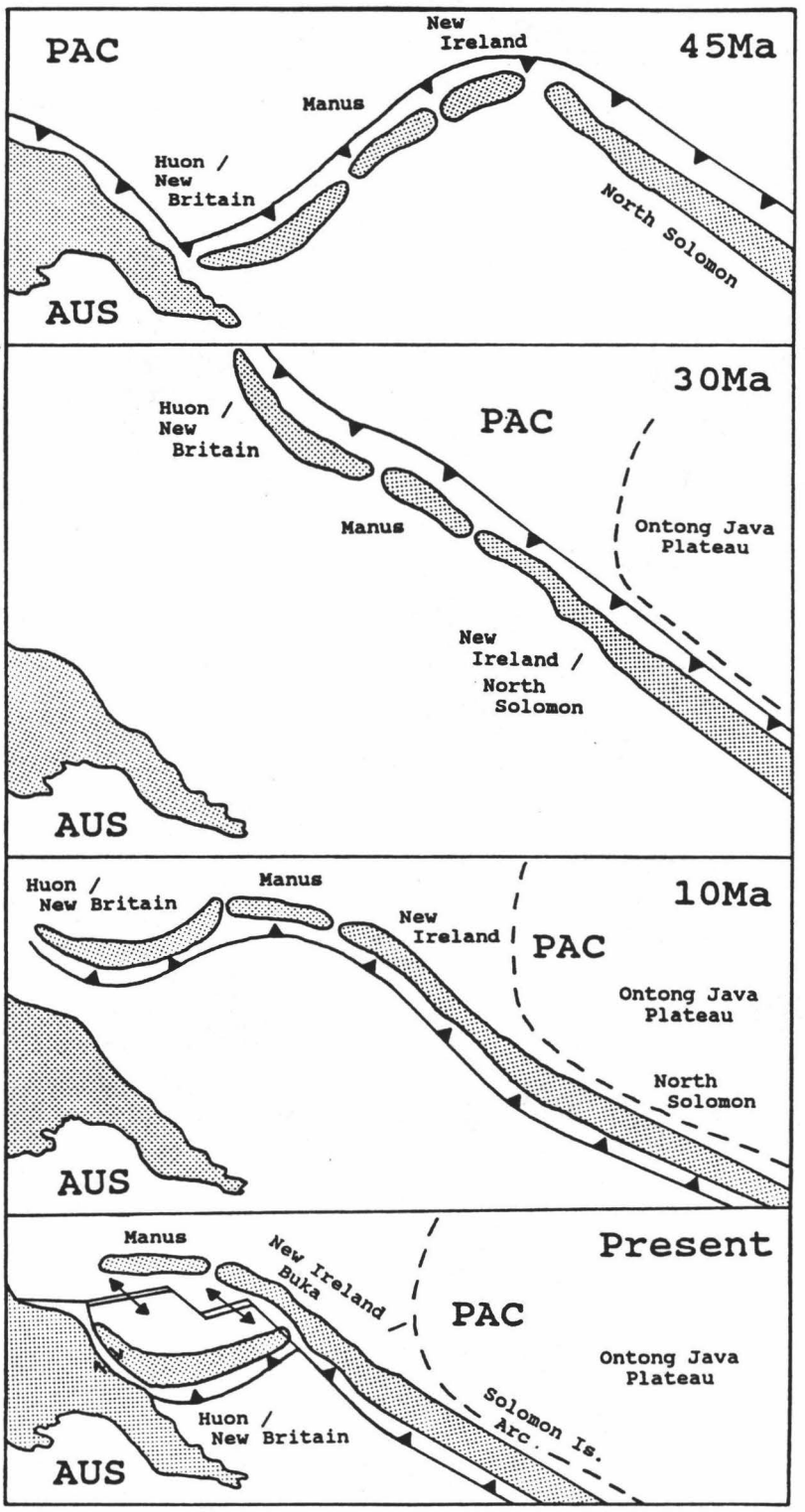

Figure 2. Diagrammatic interpretation of the tectonic evolution of the Bismarck Sea and adjacent areas, from 45 million years ago to the present (After Falvey and Pritchard, 1985).

About 10 Ma, the Ontong Java Plateau collided with New Ireland and the North Solomon Island Arc, and subduction of the Pacific Plate beneath this arc ended (Ripper and McCue, 1983; Cooper and Taylor, 1987). At the same time, a counter-clockwise rotation of the New Ireland/North Solomon Arc and an associated subduction reversal occurred (Ripper and McCue, 1983). This reversal was accomodated by subduction of the Solomon Sea Plate beneath the Pacific and Indo-Australian Plates, along what is now known as the New Britain Trench (late Miocene). About 4 Ma, the composite New Britain/Huon Peninsula Arc rotated counter-clockwise to form the Bismarck Sea (Falvey and Pritchard, 1985).

A band of shallow-level seismicity has been described from earthquake studies in the Papua New Guinea-Solomon Islands region. This seismic lineation forms an arcuate east-west trend across the Bismarck Sea, and could be associated with either an "embryo mid-ocean ridge or trench", or a fault lineation (Denham, 1969). Connelly (1974) suggested that sea-floor extension occurred, but it was not related directly to the Bismarck Sea seismic lineation. Johnson and Molnar (1972) and Krause (1973) speculated that the lineation represented the boundary between two microplates, and that it is a left-lateral strike-slip fault. Malahoff and Bracey (1974) suggested that it is a spreading center. Connelly (1976) also suggested that sea-floor spreading is associated with the Bismarck Sea lineation, but that the processes are not similar to conventional mid-ocean ridges. Taylor (1979) recognized the existence of sea-floor spreading in the Manus Basin, and that this spreading occurred along one of four segments that composed the Bismarck Sea lineation.

TECTONIC FEATURES OF THE MANUS BASIN

The Manus Basin is a back-arc basin (small ocean basin behind an island arc, Watts et al., 1977) in the eastern Bismarck Sea. It lies between the Willaumez Rise and the islands of New Britain, New Ireland and New Hanover (Fig.1). The basin consists of seven main tectonic features, four of which have fresh lava outcrops (Fig.3). These features are described briefly below and are labeled in Figure 3.

The eastern Manus Basin is dominated by *en echelon* rifts (subparallel rifts arranged along a linear zone), the East Manus Ridges. The East Manus Ridges are bounded by two left-lateral transform faults, the Weitin Fault and its offshore extension to the east, and the Djaul Transform Fault to the west (Fig.3). The Ridges lie between the islands of New Britain and New Ireland in water depths less than about 2000 m. The East Manus Ridges do not show well-defined tectonic features. Thus rifting and seafloor spreading may be poorly-organized. The extent of lava fields shown on Figure 3 indicates this region is volcanically moderately active. West of the Djaul Transform Fault are the Southern Rifts, consisting of two overlapping rift grabens and an active seamount. The deep basins and the lack of extensive lava fields indicate that the Southern Rifts must have a low magmatic budget, caused by either the commencement of very young/new rifts or the dying of old rifts. Magnetic lineations in this area indicate either a recent pulse of rapid spreading or a long period of slow spreading (R. Mallonee, pers. comm.), also indicative of either young or old rifts, respectively. Water depths to the Southern Rifts range from 2045-2635 m.

The dominant spreading and volcanic lineament in the Manus Basin is the Manus Spreading Center (MSC). This spreading center may be oblique to, and

Figure 3. SeaMARC II side scan sonar mosaic (top) and interpretation (bottom) of the Manus Basin. Lava fields are shaded on the bottom figure. Localities mentioned in the text include the East Manus Ridges (ER), Southern Rifts (SR), Manus Spreading Center (MSC), Extensional Transform Zone (ETZ), and the Willaumez Transform Fault (WTF). In addition, the Weitin Fault (WF) and Djaul Transform Fault (DTF) are included in the figure.

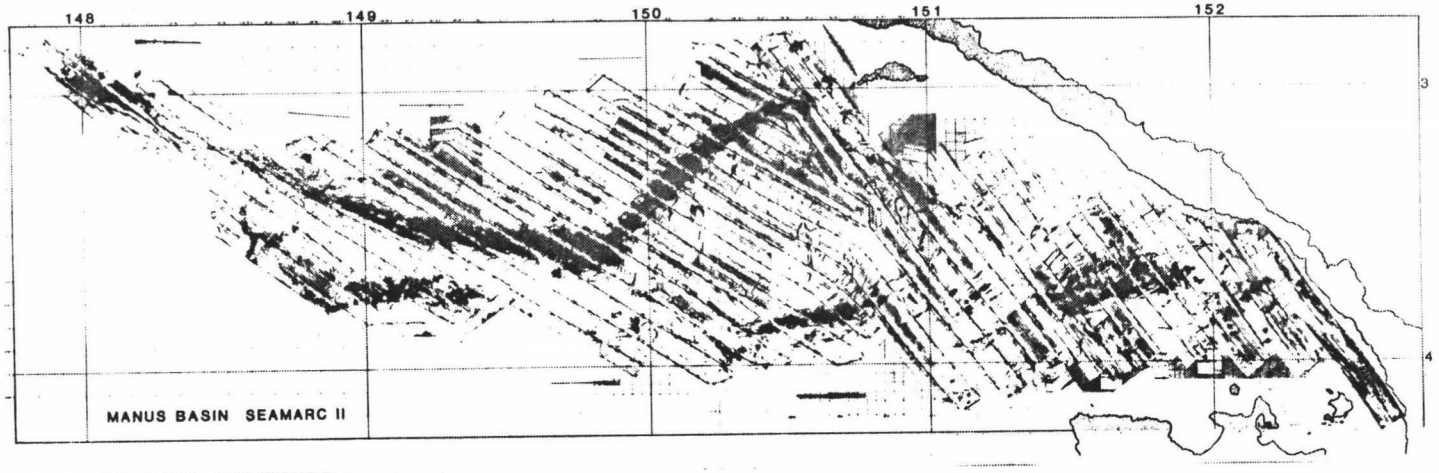
148
149
150
151
152
3
4
MANUS BASIN SEAMARC II

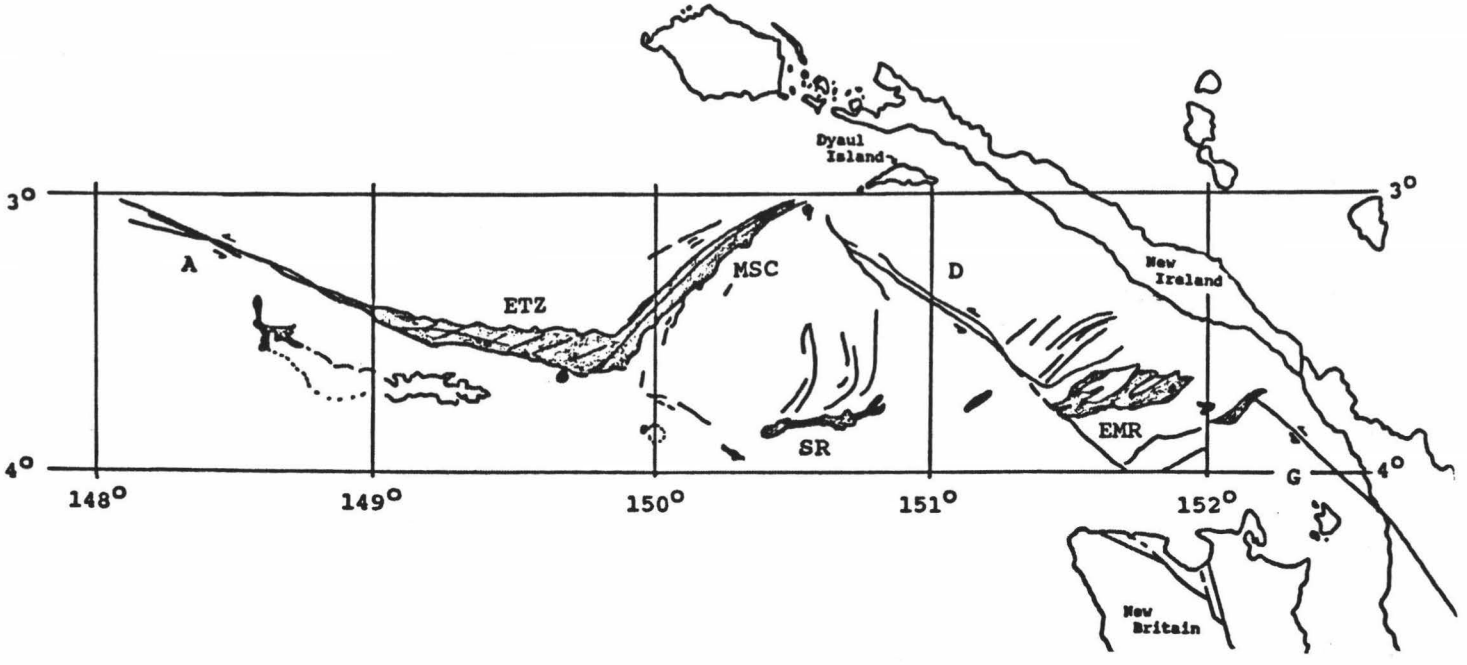
Dyaul Island
New Ireland
New Britain
A
ETZ
MSC
D
SR
EMR
G
3°
4°
148°
149°
150°
151°
152°

possibly propagating across, the Djaul Transform. Pseudofaults (paired-age discontinuities forming V-shaped boundaries between crusts of different ages) extend out on both sides of the northern tip of the rift, consistent with either rift propagation (Sinton et al., 1986), or a recent rift with large variations in spreading rate along strike. Sea-floor spreading began in the Manus Basin approximately 3.5 Ma (Taylor, 1979). A minimum spreading rate of about 120 mm yr^{-1} at the southwestern end has been estimated from magnetic lineation data (Connelly, 1976; Taylor, 1979; R. Mallonee and B. Taylor, pers. comm.). The rate decreases to the northeast. The MSC lies at a depth of about 2000 m toward the southwestern end ($3^{o}30$'S, $149^{o}55$'E), and becomes progressively deeper toward the northeast ($3^{o}05$'S, $150^{o}25$'E), reaching a maximum depth of about 2600 m. The magmatic budget is vigorous at the southwestern end, where both vesicular and nonvesicular lavas are present. At its northeastern end, the MSC grades into a deep axial valley. This may be a consequence of a diminishing magmatic budget. Lavas recovered from the northeastern end have extensively altered surfaces, indicating that the lavas are old and the eruption frequency low in this area. Alternatively, the alteration could be a result of the hydrothermal activity nearby, thus the lavas could be young. However, inactive hydrothermal vents were photographed near $3^{o}09.7$'S, $150^{o}16.8$'E, and the lavas sampled near the vents (within 100 m) did not have any sulphide staining (Both et al., 1986), suggestive of hydrothermal activity. Pumice recovered from the northeast tip of the axial valley of the MSC, possibly was erupted from the spreading axis itself or nearby New Britain.

The presence of a microplate in the Manus Basin is inferred by geophysical data (R. Mallonee and B. Taylor, unplublished data). The Manus microplate is bounded by the Manus Spreading Center on the northwest, the Southern Rifts on the south, the Djaul Transform Fault on the northeast, and a possible boundary (as yet

unnamed) on the southwest (Taylor et al., 1987). The southwestern boundary of the Manus Basin is marked by the eastern extension of the Willaumez Transform Fault.

Between the Manus Spreading Center and the Willaumez Transform Fault is a series of rift zones called the Extensional Transform Zone (ETZ). The ETZ is characterized by right-stepping, overlapping, *en echelon* rift zones (Fig.3). This *en echelon* repetition and associated prospective structures are important diagnostic features of wrench (strike-slip) zones. Wrenching causes two sets of intersecting, vertical fractures forming a predictable orientation along the wrench zone. These fractures can also form faults. The first set of fractures form at low-angles (10^{o}-30^{o}) to the wrench strike. The low-angle faults, called synthetic faults or Reidel shears, have the same sense of displacement as that of the main wrench zone and the final wrench fault. The second set of fractures intersect the wrench zone at high-angles (70^{o}-90^{o}). The high-angle faults, called antithetic faults or conjugate Reidel shears, have a sense of displacement opposite that of the wrench. The 90 km-long, 072^{o}-trending ETZ is cut by a Reidel Shear, trending 102^{o}, that is synthetic to the Willaumez Transform Fault, trending 117^{o} (Taylor et al., 1986). The geometry of the ETZ's structural elements with respect to the Willaumez Transform Fault is similar to that of a second order strain ellipse (Fig.4). No other transforms like the ETZ are presently known. The ETZ is about 2400 m deep on the northwest (3^{o}25'S, 149^{o}E) and southeast (3^{o}35'S, 149^{o}40'E) ends, and has a minimum depth of about 2000 m in the middle. Only vesicular lavas were recovered at this minimum depth or on this "high" zone of the ETZ (Fig.5a). The magmatic budget along the ETZ is vigorous and all of the lavas recovered are devoid of surface alteration implying they are of recent age.

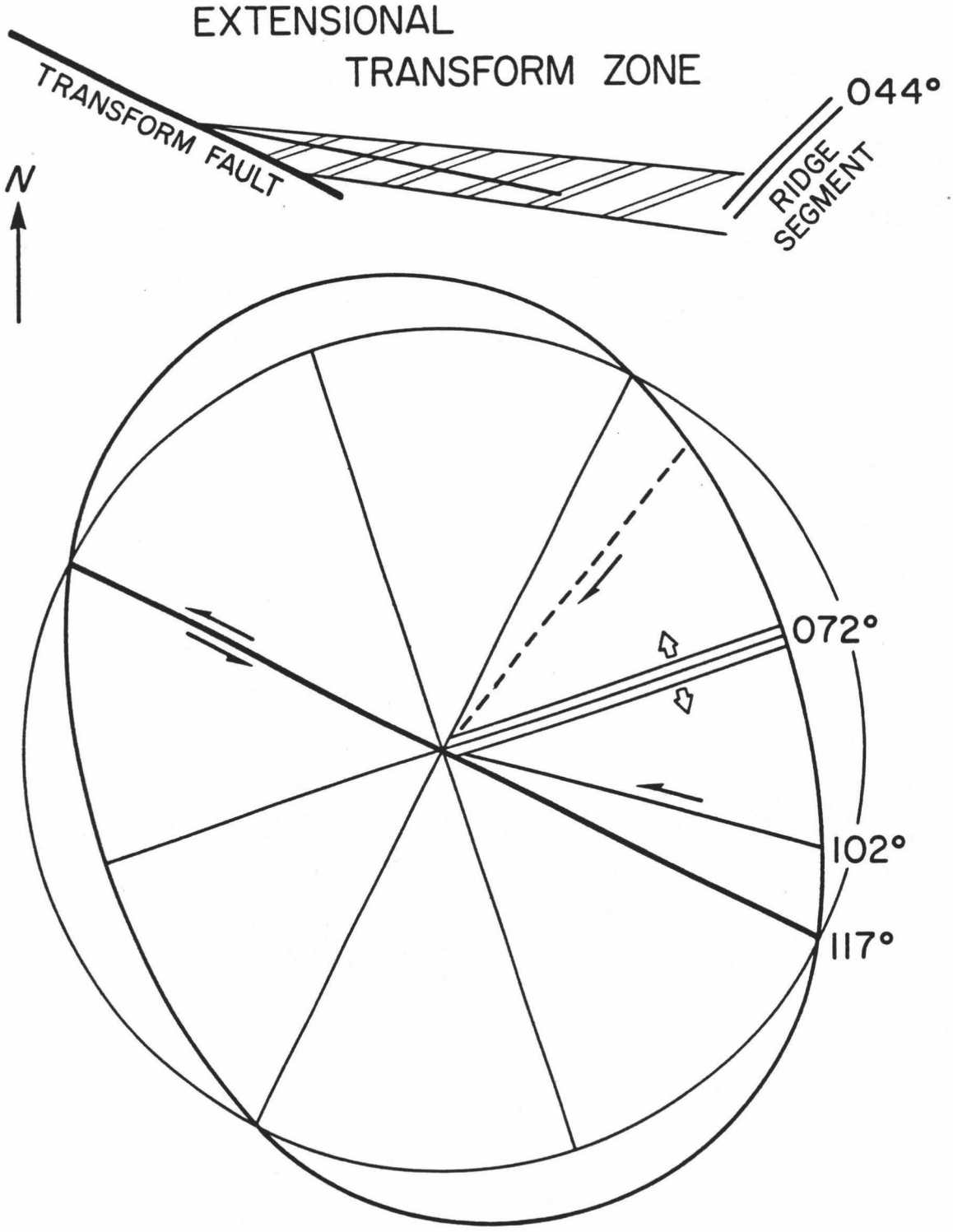

Figure 4. Second-order strain ellipse showing the geometry of the Extensional Transform Zones structural elements with respect to the Willaumez Transform Fault (After Taylor et al., 1986).

Figure 5. SeaMARC II bathymetry of the (a) Extensional Transform Zone (top) and profile through the Extensional Transform Zone (bottom), and (b) Manus Spreading Center (top) and profile through the Manus Spreading Center (bottom). Short, thick lines show dredge sample locations on the bathymetry. Sampled BABB (B), MORB (M) and X-BABB (XB) lithologies are shown above the depth profile: basalts (b), ferrobasalts (f) and basaltic andesites (ba).

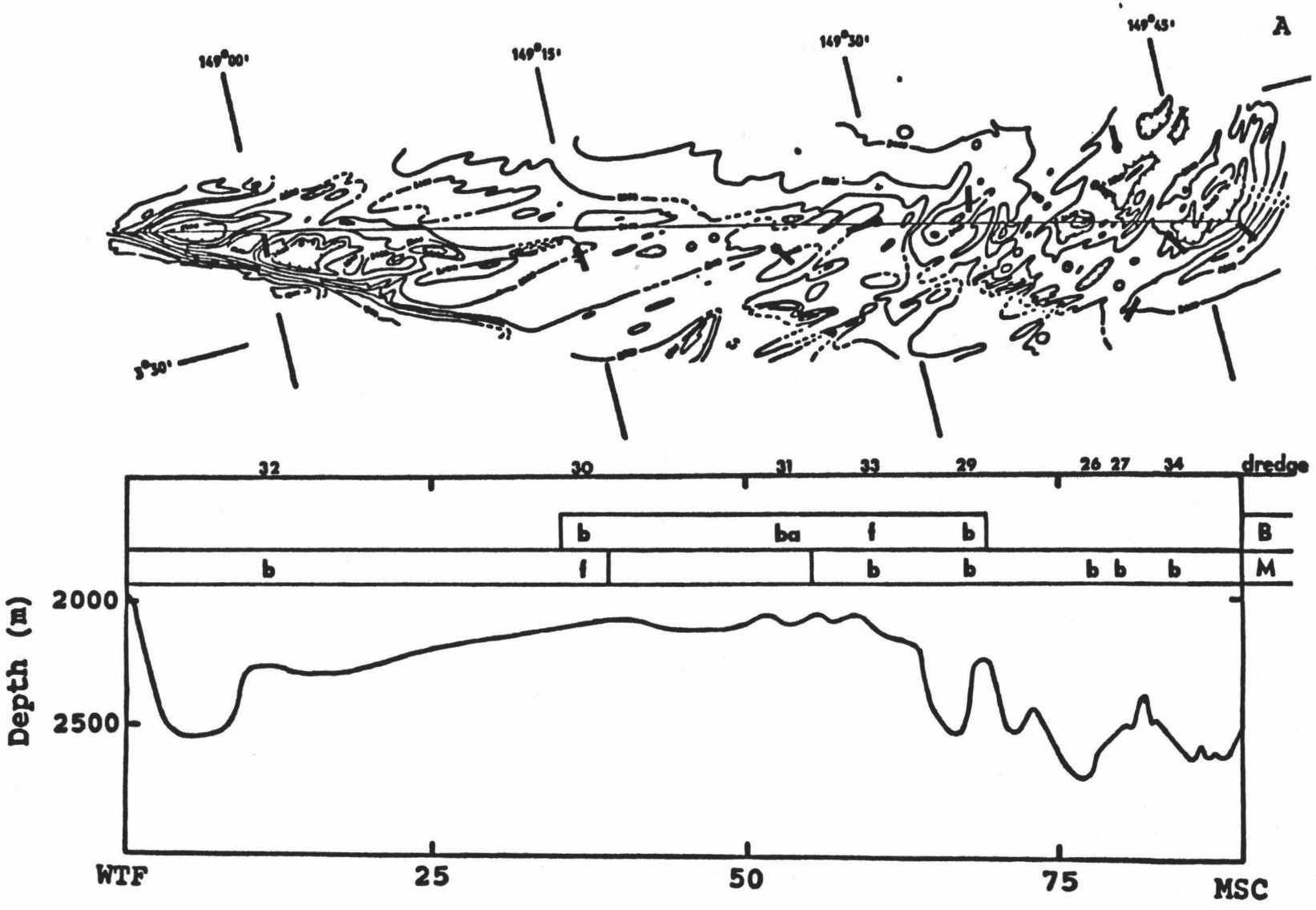
A
149°00'
149°15'
149°30'
149°45'
5°30'
32
30
31
33
29
26 27
34
dredge
b
ba
f
b
B
b
f
b
b
b b
b
M
2000
2500
Depth (m)
WTF
25
50
75
MSC
Distance (km)

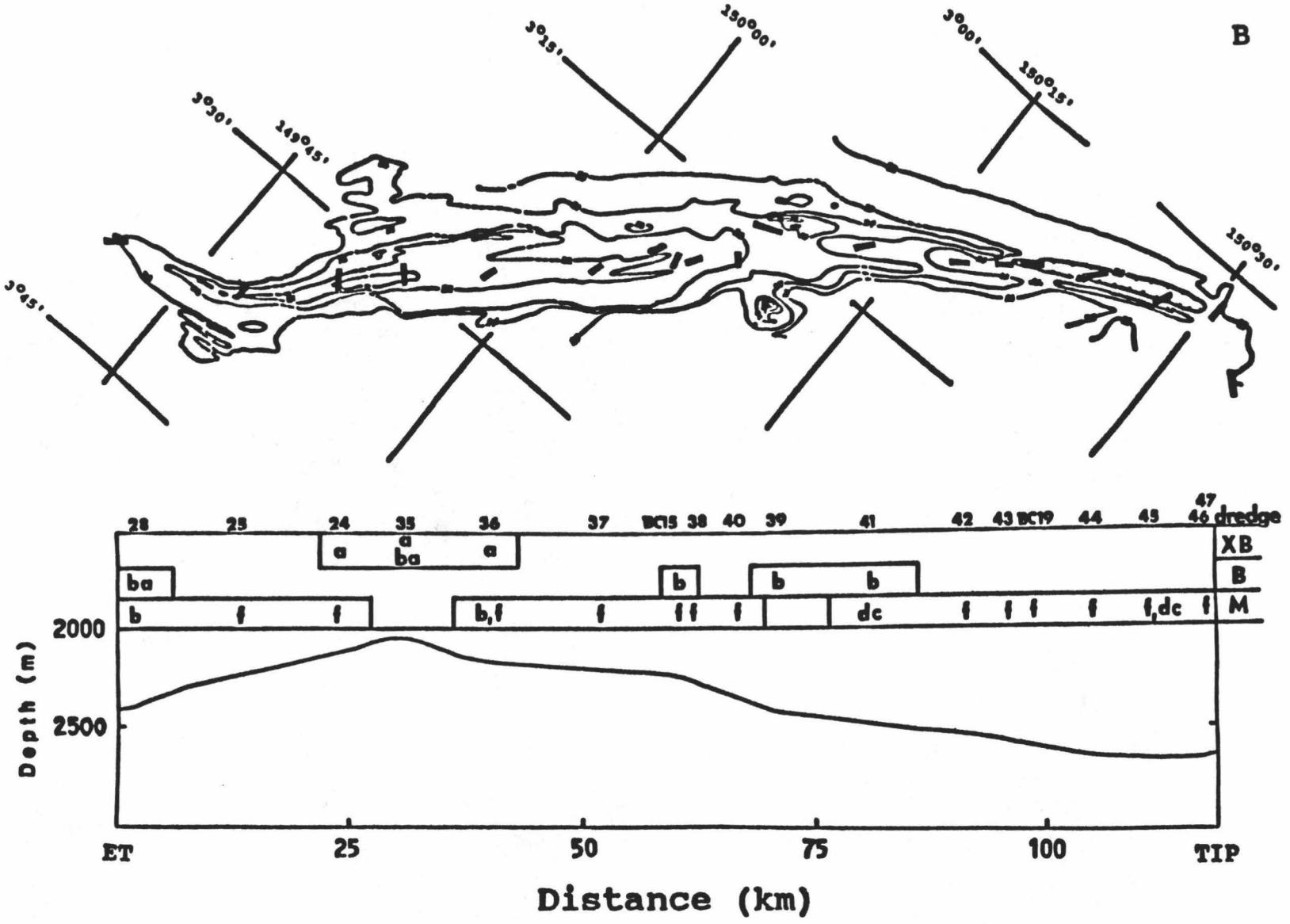
B
30°15'
150°00'
30°00'
150°15'
30°30'
149°45'
150°30'
30°45'
28 25 24 35 36 37 BC15 38 40 39 41 42 43 BC19 44 45 46 47 dredge
XB
B
M
a
ba
b
f
b,f
dc
f,dc
2000
2500
Depth (m)
ET
25
50
75
100
TIP
Distance (km)

TRANSFORM FAULT EFFECTS

Vogt and Johnson (1975) recognized that transform faults can serve as barriers to subaxial magma flow along mid-ocean ridges. Truncation of the ridge segment by a transform fault disrupts the thermal environment in the vicinity of the ridge-transform intersection, creating a "cold boundary" (Gallo and Fox, 1979). This cold boundary can lead to less melting, which, in turn, results in lavas that are more enriched in TiO_2, FeO^* and Al_2O_3 near the transform. The cooler thermal regime is also supported by observations of a relatively thin crust near the ridge-transform intersection (Gallo and Fox, 1979). Melting contours beneath a ridge-transform intersection show that there should be less extensive melting, and that melting should begin at shallower depths. Basalts from ridge-transform intersections tend to be more fractionated which is due to either ponding of the subaxial flow against the transform fault (Bender et al., 1984) or disruptions in magma chamber geometries so that differentiated lavas evolve in small disconnected chambers (Sinton et al., 1983).

The chemical systematics at the Tamayo Fracture Zone on the East Pacific Rise, and at other ridge-transform intersections show that some basalts near ridge-transform intersections have higher concentrations of TiO_2, FeO^*, incompatible elements (U, Th, Rb, K, Cs, Nb, LREE, P, Ta), and higher ratios of La/Sm and La/Yb, with respect to normal-MORB away from such intersections (Langmuir and Bender, 1984). These chemical characteristics have been collectively referred to as the transform fault effect (TFE) (Bender et al., 1984; Langmuir and Bender, 1984). The detection of the TFE may be obscured by magma mixing, high-pressure crystallization, and seamount volcanism. In addition, TFE's can be complicated if

extension occurs within the transform itself, or possibly by a shift in transform position which can lead to a shift in position of the ridge-transform intersection.

PREVIOUS STUDIES OF BACK-ARC BASINS

Magma genesis in the Manus Back-Arc Basin raises basic questions regarding the relationship of magma composition to the tectonic setting. What types of lavas are produced at transforms and spreading centers, and how do these lavas compare with other back-arc lavas and with mid-ocean ridge basalts (MORB)?

Evidence, based on the structure and magnetic lineations of back-arc basin crusts, implies that crustal generation is similar in some back-arc basins and major ocean basins (Watts et al., 1977; Taylor and Karner, 1983). However, magnetic lineation patterns can be difficult to correlate in some back-arc basins. Alternatively, spreading in some back-arc basins may be more diffuse than in the major ocean basins. The magnetic signal in back-arc basins may be unclear due to the small size of the spreading segment, or their formation near the geomagnetic equator. Therefore, the difficulties may be a function of the size of the spreading segment rather than fundamental differences in spreading processes (Taylor and Karner, 1983).

Although the petrology of Manus Basin lavas has not previously been reported, work has been done on lavas from other back-arc basins. Studies of back-arc basin lavas using whole-rock data found few differences between the major elemental composition of mid-ocean ridge basalts and basalts from back-arc basins (Hart et al., 1972; Hawkins, 1974; Hawkins and Batiza, 1975; Gill, 1976; Tarney et

al., 1977; Mattey et al., 1981). However, later studies of volcanic glasses showed striking differences between mid-ocean ridge and back-arc basin lavas. Glasses from the Mariana Trough and Scotia Sea, for example, have higher Al_2O_3 and lower total FeO (FeO^*). Enrichment in K, Rb, Sr, Ba and light rare earth elements (LREE) (Hart et al., 1972; Fryer et al., 1981; Hawkins and Melchior, 1985; Sinton et al., 1987; Sinton and Fryer, 1987), and H_2O, CO_2 and Cl have been documented in some back-arc basin rocks (Garcia et al., 1979; Muenow et al., 1980). Fryer et al. (1981) suggested that these "enriched" lavas represent a distinct magma type found within back-arc basins and called them "back-arc basin basalts" (BABB).

The total compositional range of lavas recovered from back-arc basins is quite variable. Rocks similar in composition to mid-ocean ridge basalts (MORB), back-arc basin basalts (BABB), island-arc, and even a type of BABB that is highly enriched in incompatible elements (Hart et al., 1972; Hawkins, 1976; Garcia et al., 1979; Fryer et al., 1981; Hawkins and Melchior, 1985; Sinton et al., 1987; Sinton and Fryer, 1987) have been recovered from back-arc basins. The source regions and processes that control the chemical composition of back-arc volcanism remain controversial.

Prior to this study only a few small pieces of volcanic glass had been recovered from the southern Bismarck Sea. Davies and Price (1987), on the basis of a single microprobe major element analysis of the glass, described the sample as a normal mid-ocean ridge basalt (N-MORB).

Few previous petrological studies of back-arc basin lavas have been framed in a plate-tectonics context. For example, do these lavas come from well-established spreading centers, "point-source" volcanic centers, off-axis seamounts, or transform boundaries? The present-day plate tectonic setting is known for the Manus Basin and all of the volcanically-active features have been sampled. This study represents

the first investigation of magmas related to transforms and spreading centers in a back-arc basin setting. The goals of this study were to examine the relationship of lava compositions to tectonic elements in the Basin, and the compositional variations between and within the Manus MORB and BABB lava suites. This study focuses on relationships between depth, source composition and melting processes in the Manus Extensional Transform Zone and Manus Spreading Center regions.

II. MATERIALS AND METHODS

Surveys and sampling of the Manus Basin were performed during two cruises (MW8517 and MW8518) aboard the University of Hawaii's R/V MOANA WAVE from December, 1985, to January, 1986. Surveys included SeaMARC II side-scan imaging and bathymetric swath mapping. The SeaMARC II survey imaged the tectonic features in the Manus Basin. This image was used to select sites for rock sampling.

Rock samples were taken from 34 dredges on the four main active features of the Manus Basin (Fig.5). The rock dredge consisted of a chain-link bag with a rigid metal rim around the top, and a 0.9 M.T. (1 ton) lead weight attached to the towing cable. Dredges 14-18 were located in the East Manus Ridges. Dredges 19-22 were located in the Southern Rifts and Dredge 23 was recovered from a seamount to the west of the Southern Rifts. Dredges 26, 27 and 29-34 were from the Extensional Transform Zone (ETZ), and Dredges 24, 25, 28 and 35-47 were from the Manus Spreading Center (MSC).

Four additional samples were collected. Three rock samples were recovered during two bottom camera stations (BC-15 and BC-19), and one volcanic glass sample was recovered from a gravity core (GC-10). The samples were sorted according to rock type based on their physical differences, including mineralogy, vesicularity, alteration/weathering and density. These samples were then thin-sectioned for petrographic and mineral analyses. The thin-section slabs were cut from the outer surface (usually glassy) into the core of the rock in order to evaluate the presence of cooling structures and mineral zoning relationships in the rock.

Preparation of rock samples for geochemical analysis included rock powdering. The rocks were scrubbed with a nylon brush and rinsed with tap water to loosen sediment debris, and then ultrasonically bathed in distilled water until the water remained clear. The rocks were then squirted with alcohol to speed drying and oven dried at a maximum temperature of 110°C for 1/2 to 1 hour. The rocks were broken into small pieces (approximately 10 mm cubes) with a hydraulic press. These smaller chunks of rock were used because it was easier to identify alteration surfaces on the rock which could cause chemical contamination of the rock powder. A tungsten-carbide shatter box was then used to crush the samples into a fine powder.

X-ray fluorescence spectrometry (XRF) was used to analyze major elements on representative samples of whole-rock powders. Whole-rock powders were combined with a fusion mixture to reduce matrix effects and lower the melting point of the rock powders. They were melted in a platinum crucible because of its high melting temperature and its chemically-inert nature. The melt was then rapidly quenched and pressed into glass discs in one step for major element analyses on the XRF spectrometer. Techniques for XRF analyses of rock samples are described by Norrish and Hutton (1969). A fully-automated Siemens X-ray fluorescence spectrometer in the laboratory of Dr. Bruce Chappell at the Australian National University in Canberra was used to analyze eighteen samples from the ETZ and forty-five samples from the MSC. Each sample was analyzed in duplicate and the resulting concentrations were averaged. Total iron, measured as Fe_2O_3 (ferric iron) was analyzed by XRF; FeO (ferrous iron) was measured by titration of excess ammonium metavanadate with an oxidizing agent, $K_2Cr_2O_7$.

Trace element concentrations were also measured by XRF, on whole-rock pressed powder pellets, using a fully-automated Philips X-ray fluorescence

spectrometer in the laboratory of Dr. Chappell at the Australian National University. Techniques for sample preparation and analysis are described in Norrish and Chappell (1977). Basically, the whole-rock powder is poured into a steel cylinder and is compressed with a steel plunger. Boric acid is then added to the cylinder and compressed again; this results in a compact rock powder pellet encased in boric acid.

Instrumental neutron activation analysis (INAA) for rare earth and for some trace elements on four samples from the ETZ and twenty-three samples from the MSC was also performed by Dr. Chappell. The techniques used are similar to those given by Goles (1977).

Fresh glass rinds from submarine lavas were used in the study to avoid the effects of crystal addition and alteration (Byerly et al., 1977). Major element analyses with an electron microprobe were performed on glass rinds in order to determine magmatic compositions of the glasses and define liquid fractionation paths.

To prepare samples for electron microprobe analysis, the glassy rind of each rock sample was removed. These glasses were then crushed with a boron-carbide mortar and pestle and passed through a 1-mm nylon mesh sieve. The glass chips were cleaned ultrasonically in distilled water to remove any sediment debris. Samples were then immersed in 0.3 N HCl to remove any carbonate film on the surface of the glass chips. Subsequent distilled water washes in the ultrasonic cleaner removed any adhering particles. Samples were oven dried at 120°C. Glasses were picked by hand under a binocular dissecting microscope. A 1-mm diameter chip was preferred because it was usually free of microphenocrysts and weathered/altered material. The cleaned glass chips were mounted in plastic discs with epoxy and polished to a 0.3-μm finish. The sample discs and comparison standards were then carbon-coated to maintain analysis consistency. A total of two hundred and five glass samples from the Manus Basin were analyzed (thirty-nine glass samples from

the ETZ, ninety-nine glass samples from the MSC, and sixty-seven glass samples from the East Manus Ridges and Southern Rifts) by electron microprobe at the University of Hawaii, using techniques similar to those described by Byerly et al. (1977). A Cameca-MBX wavelength-dispersive, three-spectrometer electron microprobe was used for the analyses. The glass standards used for analyses of SiO_2, TiO_2, Al_2O_3, FeO^*, MgO, CaO, Na_2O, K_2O and P_2O_5 were from the Juan de Fuca Ridge (VG-2) and Makaopuhi lava lake (VG-A99); the MnO standard was rhodonite. These elements were analyzed with counting times of 10 seconds. P_2O_5 was analyzed separately with counting times of 50 seconds using an apatite standard (USNM # 104021). All analyses of glass samples used a defocused beam (~25 μm), an accelerating voltage of 15 kV and sample current of 12 nA. A minimum of six measurements were performed on each sample and the resulting values were averaged and normalized to the glass standards.

Representative samples from each chemical group within the ETZ were analyzed for mineral composition on polished thin sections. Their compositions are used to determine equilibrium/disequilibrium assemblages and to model fractionation and/or mixing.

The presence and concentration of volatiles were determined by Knudsen cell, quadruple mass spectrometry on four samples from the ETZ and fourteen samples from the MSC by Dr. David Muenow and Mr. Kwesi Aggrey at the University of Hawaii (Aggrey, 1989). The concentration of volatiles provides additional geochemical constraints for a petrogenetic model for the origin of ETZ magmas.

III. RESULTS

MAGMA TYPES IN THE MANUS BASIN

Samples were initially classified according to vesicularity. Most lavas recovered in the East Manus Ridges were vesicular. Vesicular and nonvesicular lavas were recovered, in the approximate proportion of 1:1, from the Southern Rifts. The Southern Rift seamount recovered only nonvesicular lavas. Extensional Transform Zone (ETZ) and Manus Spreading Center (MSC) lavas ranged from essentially nonvesicular to moderately vesicular vesicular types. Three types of lavas could be identified: 1) vesicular, represented lavas erupted in the Manus Basin closest to the trench, 2) moderately vesicular, and 3) nonvesicular, represented lavas erupted farthest from the trench. These classifications were refined using major element data (Table 1). Compositional variations within and between each dredge is apparent, especially K_2O and FeO^* (total iron) (Fig.6) and illustrated for other major elements in Figure 7. The groups were further refined, based on trace element data. These groups then were used in order to assess larger variations, such as magma types within the Manus Basin. Out of the entire suite of lavas from the Manus Basin, three major types of magma are represented.

The MORB (mid-ocean ridge basalt) group (Fig.6) range from basalts to dacites with the essential characteristics of normal mid-ocean ridge basalts (N-MORB); however, compared to N-MORB (*e.g.* along the East Pacific Rise and the Mid-Atlantic Ridge) they have extremely low concentrations of TiO_2 ($\simeq$ 1.0 wt. % at 8 wt. % MgO), Al_2O_3, K_2O ($\simeq$ 0.04 wt. % at 8 wt. % MgO) and P_2O_5. These lavas are nonvesicular with only a slight increase in vesicularity observed through the

Table 1. Major Element Concentrations (Group Means) of Volcanic Glasses from the Manus Spreading Center and Extensional Transform Zone by Electron Microprobe

Group	n*	t**	Mg #	SiO2	TiO2	Al2O3	FeO*	MnO	MgO	CaO	Na2O	K2O	P2O5	Total
MSC														
24A	4	M	49	51.25	1.39	13.85	12.55	0.19	6.77	11.55	2.36	0.06	0.11	100.08
24B	6	XB	45	57.98	1.00	15.03	7.90	0.12	3.63	7.40	3.69	0.56	0.18	97.49
25A	1	M	59	50.08	1.03	14.87	9.91	0.15	7.94	12.60	2.12	0.03	0.15	98.88
25B	3	M	47	51.08	1.47	13.49	12.96	0.21	6.43	10.80	2.43	0.06	0.15	99.08
28A	2	B	52	51.00	1.12	14.72	11.06	0.17	6.80	11.73	2.20	0.12	0.18	99.10
28B	1	B	50	55.53	0.96	16.37	7.81	0.14	4.42	9.09	3.22	0.17	0.17	97.88
35A-1	2	XB	54	54.69	0.82	16.25	6.89	0.16	4.57	9.55	3.31	0.71	0.29	97.24
35A-2	2	XB	55	56.16	0.78	16.08	6.83	0.09	4.66	8.46	3.28	0.66	0.30	97.30
35A-3	2	XB	53	56.46	0.90	15.95	7.77	0.12	4.96	9.41	3.21	0.68	0.25	99.71
35B	2	XB	47	57.98	1.05	14.51	8.56	0.11	4.30	7.79	3.53	0.63	0.17	98.63
35C	1	XB	39	61.64	0.90	15.47	5.96	0.12	2.10	5.13	4.51	1.29	0.40	97.52
36A	2	M	60	51.04	1.00	14.89	10.10	0.17	8.45	12.60	2.15	0.05	0.16	100.61
36B	1	M	50	50.71	1.29	13.78	12.22	0.19	6.79	11.60	2.14	0.05	0.16	98.93
36C	4	M	41	51.66	2.03	13.35	14.14	0.18	5.52	9.98	2.86	0.10	0.22	100.04
36D	3	XB	55	56.09	0.88	16.08	7.45	0.13	5.05	8.79	3.34	0.64	0.24	98.69
37	9	M	53	50.80	1.21	14.11	11.65	0.17	7.37	11.36	2.26	0.05	0.17	99.15
38A	1	M	48	51.36	1.36	13.77	12.83	0.16	6.68	11.02	2.36	0.05	0.17	99.76
38B	3	M	47	51.49	1.50	12.82	13.64	0.23	6.66	11.26	2.46	0.04	0.17	100.27
38C-1	2	B	47	52.53	1.19	14.51	11.97	0.18	5.84	10.18	2.60	0.18	0.20	99.38
38C-2	2	B	43	52.58	1.40	13.24	13.23	0.20	5.52	9.89	2.74	0.19	0.18	99.17
39A	3	M	50	51.08	1.29	13.50	12.63	0.18	6.99	11.28	2.31	0.05	0.14	99.45
39B	1	M	45	51.18	1.57	12.73	13.90	0.24	6.50	11.30	2.46	0.08	0.17	100.13
40	6	B	49	52.09	1.10	15.03	10.99	0.16	5.92	10.72	2.60	0.18	0.16	98.95
41A	3	B	53	51.96	0.96	15.14	9.71	0.21	6.25	11.09	2.56	0.10	0.09	98.07
41B	2	M	10	67.60	0.79	11.74	9.38	0.19	0.57	4.45	4.32	0.32	0.18	99.54
42A	2	M	49	50.94	1.25	13.78	12.28	0.20	6.55	11.05	2.39	0.06	0.08	98.58
42B	1	M	44	51.93	1.40	13.93	13.09	0.24	5.78	10.16	2.79	0.06	0.14	99.52
43A	1	M	51	51.57	1.22	14.15	11.74	0.14	6.77	11.58	2.44	0.08	0.17	99.86
43B	2	M	36	52.15	1.72	13.03	14.84	0.24	4.70	9.16	3.04	0.10	0.18	99.16
44	5	M	50	51.32	1.22	14.00	12.42	0.21	6.89	11.29	2.33	0.05	0.17	99.90
45A	1	M	35	51.30	1.75	13.30	15.07	0.25	4.65	9.34	2.69	0.13	0.23	98.71
45B	1	M	46	51.55	1.46	13.56	13.26	0.18	6.38	11.09	2.38	0.04	0.16	100.06
45C	4	M	6	65.71	0.77	11.36	10.46	0.22	0.39	4.73	4.02	0.32	0.24	98.22
46	5	M	22	53.00	2.36	11.76	17.91	0.29	2.77	7.91	3.03	0.13	0.30	99.46
47	3	M	39	51.10	1.83	13.03	15.44	0.21	5.47	9.85	2.81	0.10	0.31	100.15
BC-15	2	M	46	51.43	1.40	13.74	12.99	0.22	6.33	10.84	2.38	0.05	0.13	99.51
BC-19	1	M	40	51.74	1.56	13.60	13.85	0.25	5.27	9.72	2.49	0.07	0.17	98.72
GC	1	B	52	51.66	1.11	14.96	11.10	0.16	6.70	11.79	2.25	0.11	0.09	99.93
HCRA	1	B	51	51.55	1.11	14.50	10.86	0.13	6.46	11.33	2.40	0.09	0.15	98.58
HCRB	1	M	46	52.25	1.28	14.02	12.37	0.18	5.93	10.35	2.55	0.09	0.13	99.15
ETZ														
26	6	M	55	51.08	1.04	14.22	10.90	0.20	7.38	12.21	2.10	0.05	0.16	99.34
27	3	M	54	50.54	1.16	14.05	11.27	0.20	7.30	12.00	2.11	0.04	0.16	98.83
29A	1	M	58	50.75	1.02	15.04	10.58	0.21	8.16	12.72	2.17	0.04	0.15	100.84
29B	4	B	61	51.96	0.77	15.95	7.82	0.13	6.87	12.04	2.27	0.13	0.13	98.07
30A	3	B	46	52.99	1.12	14.87	10.75	0.20	5.17	9.45	2.95	0.17	0.16	97.83
30B	2	B	38	52.69	1.40	13.95	12.87	0.19	4.45	8.77	3.05	0.16	0.15	97.68
30C	1	B	35	54.07	1.50	13.64	12.97	0.23	3.89	8.04	3.25	0.22	0.17	97.98
31A	2	M	50	50.00	1.64	13.95	11.85	0.23	6.67	11.45	2.67	0.12	0.19	98.77
31B	4	M	51	50.89	1.33	14.12	12.37	0.19	7.20	11.55	2.38	0.05	0.16	100.24
31C	1	B	68	50.30	0.40	15.74	7.07	0.09	8.25	13.68	1.48	0.08	0.13	97.22
32A	2	M	58	50.42	1.00	14.89	10.39	0.14	8.14	12.34	2.21	0.04	0.17	99.74
32B	3	M	56	50.26	1.07	14.51	10.73	0.18	7.72	12.56	2.25	0.05	0.16	99.49
33A	1	B	34	53.50	1.39	14.71	12.91	0.28	3.74	8.62	3.22	0.25	0.14	98.76
33B	3	M	53	51.37	1.09	14.19	11.44	0.18	7.35	12.62	2.30	0.02	0.15	100.71
33C	2	B	38	53.28	1.38	14.78	12.47	0.20	4.15	8.86	3.20	0.22	0.20	98.74
34	1	B	55	51.15	0.94	14.72	10.60	0.16	7.19	12.34	2.14	0.07	0.13	99.44

Analyzed by L. Liu, HIG.
*number of samples averaged.
**magma types: M = MORB, B = BABB, and XB = X-BABB

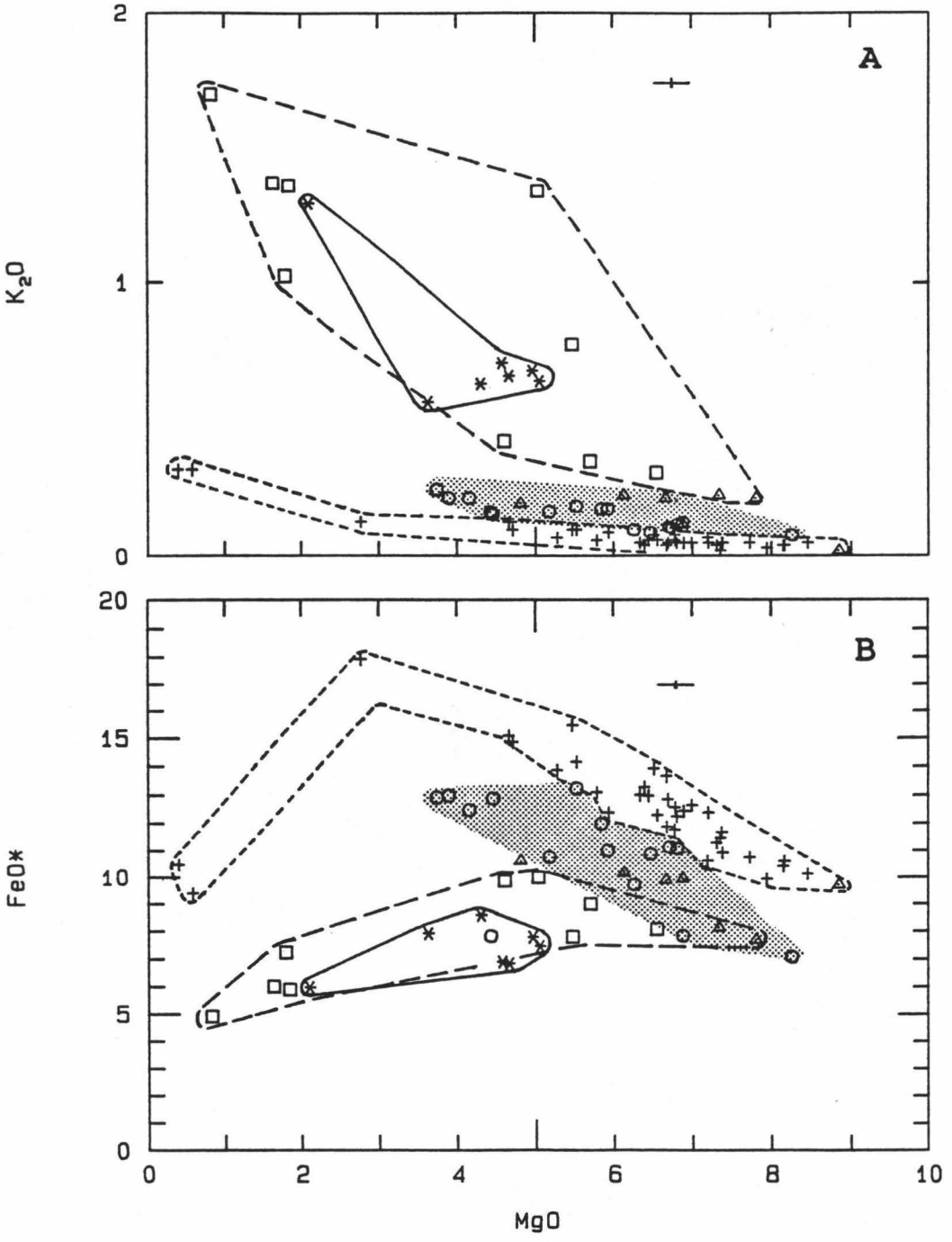

Figure 6. (a) K_2O versus MgO and (b) FeO^* versus MgO for all glass data group means from the Manus Basin. MORB field is shown by the short dashed line, BABB field by the stippled region, island arc associated lava field by the long dashed line and X-BABB field by the solid line. Symbols are as follows: MSC and ETZ MORBs (+), MSC and ETZ BABBs (o), MSC X-BABB (*), SR (Δ) and ER (□). Relative uncertainty of the probe analyses is shown by the cross in each figure.

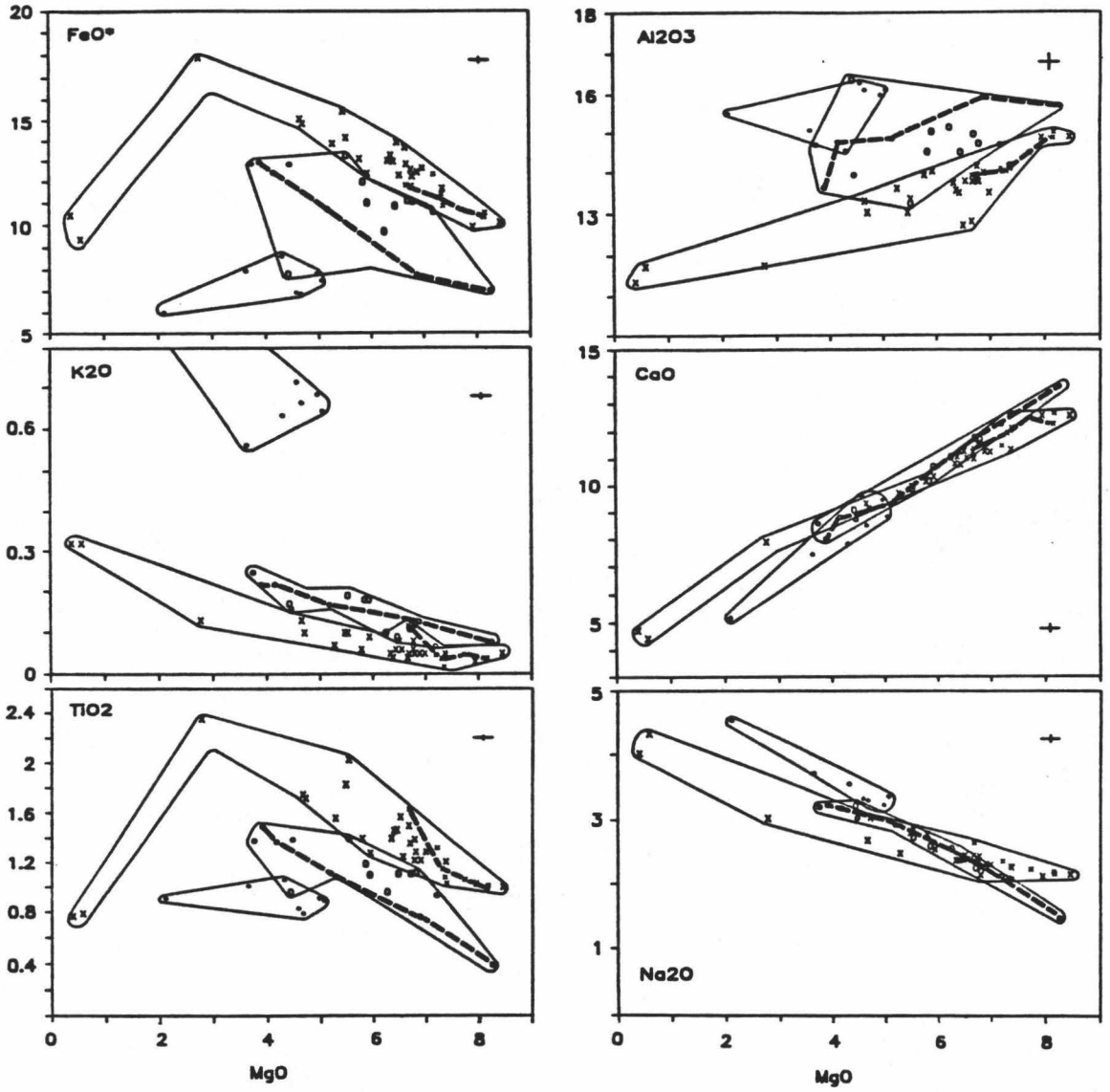

Figure 7. Major element variations versus MgO for Extensional Transform Zone and Manus Spreading Center glass data listed in Table 1. The whole suite of Manus Basin MORBs, BABBs and X-BABBs are shown by the enclosed fields. Heavy dashed lines show calculated fractionation paths. Symbols are: (x) MORB, (o) BABB and (*) X-BABB. Relative uncertainty of the probe analyses is shown by the cross in each figure.

differentiation sequence. The MORB group also defines a strong iron-enrichment trend. The MORB group is restricted to the Manus Spreading Center and Extensional Transform Zone.

Compared to the Manus MORB group at the same MgO, the BABB (back-arc basin basalt) group ranges from basalts and basaltic andesites (Fig.6). They contain greater Al_2O_3 and K_2O ($\simeq$ 0.08 wt. %), and lower FeO^* ($\simeq$ 7 wt. %) and TiO_2 ($\simeq$ 0.4 wt. %) contents. This major element variation is similar to variations of other back-arc basin basalts (*e.g.* Mariana Trough: Fryer et al., 1981). These lavas occur in the Extensional Transform Zone (ETZ), Manus Spreading Center (MSC) and Southern Rifts, but they were not recovered from the East Manus Ridges.

Lavas with a high K_2O concentration (Fig.6) are restricted to the rifts closest to the active arc (*i.e.* the East Manus Ridges and Southern Rifts). Like the MORB group, these lavas range from basalts to dacites, but they are very vesicular and lack a strong iron-enrichment trend. These lavas, with a high concentration of K_2O, will not be discussed further in this study. However, within the field for the high K_2O group, there are lavas of the BABB group recovered from the MSC (Fig.6). These BABB lavas, an extremely enriched type of BABB, are chemically and petrographically different from the high K_2O (arc-associated) lavas. The extremely enriched type of BABB or what I will call X-BABB is discussed in a later section.

The concentration of major elements also were determined on selected whole-rock samples (Table 2). These samples correspond to each representative mean glass group and reconfirm natural glass compositions. Large chemical variations between the glass and its corresponding whole-rock sample can be accounted for by phenocryst contribution. Phenocryst contribution of olivine and plagioclase would respectively cause higher MgO and Al_2O_3, and lower TiO_2; this effect is observed (Fig.8). Smaller variations are probably due to analytical uncertainty.

Table 2. Major and Trace Element Concentrations of Whole Rock from the Extensional Transform Zone and Manus Spreading Center by X-Ray Fluorescence Spectrometry

Group	ETZ 26	26	27	29A	29B	30A	30B	31A	31B	31C	32A	32B	33A	33B
Sample	26-5	26-14	27-5	29-3	29-4	30-2	30-3	31-1	31-3	31-8	32-5	32-3	33-1	33-3
SiO2	50.64	50.74	50.17	49.58	51.21	53.01	58.64	50.24	50.40	51.44	49.63	49.81	52.44	50.69
TiO2	1.03	1.06	1.07	0.96	0.70	1.05	1.14	1.46	1.19	0.35	0.98	0.99	1.27	0.97
Al2O3	14.32	14.45	14.64	14.92	15.89	15.41	12.61	14.30	13.80	15.23	14.84	15.46	14.68	14.38
Fe2O3	1.88	1.93	1.62	1.62	1.41	2.27	2.37	2.46	2.15	1.51	1.54	1.60	3.71	1.48
FeO	8.84	8.83	9.37	8.63	6.48	8.12	8.46	8.94	10.29	5.57	8.56	8.23	8.69	9.16
MnO	0.18	0.19	0.18	0.17	0.14	0.17	0.17	0.19	0.20	0.13	0.17	0.16	0.20	0.19
MgO	7.46	7.36	7.71	8.38	8.86	5.48	4.26	6.94	7.00	9.30	8.14	7.97	4.62	7.60
CaO	11.94	11.98	12.11	12.58	12.06	9.90	7.92	11.85	11.61	13.57	12.36	12.98	9.14	12.41
Na2O	2.41	2.41	2.24	2.23	2.30	2.91	2.68	2.65	2.49	1.44	2.33	2.23	3.21	2.27
K2O	0.09	0.13	0.05	0.04	0.14	0.27	0.17	0.22	0.05	0.08	0.05	0.07	0.29	0.04
P2O5	0.08	0.08	0.08	0.08	0.08	0.12	0.12	0.14	0.09	0.04	0.07	0.07	0.20	0.07
S	0.12	0.10	0.14	0.12	0.03	0.06	0.06	0.13	0.15	0.02	0.12	0.11	0.04	0.11
H2O+	0.54	0.45	0.26	0.38	0.65	0.80	0.90	0.41	0.32		0.41	0.27	0.70	0.27
H2O-	0.22	0.22	0.07	0.12	0.20	0.36	0.22	0.24	0.20		0.14	0.10	0.25	0.07
CO2	0.25	0.27	0.16	0.27	0.25	0.33	0.29	0.25	0.40		0.31	0.23	0.33	0.19
Total	100.00	100.20	99.87	100.08	100.40	100.26	100.01	100.42	100.34	98.68	99.65	100.28	99.77	99.90
Mg #	56	55	56	60	67	49	42	53	51	71	59	59	41	56
Sc		50			39		32				42			46
V	315	324	310	269	214	310	360	330	345	223	276	271	418	309
Cr	59	52	204	272	281	8	3	105	42	370	197	326	4	119
Co				55									43	
Ni	66	66	93	118	158	19	11	56	51	135	102	98	12	80
Cu	117	110	114	115	80	65	48	91	130	74	120	105	57	148
Zn	84	84	73	83	64	90	98	75	100	54	82	78	89	84
Ga	15.0	15.5	14.5	14.5	13.5	17.0	13.5	16.5	16.0	8.5	12.5	12.5	18.0	13.0
Rb	1.0	1.5	0.5	0.5	1.5	3.0	2.0	2.5	0.5	1.0	0.5	0.5	3.5	1.0
Sr	80	81	71	72	171	175	137	109	68	87	75	81	245	73
Y	22	23	24	21	13	23	27	30	27	10	23	23	27	24
Zr	53	52	57	50	42	61	68	89	57	17	54	54	79	50
Nb	0.5	0.5	1.5	0.5	0.5	0.5	1.5	2.5	1.0	0.5	0.5	0.5	1.0	0.5
Ba	10	6	6	4	26	36	50	22	8	12	10	10	72	12

Analyzed by B. Chappell, ANU.
T.E. in parts per million.

Table 2. (continued)

33B		33C	34	MSC 24A	24B	25A	25B	28A	35A-1		35A-2	35A-3		35B
33-5	33-9	33-2	34-1	24-1	24-9	25-2	25-1	28-1	35-3	35-5	35-2	35-1	35-4	35-7
49.63	52.28	52.30	50.02	50.29	57.72	50.18	50.50	50.38	56.59	55.71	55.60	55.79	54.41	56.72
0.97	1.24	1.27	0.88	1.38	0.98	0.95	1.43	1.05	0.78	0.81	0.77	0.77	0.88	0.91
14.44	14.58	14.64	14.73	13.61	15.28	14.98	13.44	14.35	16.20	16.35	15.92	15.83	15.89	15.67
1.68	3.24	4.61	1.74	1.91	1.67	1.78	2.27	2.18	1.98	2.59	2.07	2.55	2.51	1.78
8.85	8.73	7.88	8.57	10.68	6.19	8.34	10.87	8.66	4.93	4.55	4.76	4.57	5.78	5.81
0.18	0.19	0.20	0.18	0.20	0.13	0.17	0.21	0.18	0.12	0.12	0.11	0.12	0.14	0.12
7.90	5.13	4.38	7.75	6.73	3.59	8.23	6.46	7.48	4.59	4.55	4.55	4.68	5.31	4.09
12.54	9.01	9.03	12.11	11.45	7.33	12.58	10.90	11.56	8.47	8.59	8.32	8.60	9.47	7.94
2.32	2.98	3.24	2.27	2.46	3.89	2.30	2.52	2.25	3.66	3.57	3.74	3.70	3.39	3.72
0.07	0.46	0.39	0.08	0.06	0.64	0.08	0.06	0.15	0.70	0.73	0.70	0.73	0.58	0.66
0.07	0.22	0.21	0.07	0.12	0.20	0.08	0.12	0.11	0.33	0.33	0.32	0.32	0.27	0.20
0.12	0.04	0.06	0.12	0.15	0.03	0.10	0.16	0.13	0.06	0.04	0.06	0.05	0.04	0.02
0.42		0.85	0.63	0.47	1.76	0.29	0.56	0.56		1.31			1.07	1.43
0.16		0.46	0.19	0.12	0.38	0.16	0.19	0.35		0.47			0.37	0.65
0.28		0.47	0.24	0.29	0.71	0.24	0.31	0.33		0.52			0.47	0.40
99.63	98.10	99.99	99.58	99.92	100.50	100.46	100.00	99.72	98.41	100.24	96.92	97.71	100.58	100.12
58	44	39	58	49	45	60	47	56	55	54	55	55	54	50
			43	47	26	43		44			43	26		26
309	410	400	290	381	253	272	398	327	249	238	272	238	271	250
114	49	3	172	126	21	257	90	233	49	48	257	57	63	33
					31		53						36	
77	17	11	89	64	26	107	57	99	37	36	107	36	47	33
148	59	56	115	117	92	106	119	113	85	82	106	88	94	73
83	110	87	71	94	60	67	113	90	64	64	67	62	59	54
12.5	15.0	17.0	14.5	17.0	15.5	14.5	17.0	15.5	14.0	16.0	14.5	13.5	16.5	15.5
0.5	10.5	4.5	1.0	1.0	7.5	1.0	0.5	1.5	10.0	9.5	1.0	9.5	7.5	8.0
81	255	250	103	79	251	78	77	101	650	640	78	640	481	323
24	30	28	19	31	19	21	30	24	16	14	21	16	18	19
50	88	80	42	73	100	54	76	57	127	128	54	121	106	91
0.5	1.5	1.5	1.0	1.0	3.5	1.0	1.0	0.5	5.0	5.0	1.0	5.0	4.0	3.5
14	300	74	18	12	155	8	10	20	250	235	8	235	175	175

Table 2. (continued)

35C	36A	36B	36C	36D		37		38A	38B	38C-1	38C-2	39A	39B	40	
35-3C	36-2	36-1	36-8	36-4	36-6	37-1	37-2	38-3	38-4	38-8	38-9	39-1	39-2	40-1	40-6
53.13	49.92	51.62	51.11	54.71	56.12	50.73	50.35	50.68	50.91	51.31	52.86	50.46	51.09	51.51	51.76
0.63	0.95	1.23	1.98	0.81	0.82	1.22	1.24	1.37	1.38	1.17	1.22	1.23	1.39	1.07	1.08
17.33	14.72	13.56	13.18	16.26	16.08	13.94	13.98	13.38	13.41	14.28	14.01	13.70	13.45	14.72	14.85
3.90	1.62	1.62	2.44	1.80	1.84	1.55	2.17	1.89	2.39	2.66	2.55	2.00	2.22	2.57	2.95
3.50	8.35	10.23	12.02	5.48	5.36	10.29	9.87	11.05	10.68	9.29	9.43	10.18	10.84	8.34	7.81
0.11	0.17	0.20	0.22	0.12	0.12	0.20	0.20	0.21	0.21	0.19	0.19	0.20	0.21	0.18	0.18
6.18	8.36	6.86	5.05	4.75	4.85	7.33	7.53	6.42	6.51	5.83	5.57	6.99	6.51	6.09	5.95
10.57	12.51	11.25	9.82	8.73	8.80	11.66	11.56	10.91	10.98	10.26	9.94	11.46	10.98	10.79	11.05
2.84	2.18	2.36	2.83	3.35	3.49	2.36	2.42	2.53	2.53	2.73	2.77	2.42	2.51	2.63	2.61
0.50	0.05	0.06	0.10	0.65	0.67	0.05	0.05	0.06	0.06	0.22	0.26	0.05	0.06	0.23	0.26
0.22	0.07	0.09	0.20	0.24	0.24	0.10	0.10	0.10	0.11	0.12	0.12	0.09	0.11	0.11	0.12
0.02	0.11	0.13	0.19	0.03	0.03	0.14	0.16	0.16	0.16	0.17	0.09	0.14	0.16	0.09	0.05
	0.51		0.79	1.67		0.42	0.22	0.42	0.44	0.99		0.47	0.22	1.07	0.85
	0.22		0.07	0.41		0.07	0.16	0.08	0.19	0.41		0.16	0.12	0.33	0.42
	0.25		0.32	0.40		0.19	0.43	0.30	0.33	0.49		0.30	0.23	0.44	0.30
98.93	100.01	99.21	100.32	99.41	98.42	100.25	100.44	99.56	100.29	100.12	99.01	99.85	100.10	100.17	100.24
61	60	51	39	54	55	53	53	47	47	47	46	51	47	50	50
	43			31	26	46	46	47	48			47		40	
241	292	388	436	240	250	355	347	392	397	368	398	369	391	341	343
54	287	78	59	52	57	149	124	84	86	11	6	81	84	65	63
										47			55		
56	115	60	40	43	48	75	79	51	54	38	35	58	55	55	52
56	121	132	88	72	81	118	116	117	118	112	102	128	120	117	118
51	80	103	114	64	64	83	95	91	97	101	103	102	94	91	93
14.5	15.0	14.0	17.5	15.5	14.0	15.5	16.5	16.5	16.5	16.5	15.0	16.5	16.5	16.5	16.0
7.0	0.5	0.5	1.5	8.5	9.0	1.0	0.5	0.5	0.5	2.0	3.0	0.5	0.5	2.5	2.5
815	73	75	76	441	462	71	74	71	72	130	134	71	71	161	165
9	21	30	47	15	16	27	26	31	31	28	30	28	31	24	24
85	48	67	125	94	95	64	66	74	74	64	67	64	75	57	61
3.5	1.0	0.5	2.0	5.0	4.0	0.0	0.5	0.5	1.5	0.5	0.0	0.0	0.0	1.0	0.5
200	12	20	26	175	190	8	12	6	10	28	40	10	8	30	36

Table 2. (continued)

41A		41B		42A	42B	43B	44	45A	45B	45C			46	47		BC15	BC19
41-3	41-4	41-1	41-7	42-3	42-1	43-1	44-1	45-2	45-1	45-3	45-4	45-6	46-2	47-1	47-2	BC15-1	BC19-1
52.19	51.48	66.75	65.94	52.06	51.38	52.28	54.49	50.85	50.60	61.36	63.38	64.18	51.57	50.67	50.46	53.58	51.20
0.93	0.91	0.79	0.81	1.24	1.27	1.65	1.08	1.81	1.18	1.07	1.05	0.89	2.41	1.72	1.42	1.29	1.44
15.17	15.02	11.25	11.34	13.66	13.91	12.91	12.82	12.83	13.71	10.58	10.91	10.39	11.28	13.01	13.27	14.71	13.04
2.50	2.19	1.31	0.86	2.32	2.73	2.85	1.67	3.36	1.84		1.13	0.71	3.18	2.94	2.15	2.95	2.45
7.09	7.30	8.02	8.55	9.56	9.56	11.54	9.27	11.75	10.03	11.64	10.20	9.77	14.65	11.79	10.90	9.05	11.11
0.16	0.16	0.17	0.18	0.19	0.20	0.23	0.18	0.23	0.20	0.21	0.22	0.20	0.27	0.37	0.21	0.20	0.22
6.51	6.73	0.61	0.62	6.65	6.27	4.90	6.73	4.75	7.16	1.59	0.58	0.51	2.85	5.43	6.44	4.21	5.47
11.36	11.27	4.45	4.59	11.20	10.87	9.36	10.69	9.38	11.63	5.93	5.04	4.49	8.02	10.20	10.81	8.47	9.82
2.69	2.63	4.27	4.26	2.44	2.61	3.00	2.14	2.79	2.28	3.48	4.00	3.88	3.11	2.72	2.41	3.39	2.59
0.18	0.17	0.31	0.29	0.07	0.10	0.14	0.04	0.20	0.05	0.24	0.46	0.31	0.27	0.10	0.06	0.31	0.10
0.09	0.09	0.20	0.19	0.10	0.11	0.15	0.08	0.19	0.09	0.29	0.32	0.26	0.31	0.17	0.11	0.15	0.13
0.07	0.06	0.06	0.05	0.14	0.15	0.16	0.12	0.17	0.13	0.10	0.11	0.06	0.21	0.19	0.15	0.04	0.15
0.76	0.89	1.50	1.29		0.66	0.78		0.83			1.90		0.86	0.79			
0.40	0.40	0.04	0.06		0.28	0.30		0.51			0.38		0.43	0.10			
0.43	0.43	0.32	0.28		0.34	0.43		0.38			0.40		0.53	0.26			
100.53	99.97	100.05	99.31	99.63	100.44	100.68	99.31	100.03	98.90	96.49	100.08	95.65	99.95	100.46	98.39	98.35	97.72
55	56	11	11	50	48	38	53	36	52	20	8	8	22	40	47	39	42
40	43	15		46	45	45	43	42	46				42	45			
304	305	26	27	389	382	440	345	442	363	64	9	6	280	434	422	361	426
127	118	6	5	63	47	16	88	16	97	16	3	1	5	76	95	2	25
											12						
79	79	1	0	58	52	30	65	30	67	9	0	0	5	54	59	9	42
120	111	14	14	130	123	100	130	78	123	55	13	15	44	103	118	37	115
61	79	152	146	100	85	108	90	140	98	182	172	199	158	114	110	105	123
14.5	15.5	22.5	21.5	14.0	16.0	18.5	12.5	18.5	13.5	18.5	22.5	20.0	22.0	17.0	15.0	15.5	15.0
1.5	1.5	4.0	4.0	1.0	1.0	1.5	0.5	2.0	0.5	3.0	5.0	4.5	2.5	1.5	0.5	3.0	1.0
157	163	88	92	89	98	83	72	90	72	89	92	90	83	87	77	175	82
20	19	115	108	29	28	42	26	41	29	95	110	118	67	40	33	30	38
49	52	380	356	67	66	106	56	108	63	302	370	401	163	100	76	79	89
0.5	1.0	3.0	4.0	0.0	0.5	1.5	0.0	0.5	0.5	3.0	3.5	405.0	1.0	1.5	0.0	1.5	1.0
18	20	54	48	18	14	26	18	22	18	56	54	56	24	22	10	38	8

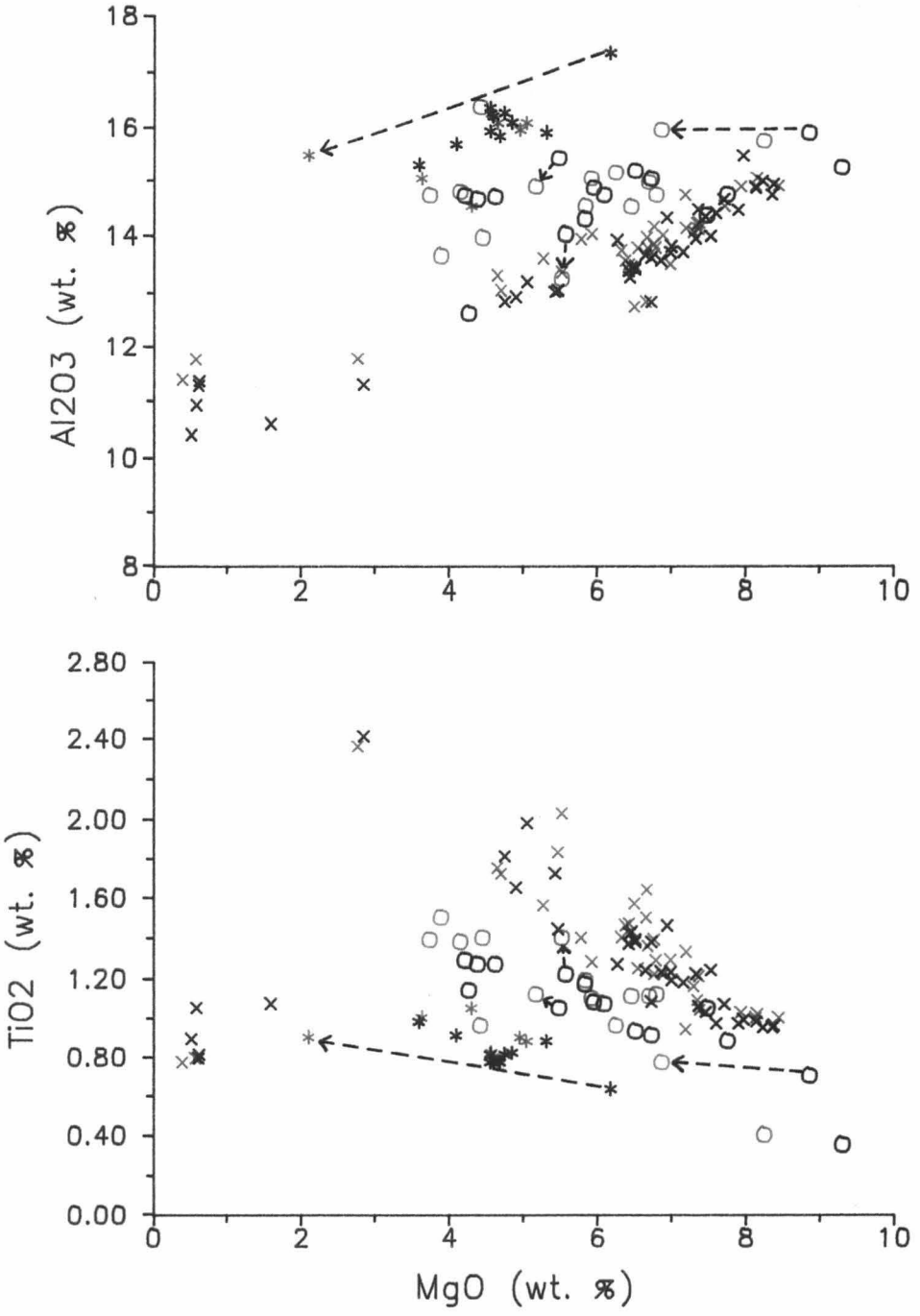

Figure 8. Chemical variations between averaged whole-rock data and averaged glass data from the Extensional Transform Zone and the Manus Spreading Center. (a) Al_2O_3 versus MgO and (b) TiO_2 versus MgO. In general, Al_2O_3 decreases and TiO_2 increases from whole-rock to glass due to the contribution of olivine and plagioclase in the whole-rock sample (shown for selected samples). Symbols are: (x) MORB, (o) BABB and (*) X-BABB for whole-rock and glass data. Blue symbols represent glasses and black symbols represent whole-rocks.

Trace element abundances (Table 2) substantiate the major magma type distinctions represented in the Manus Basin; other trace elements (Sc, Cs, Hf, Th and U) are presented in Table 3. Relative to Manus MORB lavas, the BABB lavas are enriched in Rb, Sr and Ba, and depleted in Zr, Sc, Cu, V and Y (Fig.9). These trends agree with data for other back-arc basin lavas compared to those from mid-ocean ridges. X-BABB lavas have greater and lower concentrations of the same elements as in the BABB lavas. However, Zr concentration is greater in X-BABB lavas compared to MORB, this is in contrast to BABB lavas which are depleted in Zr compared to MORB (Fig.9). Thus, for the element Zr the X-BABB lavas do not represent an extreme version of BABB lavas. Rare earth elements (La, Ce, Sm, Eu, Gd, Ho, Yb and Lu) are presented in Table 3 and plotted with Ba relative to chondrite in Figure 10. Twenty-two whole-rock samples from the ETZ and MSC form three progressive trends on the chondrite-normalized rare-earth element plot. The BABB lavas are enriched in the light rare earth elements (LREE) and Ba compared to MORB at fairly high levels of REE (10-15 times chondrite); this is similar to Mariana Trough lavas (Fryer et al., 1981; Sinton and Fryer, 1987). X-BABB, an extremely enriched version of BABB, form the third trend in the Ba-rare earth element plot (Fig.10). These lavas show a higher degree of enrichment of the light rare earth elements and Ba compared to BABB, but their moderate Ba/La and distinctly LREE patterns distinguish them from lavas of the island arc association.

The magma types can also be distinguished by water contents and total volatile abundances (Table 4). The Manus BABB lavas have water contents > 1 wt. % compared to the Manus MORB lavas, which have < 0.4 wt. % H_2O at about 8 wt. % MgO. Water content tends to increase through the differentiation sequence for both Manus MORB and BABB.

Table 3. Rare Earth and Other Element Abundances of Whole Rocks from the Extensional Transform Zone and Manus Spreading Center by Instrumental Neutron Activation Analysis

	ETZ				MSC								
Group	30B	32A	33B	34	24A	25A	28A	35A-3	35B	36A	36D	37	38A
Sample	30-3	32-5	33-3	34-1	24-1	25-2	28-1	35-1	35-7	36-2	36-6	37-1	38-3
La	4.0	1.40	1.30	1.65	2.2	1.50	1.95	21.5	12.1	1.65	15.7	1.85	2.1
Ce	9.8	4.2	4.6	5.0	7	4.8	5.7	43.5	23.0	5.0	31.0	5.7	6.5
Sm	2.70	2.15	2.15	2.00	3.10	2.20	2.40	3.40	2.60	2.10	2.70	2.70	3.00
Eu	0.96	0.82	0.82	0.79	1.09	0.81	0.92	0.94	0.83	0.80	0.86	0.97	1.10
Gd	3.4	3.0	2.9	2.7	3.9	3.0	3.4	2.7	2.6	2.9	2.5	3.6	4.2
Ho	1.05	0.80	1.00	0.75	1.20	0.90	0.90	0.60	0.75	0.80	0.65	1.05	1.10
Yb	3.05	2.60	2.65	2.45	3.60	2.65	2.95	1.80	2.30	2.50	1.80	3.30	3.75
Lu	0.44	0.40	0.44	0.39	0.59	0.41	0.48	0.28	0.34	0.40	0.28	0.52	0.59
Sc	32	42	46	43	47	43	44	26	26	43	26	46	47
Cs	<0.1	<0.1	<0.1	<0.1	<0.1	<0.1	<0.1	0.3	0.3	<0.1	0.3	<0.1	<0.1
Hf	1.4	1.1	1.0	1.0	1.5	1.1	1.2	2.1	1.7	1.0	1.7	1.4	1.6
Th	3	2	2	3	2	2	3	4	4	3	4	2	2
U	1	1	<1	1	<1	<1	<1	1	2	<1	2	<1	<1

Analyzed by B. Chappell, ANU.

Table 3. (continued)

38B	39A	40	41A	41B	42A	42B	43B	44	45A	45B	46	47
38-4	39-1	40-1	41-3	41-1	42-3	42-1	43-1	44-1	45-2	45-1	46-2	47-1
2.0	1.80	2.6	2.1	10.1	2.0	2.1	3.3	1.75	3.4	1.65	4.9	3.4
6.9	5.9	7.2	6.1	33.5	6.3	6.5	10.4	5.3	10.8	5.5	15.5	9.9
3.05	2.75	2.60	2.10	12.1	2.70	2.80	4.20	2.35	4.50	2.60	6.8	4.15
1.1	1.03	0.96	0.74	3.5	0.99	1.01	1.42	0.87	1.57	0.97	2.25	1.37
4.1	3.7	3.4	2.6	16	3.7	3.8	5.5	3.3	5.9	3.6	9.0	5.4
1.25	1.10	0.85	0.75	4.1	0.95	1.00	1.60	0.95	1.70	1.10	2.5	1.50
3.75	3.25	3.05	2.50	14.6	3.15	3.45	5.3	2.95	5.1	3.20	8.1	5.1
0.60	0.54	0.47	0.40	2.05	0.51	0.53	0.78	0.47	0.81	0.51	1.22	0.77
48	47	40	40	15	46	45	45	43	42	46	42	45
<0.1	<0.1	<0.1	<0.1	<0.1	<0.1	<0.1	<0.1	<0.1	<0.1	<0.1	<0.1	<0.1
1.5	1.4	1.3	1.0	9	1.3	1.4	2.4	1.2	2.4	1.3	3.6	2.2
2	3	3	<2	3	2	<2	2	2	4	2	2	2
<1	<1	<1	<1	<1	1	<1	1	<1	<1	<1	2	1

Figure 9. Trace element variations versus Mg # (Mg / (Mg + Fe^{2+})) for Manus Basin whole-rock data of Table 2. Solid lines represent observed fractionation trends for the MORB suite. X-BABB shown in enclosed field. Symbols are: (x) MORB, (o) BABB and (*) X-BABB.

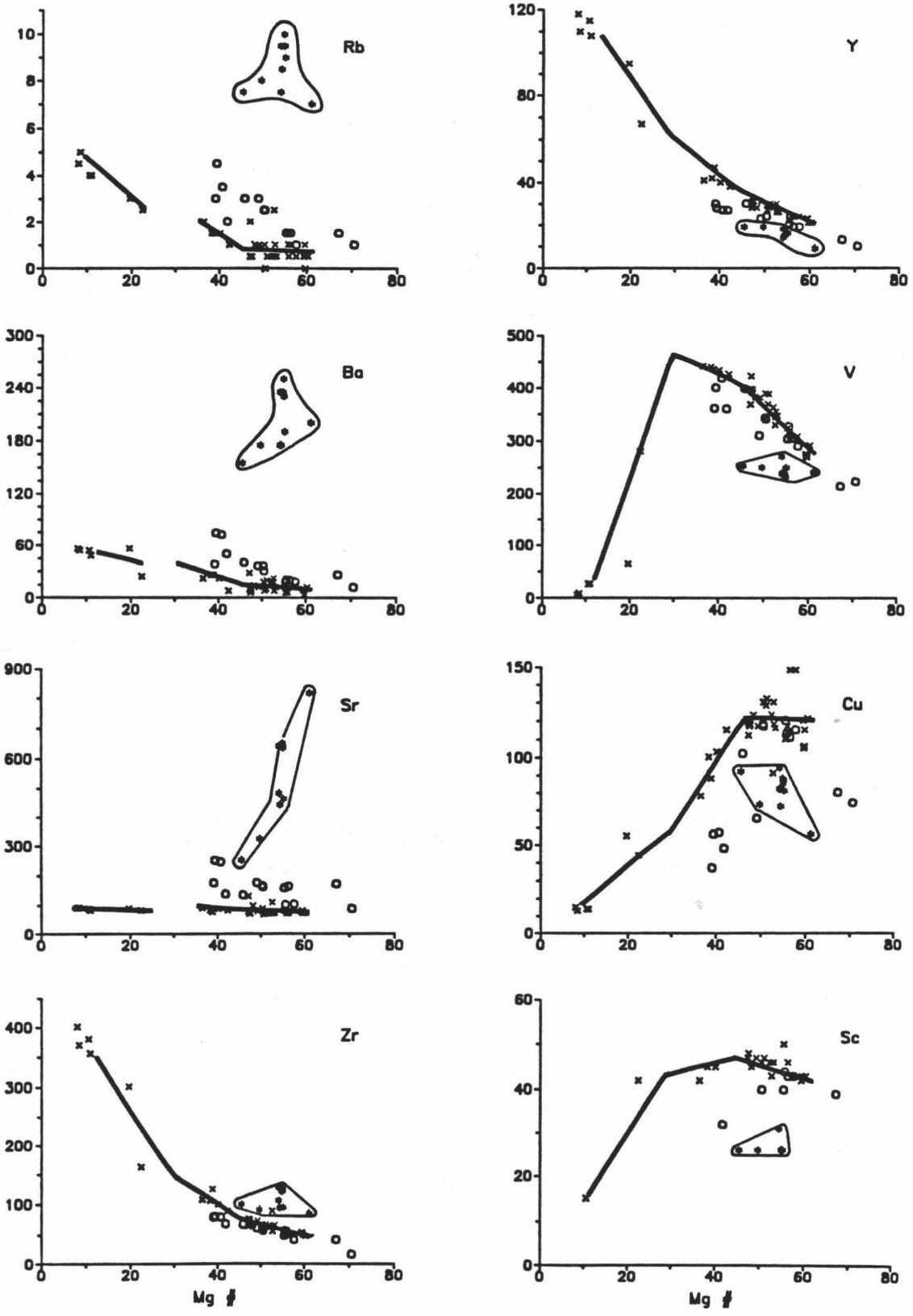
Rb
Y
Ba
V
Sr
Cu
Zr
Sc
Mg #
Mg #

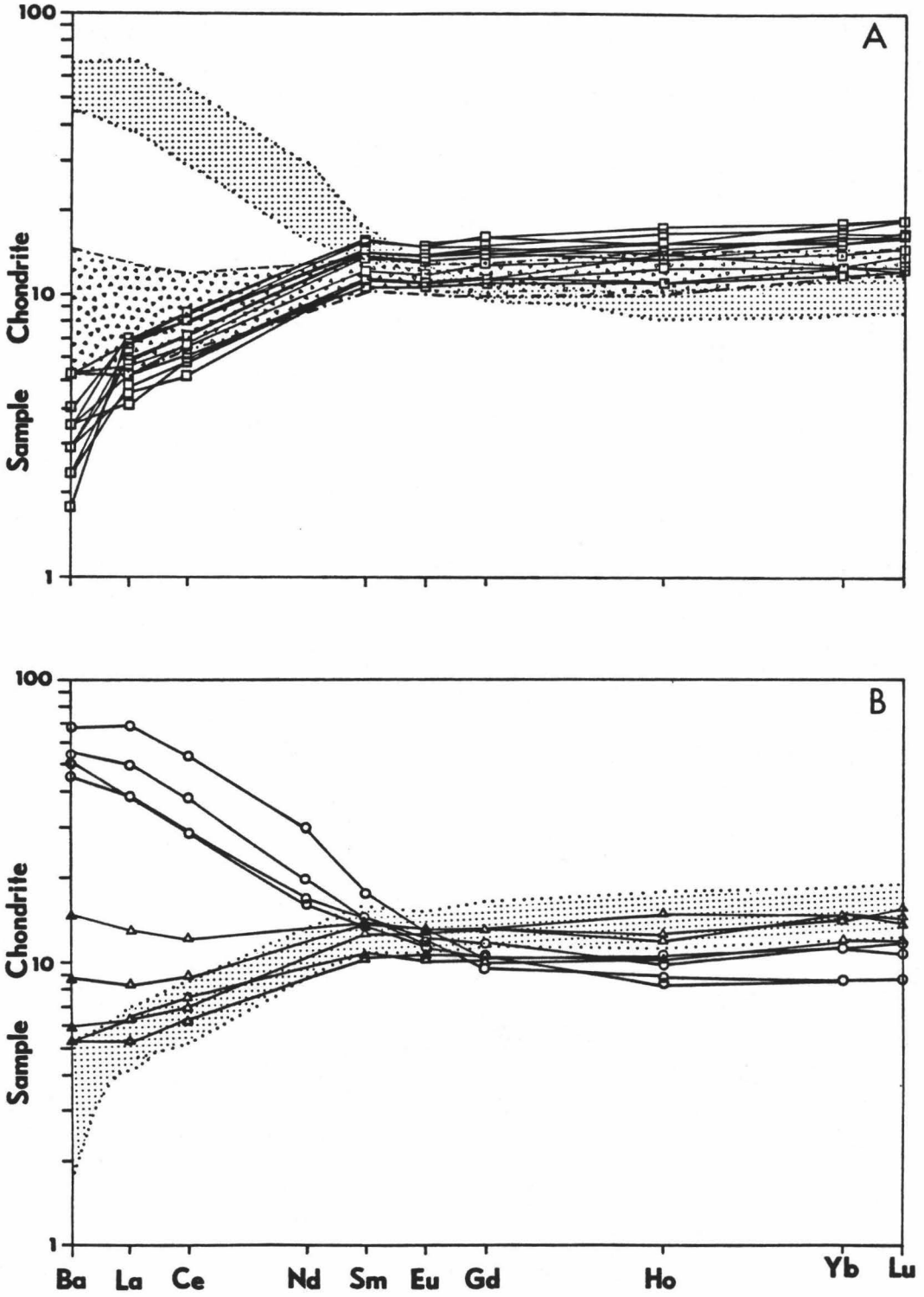

Figure 10. Chondrite-normalized Ba-rare earth element plot for samples from the Extensional Transform Zone and Manus Spreading Center. Rare earth normalization values from Boynton (1984). (a) MORB patterns shown with BABB and X-BABB fields, and (b) BABB and X-BABB patterns shown with MORB field. Symbols are: (□) MORB, (Δ) BABB, (o) X-BABB.

Table 4. Volatile Abundances of Volcanic Glasses from the Extensional Transform Zone and Manus Spreading Center by Mass Spectroscopy

Sample	29-3	31-1	31-8	33-2	24-9	35-4	36-2	36-4	36-8	38-8	40-6
Group	29A	31A	31C	33C	24B	35A-3	36A	36D	36C	38C-1	40
H2O	0.187	0.614	1.152	1.243	1.828	1.578	0.303	1.704	0.601	1.243	1.366
CO2	0.072	0.083	0.025	0.011	0.009	0.011	0.074	0.027	0.044	0.064	0.023
S	0.068	0.091	0.022	0.023	0.000	0.011	0.064	0.007	0.114	0.074	0.061
Cl	0.046	0.067	0.049	0.130	0.190	0.124	0.084	0.155	0.146	0.148	0.155
F	0.005	0.008	0.003	0.003	0.012	0.007	0.005	0.012	0.001	0.005	0.004
Total	0.378	0.863	1.251	1.410	2.039	1.731	0.530	1.905	0.919	1.534	1.609

Analyzed by K. Aggrey, U.H. Chemistry Dept.

41-1	41-3	42-1	43-1	45-2	46-2	47-1
41B	41A	42B	43B	45A	46	47
1.468	1.333	0.807	1.070	1.738	1.065	0.507
0.013	0.007	0.012	0.022	0.022	0.009	0.001
0.016	0.057	0.090	0.080	0.064	0.106	0.144
0.333	0.212	0.147	0.217	0.271	0.265	0.179
0.006	0.022	0.012	0.009	0.006	0.015	0.021
1.836	1.631	1.068	1.398	2.101	1.460	0.862

Seven chemical groups from the ETZ, showing characteristics of BABB, were recovered in Dredges 29 (Group B), 30 (Groups A, B, and C), 31 (Group C), 33 (Group C) and 34 (see Table 1). These dredges were from the shallowest portion of the ETZ (Fig.5a). The rest of the ETZ samples correspond to a MORB-type lithology (Fig.6, 7). These lavas are essentially the nonvesicular basaltic lavas in the Manus Basin. All the ETZ samples have relatively low concentrations of K_2O (< 0.22 wt. %) (Fig.6a).

Fifteen BABB-type groups (including seven X-BABB groups) were recovered from the MSC. These lavas were from the intermediate to shallowest portions of the ridge, respectively (Fig.5b). MORB-type lavas were recovered all along the MSC except on the shallowest portion of the spreading center.

X-BABB lavas, erupted on the shallowest portion of the MSC, have less than 5.5 wt. % MgO. The MgO content of the BABB lavas on the MSC increase away from the shalllowest point, suggesting MgO correlates with depth for BABB.

PETROGRAPHY

All of the Extensional Transform Zone (ETZ) samples collected for this study are either basalts or basaltic andesites with a range of vesicle sizes and abundances. A summary of the petrographic descriptions of the dredge samples from the ETZ is presented in Table 5. Dredges 26 and 27 lava are very sparsely phyric, containing microglomeroporphyritic plagioclase, olivine and clinopyroxene. In addition to anhedral, euhedral and elongate olivines, there also are skeletal olivine microphenocrysts present in all ETZ lavas. Dredge 29 lavas are mineralogically

Table 5. Petrographic Descriptions of Dredge Samples from the Extensional Transform Zone

Group	Sample	Sequence* (Vesicularity)	Mineral descriptions
26	26-5	ol, pl, cpx	ol: subhedral to euhedral; few skeletal forms pl: thin blades; subhedral crystals; twinning & zoning; clusters with cpx, sometimes olivine cpx: sector-zoning; anhedral to subhedral (some rounded?); possibly pigeonite too; lots of inclusions
26	26-14	ol, pl, cpx	ol: anhedral to subhedral; clustered with pl, sometimes with cpx pl: acicular blades; clustered with cpx, ol cpx: sector-zoning; some inclusions; may form as tiny aggregates grouped together with pl
27	27-5	ol, pl, cpx	ol: some anhedral/ euhedral; skeletal (with tails); elongate pl: blades with glass inclusions; some clustering with ol cpx: anhedral to subhedral; couple of rounded sector-zoned crystals; clustered with pl
29A	29-3	ol, pl (1-2%, 2 mm size)	ol: anhedral to euhedral; seems to be a very unstable phase; lots of fractures; inclusions (oxides) pl: subhedral; edges irregular; some glass inclusions; usually clustered with ol

*Note: ol, olivine; pl, plagioclase; cpx, clinopyroxene.

Table 5. (continued)

29B	29-5	ol, pl, cpx (1-2%, 2 mm size)	ol: subhedral to euhedral; few skeletal/elongate pl: anhedral to subhedral; clusters with cpx cpx: tiny, anhedral crystals; clusters with pl
30A	30-2	ol, pl, cpx (30-50%)	ol: skeletal forms pl: subhedral; twinning; may cluster with cpx cpx: anhedral to subhedral; may be clustered with pl
30B	30-3	ol, pl, cpx (30-50%)	ol: few, subhedral to euhedral pl: thin blades cpx: anhedral; clusters with other cpx or sometimes pl
30B	30-4	ol, pl, cpx (30-50%)	ol: few, subhedral to euhedral pl: thin blades; may cluster with other pl or cpx cpx: tiny, anhedral; usually clusters with pl
31A	31-1	ol, pl, cpx (5-10%, 2-3 mm size)	ol: anhedral to euhedral pl: thin, jagged blades; clustered with cpx (sometimes with ol) cpx: occur as tiny crystals; also anhedral, larger crystals; zoning; clustered with pl
31B	31-3	ol, pl, cpx (5-10%, 2-3 mm size)	ol: very large phenocryst (euhedral); others are anhedral; "holes" pl: anhedral to subhedral; twinning; clusters with cpx cpx: clusters with pl

Table 5. (continued)

31C	31-8	ol, pl, cpx (5-10%, 2-3 mm size)	ol: skeletal and subhedral forms; occasionally clustered with pl and cpx pl: small, acicular blades usually clustered with cpx cpx: anhedral with a few euhedral forms; clustered with pl
32B	32-1	ol, pl (1%, 1 mm size)	ol: subhedral to euhedral; some skeletal forms; usually clusters with pl pl: blades (microphenocrysts) & endsections (phenocrysts); some are rounded; may cluster with other pl or ol
32A	32-2	ol, pl (cpx-out of equil. phase) (1%, 1 mm size)	ol: anhedral to subhedral pl: blades; twinning; may cluster with ol or cpx cpx: quite a few rounded ones; sector-zoning
33A	33-1	ol, pl, cpx (40%, 4 mm size)	ol: skeletal crystals pl: tiny blades; sub-parallel alignment cpx: sector-zoning; clusters with pl
33C	33-2	ol, pl, cpx (40%, 4 mm size)	ol: few large phenocrysts; fractured; some glass inclusions; clusters with pl pl: acicular blades; shows some kind of flow structure around vesicles; few larger crystals show twinning and inclusions cpx: tiny crystals; clusters with pl

Table 5. (continued)

33B	33-3	ol, pl, cpx (1%, 1 mm size)	ol: subhedral; skeletal forms as well pl: thin blades; may cluster with cpx; other subhedral grains cluster together cpx: anhedral to subhedral; clusters with pl
34	34-1	ol, pl (1-2%, 2 mm size)	ol: subhedral; may cluster with pl; some skeletal forms pl: blades; some forming "tails" at corners; subhedral grains also occur in slide; may cluster with pl or ol

bimodal; one group of lavas contain plagioclase and olivine and the other group also includes clinopyroxene. Vesicular, aphyric lavas of Dredge 30 are the only basaltic andesites recovered from the ETZ. Petrographic inspection revealed that these aphyric lavas contain olivine, plagioclase and clinopyroxene. The slightly vesicular (5-10%, about 2-3 mm) basaltic pillow lavas of Dredge 31 are slightly phyric with plagioclase, olivine and clinopyroxene.

Dredge 32 lavas are very porphyritic, containing phenocrysts of plagioclase (40-50%, up to 15 mm) and olivine. Only two of the five samples from this dredge are slightly porphyritic. There are two types of lavas in Dredge 33. Vesicular (40%, 4 mm) lavas contain plagioclase, clinopyroxene, and olivine. In addition, some glomeroporphyritic plagioclase and clinopyroxene are present. Nonvesicular lavas contain plagioclase with only rare olivines and clinopyroxenes. The moderately-vesicular lavas of Dredge 34 also include some pipe vesicles (1-2%, 2 mm) rimming one-inch from the glassy surface. Pipe vesicles suggest that the cooling front of the lava was slow (Philpotts and Lewis, 1987). These lavas are slightly plagioclase-phyric with some olivine present.

Several differences between the dredge sites of the ETZ can be discerned from the petrography. First, the vesicular lavas were recovered only on the bathymetric "high" (~1900 m) of the ETZ. Second, at the ends of the ETZ (where the ETZ terminates to the west at the Willaumez Transform, and to the east at the Manus Spreading Center) are areas where only olivine and plagioclase crystallizing phases are observed. Third, all the dredge sites, except at Dredge Site 30, included nonvesicular lavas.

MINERAL CHEMISTRY

Olivine

Representative olivine analyses of the ETZ are presented in Table 6. Olivine is present in all samples and the olivine compositions range from Fo_{71} to Fo_{90}. Individual olivine phenocrysts did not show any observable zoning; skeletal phenocrysts are present in all the ETZ samples. There is a general positive correlation between forsterite content of the olivines and Mg # ($Mg/(Mg + Fe^{2+})$) of the host glass (Fig.11). The observed relationship is consistent with olivine-liquid equilibrium (Roeder and Emslie, 1970). The Fe-Mg exchange partition coefficient between olivine and glass ($K_D = Fe^{ol}Mg^{liq} / Mg^{ol}Fe^{liq}$) is 0.25 for six samples each from both MORB and BABB lava suites, calculated with Fe^{liq} as total Fe (Fig.11). This value falls within the range determined by Perfit and Fornari (1983) and Bender et al. (1978) for basalts from major ocean spreading centers and high-temperature olivine-melt pairs in experimental investigations of a FAMOUS basalt. Temperatures calculated using the olivine-glass geothermometer (Bender et al., 1978) indicate that the phenocrysts crystallized at progressively decreasing temperature (Table 7). Temperatures based on the Fe partitioning between olivine and melt are higher than those calculated from Mg partitioning considerations by 22^{o} - $86^{o}C$ for ETZ MORB and BABB lavas.

Table 6a. Representative Olivine Analyses of Manus MORB

Sample	32-2			32-1		33-3	27-5	31-1	
Analysis#	1	3	6	1	5	4	6	2	3
Mg#glass	58.33	58.33	58.33	56.31	56.31	53.45	53.50	50.97	50.97
SiO2	38.99	39.31	39.38	39.60	39.73	38.99	38.99	38.89	38.93
FeO	15.27	15.51	14.46	15.60	15.77	15.99	15.89	17.57	17.61
MgO	43.55	44.06	44.58	43.97	43.86	43.44	42.80	42.60	42.50
CaO	0.18	0.17	0.17	0.18	0.17	0.17	0.17	0.18	0.17
NiO	0.11	0.15	0.15	0.16	0.20	0.10	0.15	0.11	0.13
Total	98.10	99.20	98.74	99.51	99.73	98.69	98.00	99.35	99.34
				Cations on the basis of 4 oxygens					
Si	1.000	0.998	0.999	1.002	1.003	0.997	1.004	0.996	0.997
Fe2	0.328	0.329	0.307	0.330	0.333	0.342	0.342	0.376	0.377
Mg	1.665	1.667	1.686	1.658	1.651	1.656	1.642	1.625	1.622
Ca	0.005	0.005	0.005	0.005	0.005	0.005	0.005	0.005	0.005
Ni	0.002	0.003	0.003	0.003	0.004	0.002	0.003	0.002	0.003
Sum	3.000	3.002	3.001	2.998	2.997	3.003	2.996	3.004	3.003
Fo	83.6	83.5	84.6	83.4	83.2	82.9	82.8	81.2	81.1
Z	1.000	0.998	0.999	1.002	1.003	0.997	1.004	0.996	0.997
Y	2.000	2.004	2.001	1.996	1.993	2.005	1.992	2.009	2.006

Analyzed by L. Liu, HIG.

Table 6b. Representative Olivine Analyses of Manus BABB

Sample	31-8		29-5	30-2		30-3		30-4		33-2	33-1	34-1	
Analysis#	3	4	2	2	5	1	4	1	3	1	1	2	4
Mg#glass	67.53	67.53	61.36	47.43	47.43	38.37	38.37	37.88	37.88	37.80		54.37	54.37
SiO2	40.37	40.24	39.70	37.46	38.67	37.50	37.27	37.10	37.94	37.47	37.37	39.45	39.24
FeO	10.52	10.43	13.35	25.01	18.86	26.21	26.44	25.98	22.74	24.91	25.44	15.51	15.30
MgO	48.13	47.99	46.09	36.00	41.38	36.16	35.93	35.60	38.35	36.29	36.58	44.06	43.86
CaO	0.16	0.17	0.14	0.16	0.12	0.15	0.15	0.16	0.15	0.14	0.13	0.15	0.16
NiO	0.25	0.23	0.26	0.05	0.06	0.01	0.03	0.02	0.00	0.08	0.05	0.16	0.15
Total	99.43	99.06	99.54	98.68	99.09	100.03	99.82	98.86	99.18	98.89	99.57	98.33	98.71
Cations on the basis of 4 oxygens													
Si	0.999	0.999	0.995	1.001	0.998	0.993	0.991	0.995	0.997	0.999	0.992	1.000	1.000
Fe2	0.218	0.217	0.280	0.559	0.407	0.581	0.588	0.583	0.500	0.555	0.565	0.329	0.326
Mg	1.775	1.776	1.722	1.434	1.592	1.428	1.424	1.423	1.502	1.442	1.447	1.664	1.666
Ca	0.004	0.005	0.004	0.005	0.003	0.004	0.004	0.005	0.004	0.004	0.004	0.004	0.004
Ni	0.005	0.005	0.005	0.001	0.001	0.000	0.001	0.000	0.000	0.002	0.001	0.003	0.003
Sum	3.001	3.001	3.005	2.999	3.002	3.007	3.009	3.005	3.003	3.001	3.008	3.000	3.000
Fo	89.1	89.1	86.0	72.0	79.6	71.1	70.8	70.9	75.0	72.2	71.9	83.5	83.6
Z	0.999	0.999	0.995	1.001	0.998	0.993	0.991	0.995	0.997	0.999	0.992	1.000	1.000
Y	2.002	2.002	2.010	1.998	2.004	2.013	2.017	2.010	2.006	2.003	2.016	2.000	2.000

Analyzed by L. Liu, HIG.

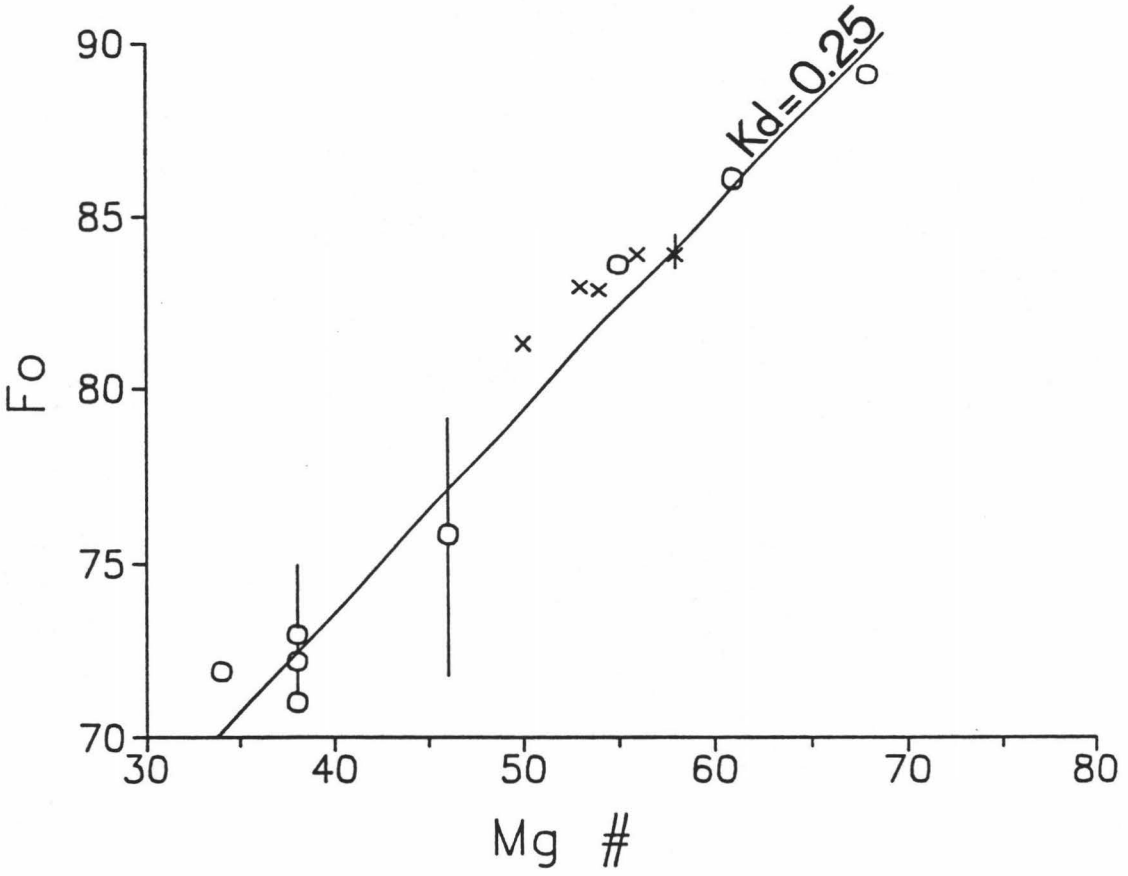

Figure 11. Average olivine forsterite composition versus Mg # (Mg / (Mg + Fe^{2+})) in coexisting glasses. Range of Fo composition is shown for each averaged sample plotted; averaged samples with no ranges shown overlap plotted symbol. Symbols are: (x) MORB and (o) BABB.

Table 7. Olivine-Glass Geothermometry for Extensional Transform Zone MORB and BABB olivines

Sample	Temperature (Bender et al., 1978) (in degrees Celsius)	
MORB (ave.)	Mg	Fe
32-2	1165	1187
32-1	1154	1191
33-3	1137	1197
27-5	1147	1195
31-1	1132	1187
BABB (ave.)	Mg	Fe
31-8	1164	1197
29-5	1123	1179
30-2	1082	1127
30-3	1094	1127
30-4	1049	1135
33-2	1043	1129
34-1	1138	1193

Plagioclase

The compositional range for all ETZ plagioclase phenocrysts is An_{70} to An_{90} (Table 8). Many of the plagioclase phenocrysts show some sort of chemical zoning but most of the rims were too thin ($\leq$ 4 um) to analyze by electron microprobe. Of the plagioclase rims that could be analyzed, most of the zoning in plagioclase was normal with calcic cores and sodic rims; only one sample (#32-1) had reversed zoning. "H"-type (skeletal-shaped) plagioclase occurs in many of the ETZ lavas, especially as part of the groundmass.

The concentration of Fe in plagioclase slightly increases with decreasing anorthite (An) content. The increase in Fe content in plagioclase may be a consequence of increasing Fe content in residual liquids during crystallization of a magma. The slight overlap between the MORB and BABB trends (Fig.12) can be explained by the nonperfect equilibrium crystallization of plagioclase in both suites. At a given An content, MORB plagioclase has slightly lower Fe concentration than BABB plagioclase. The Fe concentration of plagioclase mainly reflects the Fe concentration of the melt from which it grows. This can be seen in Figure 12b that BABB magmas grow more calcic plagioclase than MORB magmas with the same FeO^* concentrations. The composition of plagioclase is sensitive to magmatic H_2O contents such that an increase in water promotes the crystallization of a more calcic plagioclase (Yoder and Tilley, 1962; Green and Ringwood, 1968). The fractionation of augite will cause the continual decrease of Ca/Na in residual liquids, and therefore, in plagioclase crystallizing from these melts. Plagioclase An contents also decreases with decreasing temperature.

Table 8a. Representative Plagioclase Analyses of Manus MORB

Sample	32-2-1	32-2-3	32-1-1		32-1-2	33-3-3			27-5-1	27-5-2	31-1-2	31-1-3
Analysis#	5	3	2	4	3	1	2	3	3	2	2	2
SiO2	49.06	47.80	48.40	48.71	48.56	50.26	49.89	50.14	49.81	49.97	50.38	51.02
Al2O3	33.01	33.55	31.72	31.46	31.30	30.86	31.05	30.93	31.25	31.28	31.00	30.96
FeO	0.40	0.33	0.59	0.56	1.14	0.80	0.86	0.88	0.73	0.76	0.80	0.79
MgO	0.24	0.23	0.15	0.15	0.14	0.14	0.13	0.14	0.13	0.14	0.15	0.11
CaO	16.02	16.68	15.23	14.77	14.90	14.44	14.71	14.60	14.90	14.50	14.11	14.20
Na2O	2.01	1.61	2.62	2.81	2.66	3.09	2.96	3.04	2.97	3.06	3.23	3.23
K2O	0.01	0.00	0.00	0.03	0.00	0.00	0.00	0.06	0.00	0.09	0.06	0.15
Total	100.75	100.20	98.71	98.49	98.70	99.59	99.60	99.79	99.79	99.80	99.73	100.46
					Cations on the basis of 8 oxygens							
Si	2.226	2.186	2.245	2.262	2.257	2.305	2.291	2.298	2.283	2.289	2.306	2.319
Al	1.766	1.808	1.734	1.722	1.714	1.668	1.680	1.671	1.688	1.689	1.673	1.658
Fe2	0.015	0.013	0.023	0.022	0.044	0.031	0.033	0.034	0.028	0.029	0.031	0.030
Mg	0.016	0.016	0.010	0.010	0.010	0.010	0.009	0.010	0.009	0.010	0.010	0.007
Ca	0.779	0.817	0.757	0.735	0.742	0.710	0.724	0.717	0.732	0.712	0.692	0.691
Na	0.177	0.143	0.236	0.253	0.240	0.275	0.264	0.270	0.264	0.272	0.287	0.285
K	0.001	0.000	0.000	0.002	0.000	0.000	0.000	0.004	0.000	0.005	0.004	0.009
Sum	4.980	4.982	5.005	5.005	5.006	4.998	5.001	5.003	5.004	5.005	5.002	4.999
Z	3.992	3.994	3.980	3.983	3.971	3.973	3.971	3.969	3.972	3.978	3.979	3.977
X	0.988	0.988	1.026	1.022	1.035	1.025	1.029	1.034	1.033	1.027	1.023	1.022
An	81.4	85.1	76.3	74.3	75.6	72.1	73.3	72.4	73.5	72.0	70.5	70.2
Ab	18.5	14.9	23.7	25.6	24.4	27.9	26.7	27.3	26.5	27.5	29.2	28.9
Or	0.1	0.0	0.0	0.2	0.0	0.0	0.0	0.4	0.0	0.5	0.4	0.9

Analyzed by L. Liu, HIG.

Table 8b. Representative Plagioclase Analyses of Manus BABB

Sample	31-8-1		31-8-3	29-5-1	29-5-2	29-5-3	30-2-1	30-3-1		30-4-1	33-2-1	33-2-2	33-1-2	34-1-2
Analysis#	1	3	2	4	2	2	1	1	2	2	3	4	1	1
SiO2	46.36	45.52	46.01	49.27	48.61	48.98	48.17	50.46	50.29	50.26	48.85	51.11	51.43	49.27
Al2O3	34.01	34.69	34.42	31.98	32.52	31.54	33.46	31.79	31.62	32.00	32.48	30.23	29.89	32.37
FeO	0.54	0.66	0.47	0.93	0.70	0.77	0.79	0.79	0.79	0.82	0.89	0.88	1.32	0.63
MgO	0.16	0.12	0.13	0.17	0.15	0.16	0.17	0.11	0.16	0.11	0.05	0.05	0.10	0.25
CaO	17.37	18.16	18.39	15.51	15.60	15.26	16.69	14.67	14.90	14.97	15.48	13.31	13.26	15.75
Na2O	1.30	1.08	1.09	2.49	2.53	2.59	1.71	2.89	2.77	2.57	2.45	3.59	3.88	2.19
K2O	0.12	0.00	0.00	0.02	0.02	0.03	0.00	0.01	0.01	0.04	0.06	0.03	0.06	0.02
Total	99.86	100.23	100.51	100.37	100.13	99.33	100.99	100.72	100.54	100.77	100.26	99.20	99.94	100.48
Cations on the basis of 8 oxygens														
Si	2.138	2.098	2.113	2.250	2.226	2.259	2.190	2.288	2.285	2.278	2.234	2.347	2.352	2.244
Al	1.848	1.884	1.863	1.722	1.755	1.714	1.793	1.699	1.694	1.709	1.751	1.636	1.611	1.737
Fe2	0.021	0.025	0.018	0.036	0.027	0.030	0.030	0.030	0.030	0.031	0.034	0.034	0.050	0.024
Mg	0.011	0.008	0.009	0.012	0.010	0.011	0.012	0.007	0.011	0.007	0.003	0.003	0.007	0.017
Ca	0.858	0.897	0.905	0.759	0.765	0.754	0.813	0.713	0.726	0.727	0.758	0.655	0.650	0.768
Na	0.116	0.096	0.097	0.221	0.225	0.232	0.151	0.254	0.244	0.226	0.217	0.320	0.344	0.193
K	0.007	0.000	0.000	0.001	0.001	0.002	0.000	0.001	0.001	0.002	0.004	0.002	0.003	0.001
Sum	5.000	5.009	5.004	5.000	5.009	5.001	4.989	4.991	4.990	4.981	5.001	4.996	5.017	4.985
Z	3.986	3.982	3.976	3.972	3.981	3.973	3.983	3.986	3.979	3.988	3.985	3.983	3.962	3.981
X	1.013	1.027	1.029	1.028	1.028	1.028	1.005	1.005	1.011	0.994	1.017	1.013	1.054	1.004
An	87.4	90.3	90.3	77.4	77.2	76.4	84.4	73.7	74.8	76.1	77.5	67.1	65.2	79.8
Ab	11.8	9.7	9.7	22.5	22.7	23.5	15.6	26.3	25.2	23.6	22.2	32.7	34.5	20.1
Or	0.7	0.0	0.0	0.1	0.1	0.2	0.0	0.1	0.1	0.2	0.4	0.2	0.4	0.1

Analyzed by L. Liu, HIG.

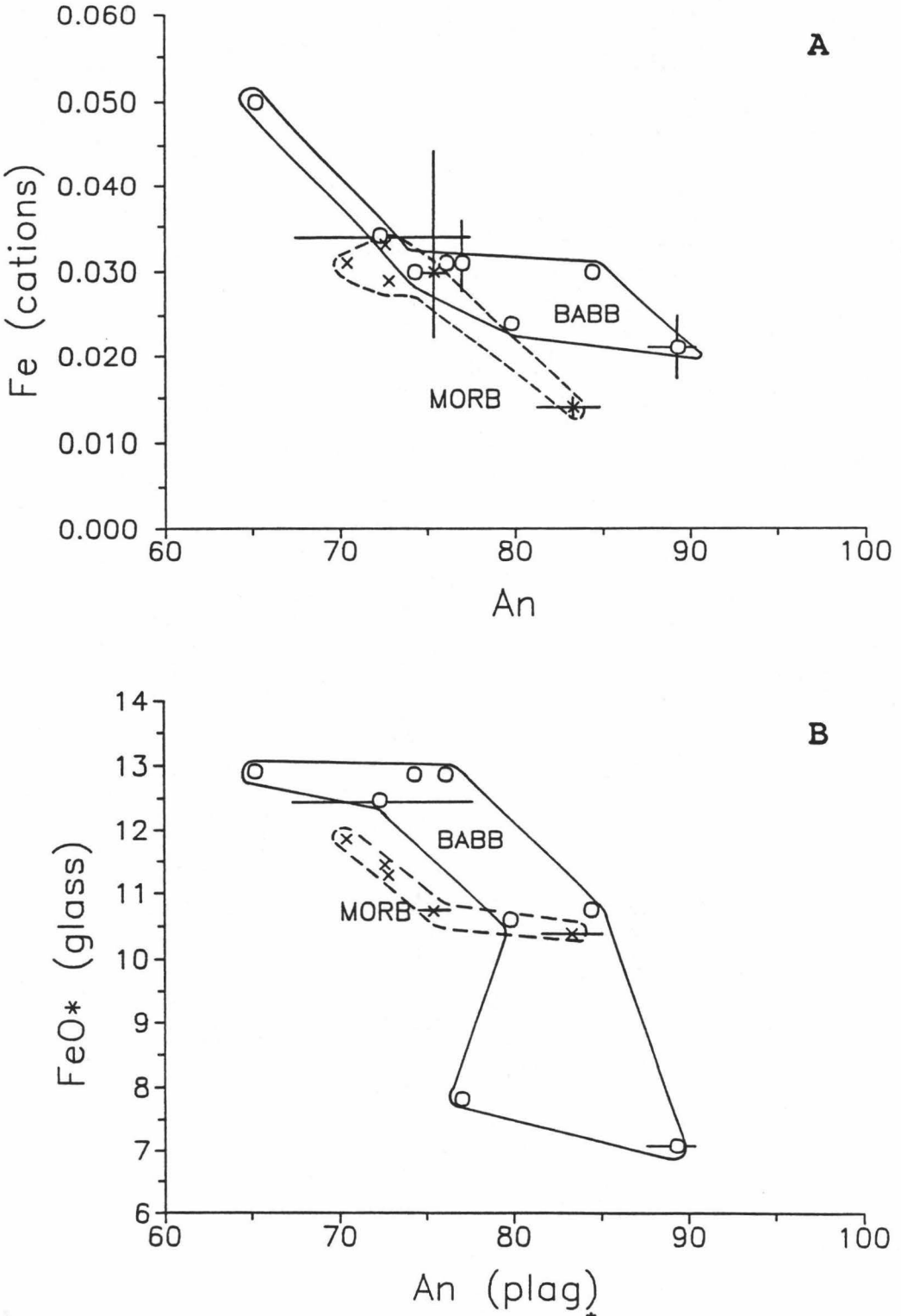

Figure 12. (a) Fe (plagioclase) versus An and (b) FeO^* (host glass) versus An for averaged plagioclase. Range of Fe and An content is shown for each averaged sample plotted; averaged samples with no ranges shown overlap plotted symbol. Symbols are the same as in Figure 11.

Clinopyroxene

The clinopyroxene compositions vary considerably in Mg # and in the concentrations of TiO_2, Al_2O_3, Cr_2O_3, FeO, CaO and Na_2O (Table 9). The phenocrysts vary from augites to subcalcic augites. Crystallization of subcalcic augites may represent metastable products formed during quenching of the liquid (Williams et al., 1982; Perfit and Fornari, 1983) or formation at higher temperatures than augites. Sector-zoned pyroxenes occur in many samples; this type of zoning may also indicate pyroxene crystallization from a supercooled magma (Bryan, 1972). The increase in Ti in the pyroxene, combined with decreasing Mg # in both clinopyroxene and its host glass (Fig.13), is controlled by the increase in Ti of the liquid with differentiation. This results from the early differentiation of Ti-free minerals olivine and plagioclase. The trend of the BABB group is displaced to lower concentrations of Ti with respect to the MORB group. This offset is probably due to the higher Ti content in liquids of the MORB group during crystallization compared to BABB. High concentrations of Ti and Al may also be due to rapid cooling of the liquid (Bryan, 1972). The overall trend of Ca in pyroxenes from the ETZ decreases with decreasing Mg #; this trend results from Na^{2+} substitution for Ca^{2+} in the pyroxene. This effect is especially prominant in the BABB suite.

Table 9a. Representative Clinopyroxene Analyses of Manus MORB

Sample	32-2-1	32-2-2	32-2-3	33-3-2	33-3-3	27-5-2		31-1-3	
Analysis#	5	4	1	3	2	2	4	1	2
SiO2	53.63	51.87	53.50	52.15	51.87	52.29	51.32	51.80	52.03
TiO2	0.23	0.37	0.24	0.34	0.41	0.36	0.49	0.57	0.46
Al2O3	2.52	4.13	2.52	2.91	3.63	3.04	4.37	3.58	3.35
Cr2O3	0.96	1.65	1.07	0.36	0.33	0.73	0.59	0.57	0.80
FeO	6.38	4.13	5.41	6.05	6.67	6.01	6.13	6.15	6.05
MnO	0.21	0.17	0.16	0.10	0.20	0.11	0.10	0.21	0.26
MgO	19.49	17.07	18.46	18.29	18.35	17.20	17.44	17.13	16.93
CaO	17.44	20.18	19.35	18.74	17.86	19.44	19.07	19.55	19.92
Na2O	0.16	0.24	0.21	0.18	0.21	0.23	0.19	0.21	0.23
Total	101.02	99.81	100.92	99.12	99.53	99.41	99.70	99.77	100.03
Cations on the basis of 6 oxygens									
Si	1.931	1.892	1.931	1.919	1.902	1.923	1.882	1.901	1.907
Alz	0.069	0.108	0.069	0.081	0.098	0.077	0.118	0.099	0.093
Aly	0.038	0.070	0.039	0.045	0.059	0.055	0.071	0.056	0.052
Ti	0.006	0.010	0.007	0.009	0.011	0.010	0.014	0.016	0.013
Cr	0.027	0.048	0.031	0.010	0.010	0.021	0.017	0.017	0.023
Fe	0.192	0.126	0.163	0.186	0.205	0.185	0.188	0.189	0.185
Mn	0.006	0.005	0.005	0.003	0.006	0.003	0.003	0.007	0.008
Mg	1.046	0.928	0.993	1.003	1.003	0.943	0.953	0.937	0.925
Ca	0.673	0.789	0.748	0.739	0.702	0.766	0.749	0.769	0.782
Na	0.011	0.017	0.015	0.013	0.015	0.016	0.014	0.015	0.016
Sum	4.001	3.993	4.000	4.010	4.011	3.999	4.008	4.005	4.005
Z	2.000	2.000	2.000	2.000	2.000	2.000	2.000	2.000	2.000
Y	1.317	1.187	1.237	1.258	1.294	1.217	1.246	1.221	1.206
X	0.684	0.806	0.763	0.752	0.717	0.782	0.763	0.784	0.799
M/M+F	84.5	88.0	85.9	84.3	83.1	83.6	83.5	83.2	83.3
Ca	35.1	42.7	39.2	38.3	36.6	40.4	39.6	40.4	41.2
Mg	54.6	50.2	52.0	51.9	52.4	49.7	50.3	49.3	48.7
Fe	10.4	7.1	8.8	9.8	11.0	9.9	10.1	10.3	10.2

Analyzed by L. Liu, HIG.

Table 9b. Representative Clinopyxroxene Analyses of Manus BABB

Sample	31-8-1		31-8-3		29-5-2	30-2-1	30-2-4		30-3-1	30-3-4	30-4-2	33-2-1	33-2-2	33-1-3
Analysis#	2	4	1	4	3	2	1	2	1	1	1	2	4	2
SiO2	51.22	51.72	52.08	52.95	52.95	53.32	52.40	53.98	53.22	51.10	51.90	50.38	50.79	49.15
TiO2	0.23	0.30	0.16	0.11	0.20	0.37	0.40	0.27	0.47	0.81	0.55	0.69	0.51	0.88
Al2O3	5.30	5.30	4.50	2.99	2.28	2.95	3.00	2.02	2.99	4.46	3.12	4.91	3.88	4.38
Cr2O3	1.60	1.09	1.41	1.04	0.93	0.00	0.00	0.00	0.00	0.00	0.03	0.03	0.00	0.00
FeO	3.83	4.05	4.15	3.43	4.60	11.57	9.23	10.76	12.44	11.65	11.89	13.39	9.95	11.97
MnO	0.03	0.13	0.16	0.16	0.04	0.36	0.22	0.31	0.33	0.30	0.41	0.31	0.22	0.27
MgO	16.82	17.51	18.94	18.88	18.67	21.95	19.82	24.34	19.19	15.73	18.50	17.70	16.74	15.25
CaO	21.16	20.44	18.87	20.21	19.97	9.96	14.04	7.59	11.97	15.75	12.68	10.77	16.20	17.14
Na2O	0.11	0.11	0.11	0.11	0.18	0.16	0.12	0.04	0.16	0.23	0.18	0.24	0.23	0.26
Total	100.30	100.65	100.38	99.88	99.82	100.64	99.23	99.31	100.77	100.03	99.26	98.42	98.52	99.30
Cations on the basis of 6 oxygens														
Si	1.861	1.868	1.880	1.920	1.930	1.928	1.925	1.955	1.939	1.894	1.925	1.888	1.902	1.855
Alz	0.139	0.132	0.120	0.080	0.070	0.072	0.075	0.045	0.061	0.106	0.075	0.112	0.098	0.145
Aly	0.088	0.093	0.072	0.048	0.028	0.054	0.055	0.041	0.067	0.089	0.061	0.105	0.073	0.050
Ti	0.006	0.008	0.004	0.003	0.005	0.010	0.011	0.007	0.013	0.023	0.015	0.019	0.014	0.025
Cr	0.046	0.031	0.040	0.030	0.027	0.000	0.000	0.000	0.000	0.000	0.001	0.001	0.000	0.000
Fe	0.116	0.122	0.125	0.104	0.140	0.350	0.284	0.326	0.379	0.361	0.369	0.420	0.312	0.378
Mn	0.001	0.004	0.005	0.005	0.001	0.011	0.007	0.010	0.010	0.009	0.013	0.010	0.007	0.009
Mg	0.911	0.942	1.019	1.020	1.014	1.183	1.085	1.314	1.042	0.869	1.023	0.989	0.934	0.858
Ca	0.824	0.791	0.730	0.785	0.780	0.386	0.553	0.295	0.467	0.626	0.504	0.432	0.650	0.693
Na	0.008	0.008	0.008	0.008	0.013	0.011	0.009	0.003	0.011	0.017	0.013	0.017	0.017	0.019
Sum	4.000	4.000	4.003	4.002	4.009	4.005	4.003	3.996	3.990	3.994	3.998	3.993	4.007	4.032
Z	2.000	2.000	2.000	2.000	2.000	2.000	2.000	2.000	2.000	2.000	2.000	2.000	2.000	2.000
Y	1.169	1.201	1.266	1.210	1.216	1.608	1.442	1.698	1.511	1.352	1.481	1.543	1.340	1.320
X	0.832	0.799	0.738	0.793	0.793	0.397	0.561	0.297	0.479	0.642	0.517	0.450	0.667	0.712
M/M+F	88.7	88.5	89.1	90.7	87.9	77.2	79.3	80.1	73.3	70.6	73.5	70.2	75.0	69.4
Ca	44.5	42.5	38.8	41.0	40.3	20.0	28.7	15.2	24.6	33.5	26.4	23.4	34.2	35.8
Fe	49.2	50.7	54.2	53.3	52.4	61.3	56.3	67.6	54.9	46.6	53.6	53.4	49.1	44.3
Mg	6.3	6.8	6.9	5.7	7.3	18.7	15.1	17.3	20.5	19.9	20.0	23.2	16.7	19.9

Analyzed by L. Liu, HIG.

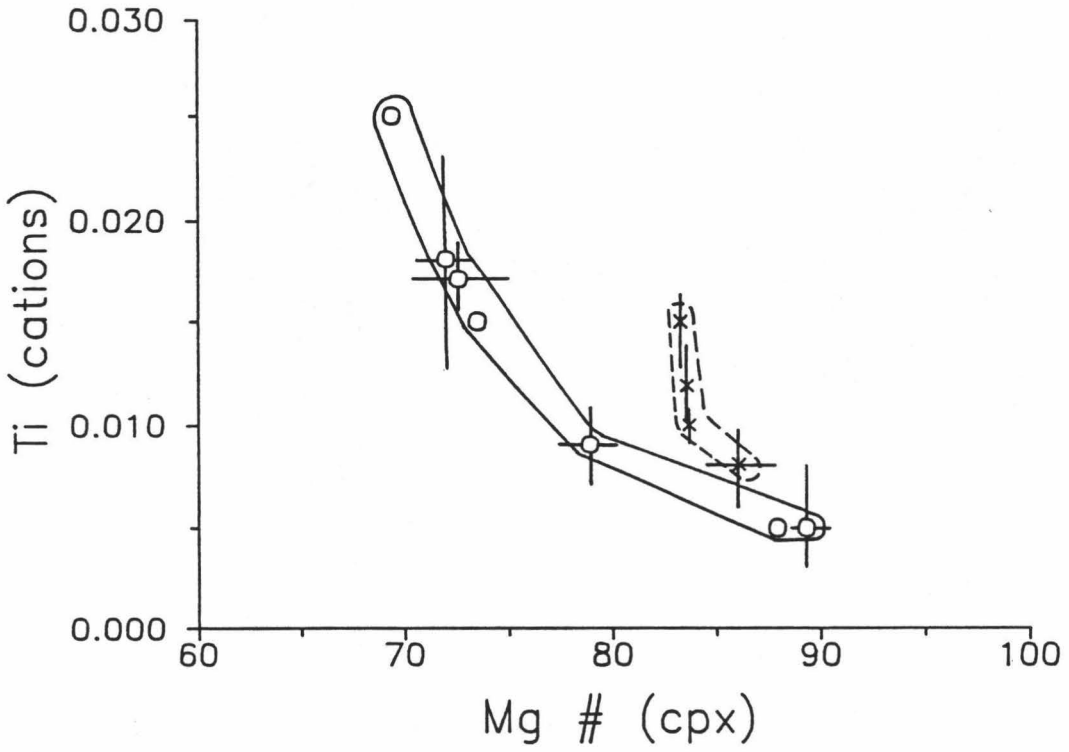

Figure 13. Ti versus Mg # of averaged clinopyroxene. Range of Ti content and Mg # is shown for each averaged sample plotted; samples with no ranges shown overlap plotted symbol. Symbols are the same as in Figure 11.

IV. DISCUSSION

FRACTIONATION TRENDS WITHIN THE ETZ

Fractionation is the process of chemical and mechanical evolution of a magma during crystallization and separation of crystals and liquid producing compositional variation within a magma. Compositional variability of Manus MORB and BABB glasses is illustrated by Figures 7 and 9. The distribution of TiO_2, K_2O and FeO^* reveal distinctive fractionation trends with the BABB lavas slightly offset to lower concentrations of TiO_2 and FeO^* and higher concentration of K_2O relative to MORB lavas. BABB lavas are about 3 wt. % lower in FeO^*, 0.7 wt. % lower in TiO_2 and 0.05 wt. % higher in K_2O compared to MORB lavas at 8 wt. % MgO. The inflection in the Sc trend (Fig.9) at Mg # (Mg / (Mg + Fe^{2+})) $\simeq$ 45 marks the point at which clinopyroxene joins olivine and plagioclase as a fractionating phase in the Manus MORB. Inflections in V and Cu also at Mg # $\simeq$ 45 in the Manus MORB probably indicate the incoming of clinopyroxene. The incoming of oxides as a fractionating phase is marked by the inflection of V at Mg # $\simeq$ 30. This may also be picked out by TiO_2 and FeO^* (Fig.7) at MgO $\simeq$ 3 wt. % (or Mg # $\simeq$ 23). The development of a slight Eu anomaly in the Manus MORB patterns (Fig.10) indicate the progression of plagioclase fractionation.

The presence of euhedral clinopyroxene phenocrysts, even in the most primitive BABB lava (Mg # = 68), indicates that BABB magmas reach clinopyroxene saturation at compositions that are relatively unmodified by shallow-level fractionation from their primary magmas. This can be explained by either derivation from shallow depths of melting (close to the 1 atm clinopyroxene-saturated cotectic)

or by fractionation at pressures significantly higher than 1 atm. In contrast, the MORB magmas are saturated with olivine, plagioclase and clinopyroxene only at moderately low Mg #'s (~45).

Fractionation Models

Quantitative modeling of fractionation can be performed by least squares regression of mineral compositions (Bryan et al., 1969; Wright and Doherty, 1970). A computer program, "IGPET", written by M. Carr (1985), based on least squares regression, was used to model fractionation of Extensional Transform Zone (ETZ) MORB and BABB. The method assumes that the glass compositions (representative of liquid compositions) are derived from a parent magma by removal or addition of chemical components, which go into the mineral phases. A disadvantage of the model is that there may be a compositional "gap" in the natural samples collected. Therefore, as fractionation proceeds the variation in mineral compositions may be discontinuous. The results of the calculations are presented in Table 10 and shown on Figure 7. Averaged glass compositions of the sample's group and the sample's constituent mineral phases were used in each fractionation step.

Two major liquid lines of descent, or paths, were attempted and calculated for a limited number of samples confined to the lavas of the ETZ, one path for the MORB lavas and another for the BABB lavas. The first step calculated for the MORB lavas was from group 32A to group 32B which required 5.9% crystallization of olivine and plagioclase in the proportion of about 1:2. The next step, group 32B to group 27, required 14.6% crystallization of olivine, plagioclase and clinopyroxene in the approximate proportions of 1:5:4. These first two steps represent a "good" sum of residuals (r^2) for fractionation. Step 27 to 31A required 22.9% crystallization of

Table 10a. Least Squares Fractional Crystallization Model for Manus MORB

Step 1
The parent lava is 32A

Coef	%	
0.020	0.334	32-2OL
0.039	0.666	32-2PLAG
0.941		32B is the daughter

	SiO2	TiO2	Al2O3	FeO	MnO	MgO	CaO	Na2O	K2O	P2O5
32B	50.52	1.08	14.58	10.79	0.18	7.76	12.62	2.26	0.05	0.16
32A										
OBS	50.55	1.00	14.93	10.42	0.14	8.16	12.37	2.22	0.04	0.17
CALC	50.25	1.01	15.00	10.47	0.17	8.19	12.49	2.21	0.05	0.15
DIF	0.12	-0.01	-0.03	-0.05	-0.03	-0.03	-0.12	0.00	-0.01	0.02

Sum of squares of residuals= 0.034

Step 2
The parent lava is 32B

Coef	%	
0.007	0.081	32-1OL
0.044	0.487	32-1PLAG
0.039	0.432	32-2CPX
0.908		27 is the daughter

	SiO2	TiO2	Al2O3	FeO	MnO	MgO	CaO	Na2O	K2O	P2O5
27	51.14	1.17	14.22	11.40	0.20	7.39	12.14	2.13	0.04	0.16
32B										
OBS	50.52	1.08	14.58	10.79	0.18	7.76	12.62	2.26	0.05	0.16
CALC	50.87	1.08	14.53	10.72	0.19	7.73	12.52	2.04	0.04	0.15
DIF	-0.14	0.00	0.03	0.07	-0.01	0.03	0.10	0.22	0.01	0.01

Sum of squares of residuals= 0.088

Step 3
The parent lava is 27

Coef	%	
0.008	0.074	27-5OL
0.038	0.366	27-5PLAG
0.058	0.561	27-5CPX
0.903		31A is the daughter

	SiO2	TiO2	Al2O3	FeO	MnO	MgO	CaO	Na2O	K2O	P2O5
31A	50.62	1.66	14.12	12.00	0.23	6.75	11.59	2.70	0.12	0.19
27										
OBS	51.14	1.17	14.22	11.40	0.20	7.39	12.14	2.13	0.04	0.16
CALC	50.81	1.53	14.26	11.36	0.22	7.45	12.22	2.53	0.11	0.17
DIF	0.13	-0.36	-0.02	0.05	-0.02	-0.06	-0.08	-0.40	-0.07	-0.01

Sum of squares of residuals= 0.321

Other steps:

The parent lava is 27

Coef	%	
0.011	-1.246	27-5OL
0.005	-0.569	27-5PLAG
-0.025	2.815	27-5CPX
		33B is the daughter

	SiO2	TiO2	Al2O3	FeO	MnO	MgO	CaO	Na2O	K2O	P2O5
33B	51.01	1.08	14.09	11.36	0.18	7.30	12.53	2.28	0.02	0.15
27										
OBS	51.14	1.17	14.22	11.40	0.20	7.39	12.14	2.13	0.04	0.16
CALC	50.81	1.08	14.27	11.48	0.18	7.41	12.24	2.31	0.02	0.15
DIF	0.13	0.10	-0.03	-0.07	0.03	-0.02	-0.10	-0.17	0.02	0.01

Sum of squares of residuals= 0.073
WARNING--MESSY MIXTURE OF ASSIMILATION AND FRACTIONATION

The parent lava is 32B

Coef	%	
0.013	0.296	32-1OL
0.031	0.704	32-1PLAG
0.957		26 is the daughter

	SiO2	TiO2	Al2O3	FeO	MnO	MgO	CaO	Na2O	K2O	P2O5
26	51.42	1.05	14.31	10.97	0.20	7.43	12.29	2.11	0.05	0.16
32B										
OBS	50.52	1.08	14.58	10.79	0.18	7.76	12.62	2.26	0.05	0.16
CALC	51.18	1.00	14.72	10.72	0.19	7.69	12.27	2.08	0.05	0.15
DIF	-0.27	0.07	-0.07	0.06	-0.01	0.07	0.35	0.18	0.00	0.01

Sum of squares of residuals= 0.244

Table 10b. Least Squares Fractional Crystallization Model for Manus BABB

Step 1
The parent lava is 31C

Coef	%	
0.009	0.038	31-SOL
0.085	0.353	31-SPLAG
0.147	0.609	31-SCPX
0.763		29B is the daughter

	SiO2	TiO2	Al2O3	FeO	MnO	MgO	CaO	Na2O	K2O	P2O5
29B	52.98	0.79	16.26	7.97	0.13	7.01	12.28	2.31	0.13	0.13
31C										
OBS	51.74	0.41	16.19	7.27	0.09	8.49	14.07	1.52	0.08	0.13
CALC	52.39	0.62	16.03	6.82	0.12	8.50	13.88	1.88	0.10	0.10
DIF	-0.26	-0.21	0.08	0.45	-0.03	-0.01	0.19	-0.36	-0.02	0.03

Sum of squares of residuals= 0.490

Step 2
The parent lava is 29B

Coef	%	
0.015	0.041	29-SOL
0.193	0.532	29-SPLAG
0.155	0.427	29-SCPX
0.637		30A is the daughter

	SiO2	TiO2	Al2O3	FeO	MnO	MgO	CaO	Na2O	K2O	P2O5
30A	54.17	1.14	15.20	10.99	0.20	5.28	9.66	3.02	0.17	0.16
29B										
OBS	52.98	0.79	16.26	7.97	0.13	7.01	12.28	2.31	0.13	0.13
CALC	52.72	0.76	16.32	8.06	0.14	7.02	12.35	2.42	0.12	0.10
DIF	0.10	0.02	-0.03	-0.09	0.00	-0.01	-0.08	-0.10	0.01	0.03

Sum of squares of residuals= 0.037

Step 3
The parent lava is 30A

Coef	%	
-0.007	-0.041	30-2OL
0.082	0.462	30-2PLAG
0.103	0.580	30-2CPX
0.821		33C is the daughter

	SiO2	TiO2	Al2O3	FeO	MnO	MgO	CaO	Na2O	K2O	P2O5
33C	53.96	1.40	14.97	12.63	0.20	4.20	8.97	3.24	0.22	0.20
30A										
OBS	54.17	1.14	15.20	10.99	0.20	5.28	9.66	3.02	0.17	0.16
CALC	53.35	1.19	15.30	11.34	0.19	5.22	10.01	2.83	0.18	0.17
DIF	0.33	-0.05	-0.05	-0.35	0.01	0.06	-0.35	0.19	-0.01	0.00

Sum of squares of residuals= 0.392
WARNING--MESSY MIXTURE OF ASSIMILATION AND FRACTIONATION

Step 4
The parent lava is 33C

Coef	%	
0.007	0.069	33-2OL
0.072	0.692	33-2PLAG
0.025	0.239	33-2CPX
0.896		30C is the daughter

	SiO2	TiO2	Al2O3	FeO	MnO	MgO	CaO	Na2O	K2O	P2O5
30A	55.18	1.53	13.92	13.24	0.23	3.97	8.21	3.32	0.22	0.17
33C										
OBS	53.96	1.40	14.97	12.63	0.20	4.20	8.97	3.24	0.22	0.20
CALC	54.53	1.39	14.86	12.41	0.22	4.26	8.76	3.18	0.21	0.16
DIF	-0.23	0.01	0.06	0.22	-0.01	-0.05	0.21	0.06	0.02	0.05

Sum of squares of residuals= 0.157

Other steps:

The parent lava is 33C

Coef	%	
0.003	0.049	33-2OL
0.030	0.479	33-2PLAG
0.029	0.472	33-2CPX
0.937		33A is the daughter

	SiO2	TiO2	Al2O3	FeO	MnO	MgO	CaO	Na2O	K2O	P2O5
33A	54.14	1.41	14.89	13.06	0.28	3.78	8.72	3.26	0.25	0.20
33C										
OBS	53.96	1.40	14.97	12.63	0.20	4.20	8.97	3.24	0.22	0.20
CALC	53.83	1.34	15.03	12.7	0.27	4.17	9.02	3.14	0.24	0.19
DIF	0.05	0.06	-0.03	-0.07	-0.07	0.03	-0.05	0.10	-0.02	0.01

Sum of squares of residuals= 0.030

The parent lava is 30A

Coef	%	
-0.007	-0.035	30-2OL
0.109	0.567	30-2PLAG
0.09	0.468	30-2CPX
0.803		30B is the daughter

	SiO2	TiO2	Al2O3	FeO	MnO	MgO	CaO	Na2O	K2O	P2O5
30B	53.94	1.43	14.23	13.18	0.19	4.56	8.98	3.12	0.16	0.15
30A										
OBS	54.17	1.14	15.20	10.99	0.20	5.28	9.66	3.02	0.17	0.16
CALC	53.05	1.19	15.35	11.45	0.18	5.20	10.13	2.72	0.13	0.12
DIF	0.44	-0.05	-0.08	-0.46	0.02	0.08	-0.47	0.29	0.04	0.04

Sum of squares of residuals= 0.734
WARNING--MESSY MIXTURE OF ASSIMILATION AND FRACTIONATION

The parent lava is 30A

Coef	%	
0.000	-0.002	30-2OL
0.136	0.548	30-2PLAG
0.113	0.454	30-2CPX
0.749		30C is the daughter

	SiO2	TiO2	Al2O3	FeO	MnO	MgO	CaO	Na2O	K2O	P2O5
30C	55.18	1.53	13.92	13.24	0.23	3.97	8.21	3.32	0.22	0.17
30A										
OBS	54.17	1.14	15.2	10.99	0.20	5.28	9.66	3.02	0.17	0.16
CALC	53.83	1.20	15.28	11.18	0.21	5.23	9.80	2.76	0.17	0.13
DIF	0.13	-0.05	-0.04	-0.19	0.00	0.05	-0.14	0.26	0.00	0.03

Sum of squares of residuals= 0.150
WARNING--MESSY MIXTURE OF ASSIMILATION AND FRACTIONATION

olivine, plagioclase and clinopyroxene in proportions of 1:4:6. This last step attempted did not give a "good" sum of residuals for fractionation. The concentrations of TiO_2 and Na_2O were too low in the parent lava, implying a clinopyroxene composition not sufficiently evolved for this lava. Other steps that may be possible are summarized in Table 10a.

The BABB lavas can be characterized by one major path. Step one, from group 31C to group 29B, can be modeled by 23.7% crystallization of olivine, plagioclase and clinopyroxene in approximate proportions 1:9:15. However, this first step did not yield a "good" sum of residuals for fractionation. TiO_2 and Na_2O concentrations were too low, and FeO and CaO concentrations were too high in the parent lava. The next step, from group 29B to group 30A, requires 51.4% crystallization of olivine, plagioclase and clinopyroxene in the proportions of about 2:19:16. This step represents a "good" sum of residuals ($r^2 \leq 0.15$) for fractionation. A third step from group 30A to any of the following groups, 30B, 30C or 33C, requires assimilation of olivine into the magma. This does not seem appropriate for this suite of lavas based on petrography and mineralogy of the samples. However, the "best fit" step is from group 30A to group 33C. FeO and CaO concentrations are too low, and Na_2O is too high in the parent lava. A fourth step from group 33C to group 30C and from group 33C to group 33A was attempted. The step from group 33C to group 30C required crystallization of olivine, plagioclase and clinopyroxene (1:7:3). The crystallization of olivine, plagioclase and clinopyroxene were required for the step from group 33C to group 33A in the proportion of about 1:5:5. These last two steps yielded "good" residuals ($r^2 < 0.15$) for fractionation.

The observed proportions of the crystallizing phases are similar to the calculated proportions in each fractionation step, especially in the MORB lavas. However, noncorrespondence between the observed and calculated mineral

proportions does not warrant major concern for fractionation modeling. Crystal settling and crystal plating in magma chambers or conduits are mechanisms that may be in effect below the ETZ, causing differences between the observed and calculated mineral proportions. Sum of squares of residuals (Table 10) represents the "best fit" solution for fractionation. In the ETZ MORB and BABB fractionation models the sum of squares of residuals tend to be high (> 0.1); however, fractionation paths chosen were restricted only to the ETZ data available and represented the most reasonable paths (Fig.7).

The models have been modified to represent crystal fractionation from primary magmas (Mg # $\simeq$ 72) as shown in Figure 14, assuming linear variation of Mg # with percent fractionation throughout the observed compositional range; this assumption is clearly an oversimplification. Nevertheless, using this assumption requires approximately 34 % fractionation to get from a MORB primary magma (Mg # = 72) to the most primitive MORB observed. This result contrasts with the approximately 5 % fractionation from a hypothetical BABB primary magma (Mg # = 72) to the most primitive BABB observed. Whether or not these estimations are quantitatively accurate, Figure 15 indicates that, relative to BABB, ETZ MORB undergo extensive shallow-level fractionation.

The effects of magma mixing may be identified by textural, mineralogical, and chemical evidence of the lavas. For the most part, minerals are in equilibrium with their host lavas; that is, the chemistry of the mineral phases that occur in these lavas are within the compositional range that can exist stably with its basaltic melt. Element-oxide diagrams (Figs.7, 9) display only fractionation trends within each of the lava suites; no mixing "lines" are apparent.

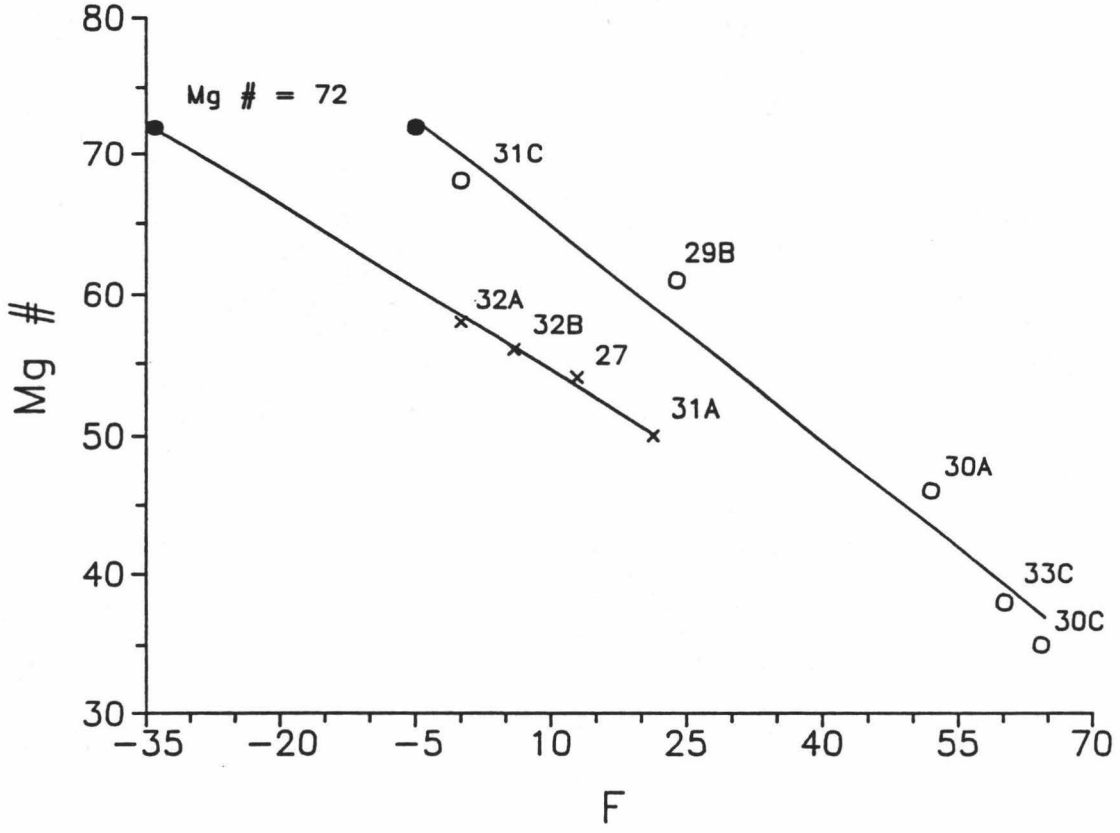

Figure 14. Mg # versus percent fractionation (F) for the Extensional Transform Zone lavas. Fractionation of the MORB and BABB suite is projected back to Mg # of 72, a value appropriate to primary magmas in equilibrium with mantle olivine.

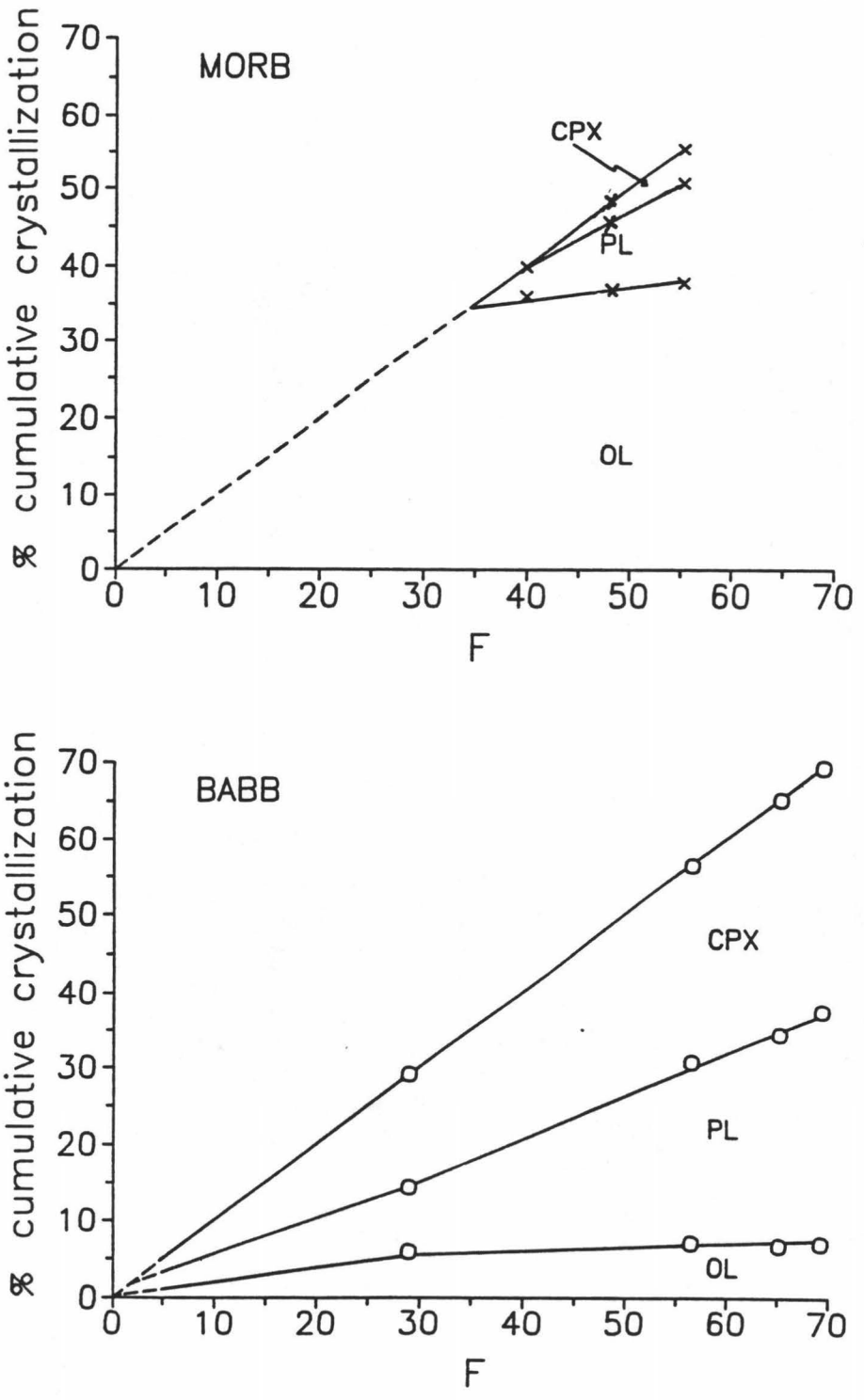

Figure 15. Diagramatic representation of the fractionation sequence in Extensional Transform Zone lavas based on least squares solutions presented in Table 10. Phase boundaries were drawn by eye to conform to the data points. Dashed lines are best guessed boundaries from the existing data.

Fractionation Conditions

Use of the projections in diopside-plagioclase-olivine-quartz (di-pl-ol-qtz) can help in understanding melting and crystallization behavior of basalt systems. These "end members" constitute major minerals involved in tholeiite petrogenesis and allow ready comparison with experimental studies. The use of the Grove projection (modified from Walker et al., 1979) allows recognition of fractionation and mixing trends between silica-saturated liquids at different stages of evolution. Projection of the averaged Manus MORB and BABB glass data from plagioclase onto the di-ol-qtz plane of the di-ol-pl-qtz tetrahedron (Fig.16a, b) reveal that the glasses plot near the olivine, plagioclase and clinopyroxene cotectic (phase boundary; equilibrium typically with two solid phases and one liquid phase) for 1 atm (Grove et al., 1982), even though some MORB do not contain clinopyroxene. The trend of the BABB lavas is slightly oblique to the 1 atm anhydrous cotectic for MORB in the ol-di-qtz pseudoternary diagram (Fig.16b). The effect of water on the position of the 1 atm olivine-plagioclase-clinopyroxene cotectic is not well understood, although Kushiro (1972) and Grove and Baker (1984) imply that the field of olivine expands at the expense of pyroxene. The BABB olivine-plagioclase-clinopyroxene cotectic seems to rotate slightly clockwise (Fig.16b) in relation to the anhydrous 1 atm cotectic, suggesting the expansion of olivine at the expense of pyroxene due to their higher H_2O content. In the ol-pl-qtz pseudoternary diagram (Fig.16c, d), experimental studies have shown that even with the addition of a small amount of water to the melts, the liquidus fields of olivine and pyroxene expand at the expense of plagioclase (Yoder and Tilley, 1962). Relative to MORB, the BABB glasses show a slight displacement of the olivine-plagioclase cotectic on the ol-pl-qtz pseudoternary toward plagioclase (Fig. 16d), also consistent with their higher H_2O content. Higher

Figure 16. Pseudoternary projections of Manus MORB, BABB and X-BABB. Projection from plagioclase onto the clinopyroxene - olivine - SiO_2 plane of the plagioclase - clinopyroxene - olivine - SiO_2 tetrahedron for (a) MORB and (b) BABB and X-BABB. Projection from clinopyroxene onto the plagioclase - olivine - SiO_2 plane for (c) MORB and (d) BABB and X-BABB (from Walker et al., 1979; Grove et al., 1982). The solid curve refers to anhydrous experimental results at 1 atm (Grove et al., 1982) and the dashed curve refers to experimental results at 2 kbar with 2% H_2O (Baker and Eggler, 1983). Experimental phase boundaries ("Y") at 10, 15 and 20 kbar (Stolper, 1980). Symbols are: (+) MORB, (o) BABB, (*) X-BABB.

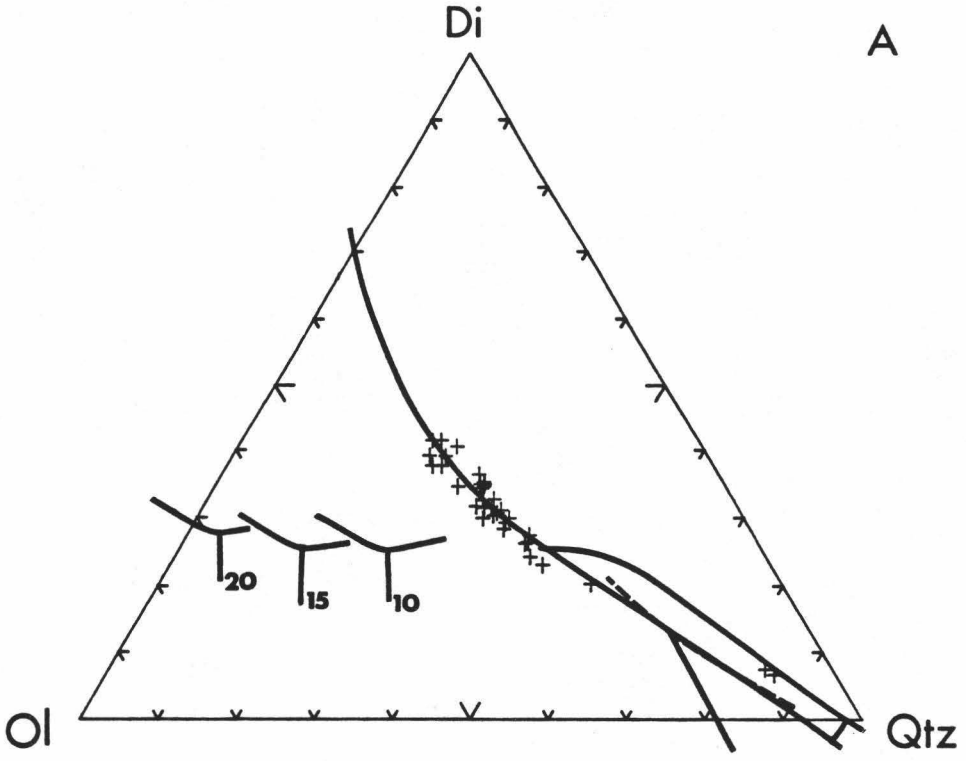
Di
A
20
15
10
Ol
Qtz

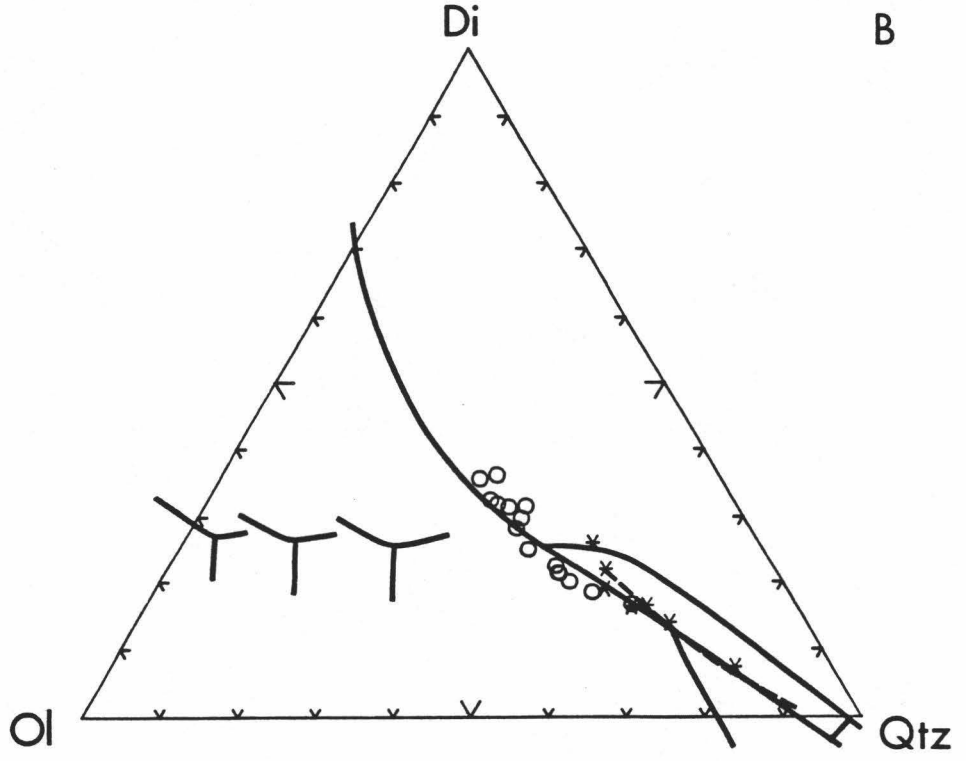
Di
B
Ol
Qtz

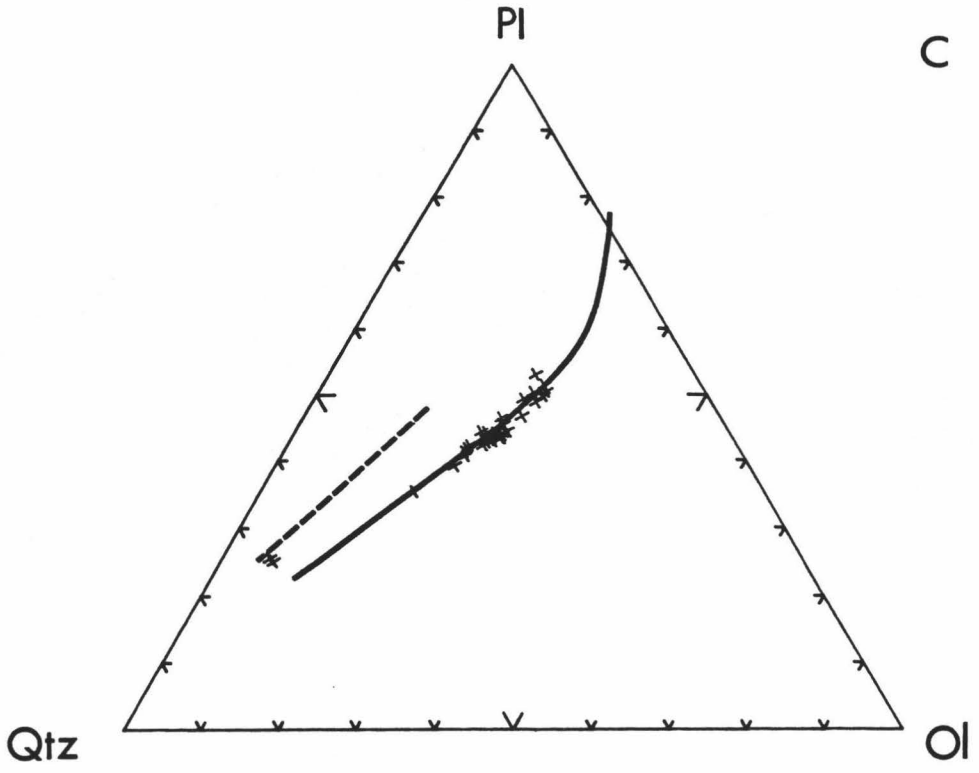
Pl
C
Qtz
Ol

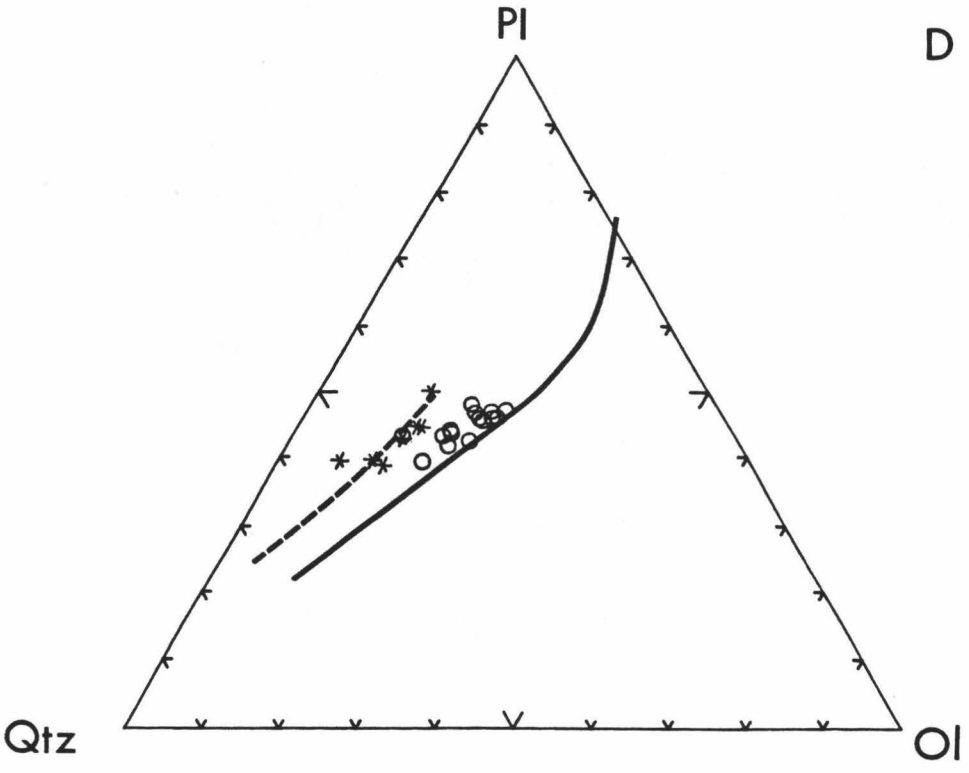
Pl
D
Qtz
Ol

H_2O content can also be shown by the steeper Na_2O trend (Fig.7) for BABB. X-BABB glasses plot near the clinopyroxene-pigeonite cotectic (Fig.16b), and the displacement of the olivine-plagioclase cotectic for this suite (Fig.16d) is consistent with even higher H_2O contents. The trend of X-BABB is consistent with hydrous fractionation at 2 kbar (Fig.16b, d).

In contrast to the MORB lava suite, the BABB lava suite contains clinopyroxene at high Mg # (68). The high Mg # indicates that the most primitive BABB lava experienced little fractionation and that it is close in composition to its primary magma (unmodified derivative of mantle melting) (Fig.14, 15). The primary magma must have been close to its cotectic to have clinopyroxene crystallizing in the glass with Mg # = 68. BABB compositional variations are consistent with hydrous fractionation at or near 1 atm (Fig.16). Therefore, the high pressure fractionation explanation for the early appearance of clinopyroxene is not supported. Alternatively, the most primitive BABB lava may have segregated from a residual mantle at shallow depths. High-pressure fractionation may also be distinguished by a high concentration of Al in clinopyroxenes. Concentration of Al in pyroxenes from MORB and BABB are similar (Table 9), thus, supporting shallow-level fractionation for both suites.

MELTING CONDITIONS

Comparison to experimental phase boundaries of Stolper (1980) at 10, 15 and 20 kbar, and univariant melting curves of Takahashi and Kushiro (1983) at 8, 10 and 15 kbar suggests a primary MORB magma must be generated at least at 10 kbar pressure (Fig.16a). The most primitive MORB have a low Mg # (58) indicating a

more extensive fractionation history than the most primitive BABB (Fig.14). The increase in TiO_2 with decreasing concentration of MgO also indicates that the MORB "cluster" represents a liquid line of descent, from primitive (magmas closest to primary) samples to more fractionated samples (Stolper, 1980). The effects of water must be considered in order to compare BABB to any experimental phase boundaries or univariant melting curves. Qualitatively, under hydrous conditions, the phase boundaries/univariant melting curves will shift toward silica (Kushiro, 1969), but not much at 1 atm. Therefore, comparison to the same experimental phase boundaries as with MORB will yield a valid approximation of melting pressure. The projection of the BABB data plot near the cotectic for 10 kbar. Therefore, a BABB primary magma must be generated at pressures between 5 to 10 kbar (Fig.16b).

Iron and magnesium are especially useful to document variations in the mantle source and melt formation conditions because they act as "intermediate elements" (Hanson and Langmuir, 1978) between trace elements and other major elements. Iron and magnesium are in solid solution and do not fully occupy one site in any mineral in the system (like trace elements), but are abundant enough to be stoichiometrically important (like most major elements). Therefore, Fe and Mg should reflect melt formation conditions. Their abundances will be primarily a function of pressure at which melting begins and the extents of melting (Langmuir and Hanson, 1980). Source compositional variations are less important because Fe and Mg will tend to be buffered by ferromagnesian phases in the mantle during melting.

Iron contents (expressed as mol %) of magmas is little affected by olivine fractionation (Langmuir and Hanson, 1980). Olivine fractionation paths are nearly vertical on the molar FeO-MgO diagram (Fig.17). Therefore, the FeO contents of the melts saturated only with olivine should reflect FeO contents of the primary

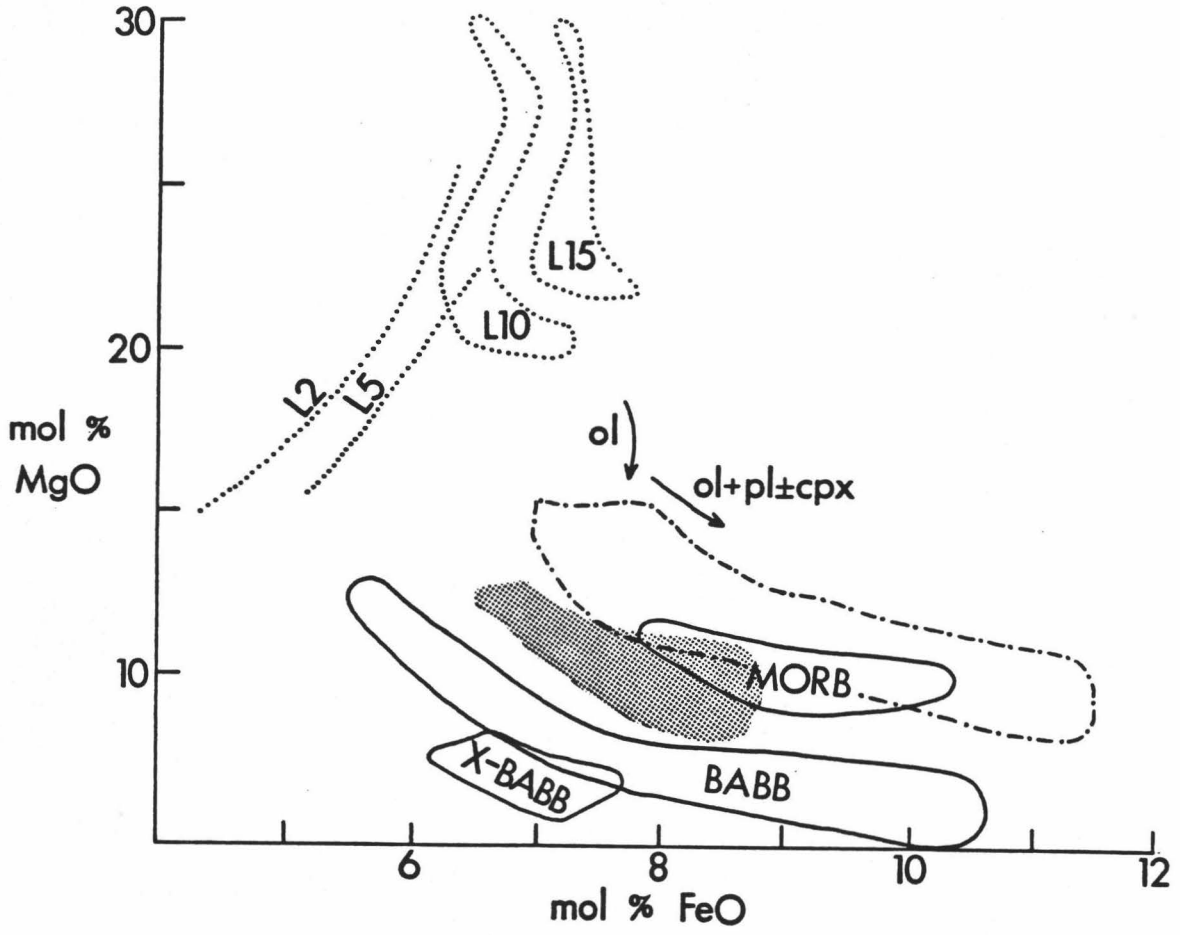

Figure 17. Mole percent MgO versus mole percent FeO showing the data fields of Manus MORB, BABB and X-BABB (solid lines) and the data fields of the Mariana Trough (stipple) and N-MORB (dash-dot line). In addition, data fields from Jaques and Green (1980) for melting of Tinaquillo lherzolite at 2, 5, 10 and 15 kbar (L2, L5, L10, L15) are shown (After Sinton and Fryer, 1987).

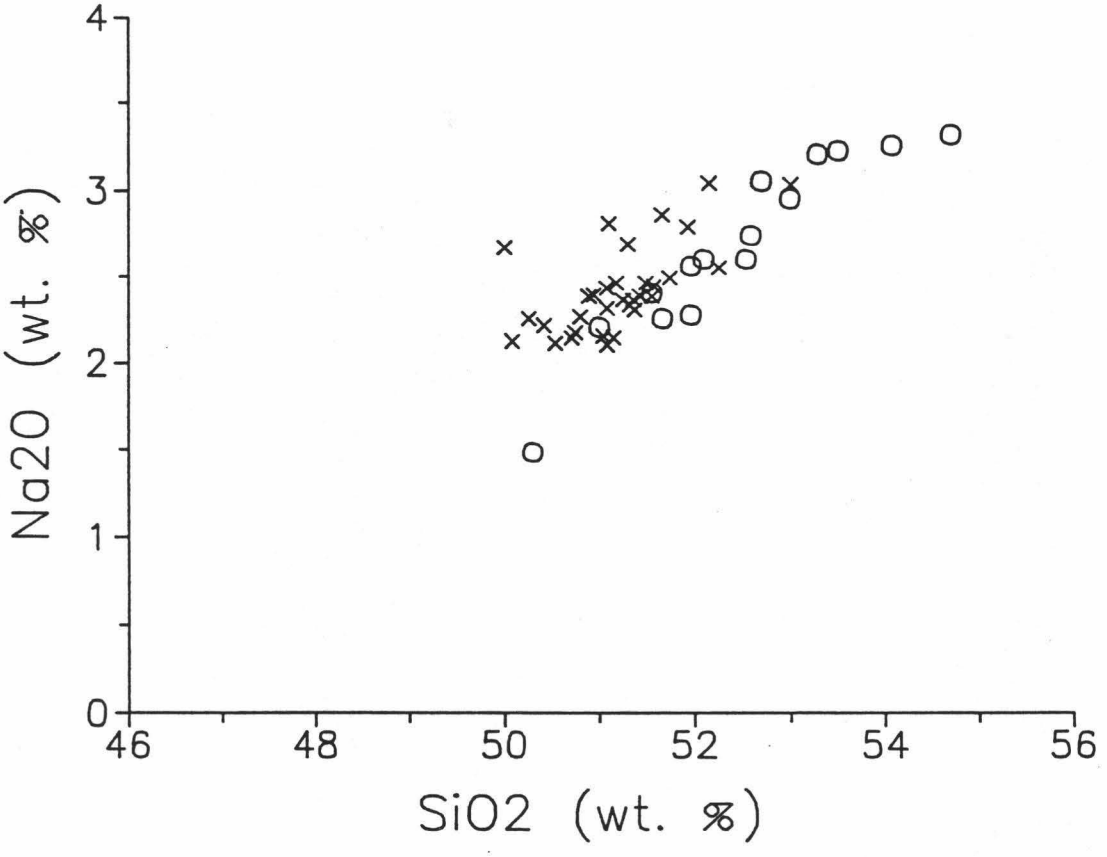

Figure 18. Na_2O versus SiO_2 for Manus MORB and BABB glass data. Manus BABB is slightly offset to higher SiO_2. Symbols are the same as in Figure 7.

magma. However, none of the ETZ and Manus Spreading Center (MSC) lavas are saturated only with olivine. Once plagioclase joins in as a fractionating phase, liquid lines of descent are low angle (Fig.17). Magnesium contents of magmas are very sensitive to olivine fractionation, therefore, it provides little information about the MgO content of primary melts. However, approximately 10% higher degree of melting, 7 kbar lower pressure (or 70K lower temperature of melting), and an increase of 1% in the forsterite content of olivine (Langmuir and Hanson, 1980) will produce the observed 2 mol % lower Fe displacement of primary melt composition (Fig.17).

The Manus Basin data indicate that the BABB lavas were generated at lower pressures (and possibly higher extents of melting than the Manus MORB lavas) due to its offset to lower Fe at a given Mg relative to Manus MORB lavas (Fig.17). Comparison to experimental data fields from Jaques and Green (1980) for melting of Tinaquillo lherzolite at 2, 5, 10 and 15 kbar results in a primary BABB magma that could be generated near 5 kbar pressure (Fig.17). This is even lower than the field for Mariana Trough BABB lavas. A primary Manus MORB magma could be generated at 10-15 kbar pressure.

SiO_2 variation depends strongly on the pressure of melting, as well as the extent of melting. Melts produced at lower pressures have higher SiO_2 contents (Klein and Langmuir, 1987). For a given Na_2O content, the BABB data is slightly offset to higher SiO_2 compared to the Manus MORB data (Fig.18), suggestive of melting at lower mean pressures for Manus BABB (Klein and Langmuir, 1987).

SOURCE COMPOSITION

The BABB differ from MORB especially in their concentrations of FeO^*, K_2O and TiO_2 (Fig.7). These differences in major elements can be accounted for by fractionation as well as depth of melting. BABB also differ from MORB by their enrichments in large ion lithophile elements (*e.g.* Rb, Ba, Sr) and in light rare earth elements (LREE). These differences, however, can not be accounted for by fractionation or depths of melting. The source for BABB can be considered to be MORB-like, but modified by metasomatism (Sinton and Fryer, 1987). Most workers on arc and back-arc magmatism look to the subducted lithosphere as the source for the metasomatizing agent (Tatsumi et al., 1986). Metasomatism of back-arc magmas may be indirectly related to the subducted lithosphere through mantle convection. Mantle-derived peridotites containing hydrous veins composed of mica and/or amphibole, which are rich in large ion lithophile elements (LILEs), implies ... "that the migration of these elements is associated with an aqueous fluid phase (such a fluid is capable of dissolving certain elements to some extent) from the deeper part of the Earth" (Tatsumi et al., 1986). At these deeper levels in the Earth, the amount of water released is likely to be small, therefore, causing only a small number of diapirs to rise; thus, the occurrence of BABB would not be widespread but interdispersed with MORB.

The observed FeO / MgO relations in Manus BABB and MORB indicates that their sources are similar. Most models for the generation of normal MORB (N-MORB) from mid-ocean ridges use a pyrolite composition (Jaques and Green, 1980) as the MORB source; however, Manus MORB is far more depleted than N-MORB (see "III. Results: Implications for magma types in the Manus Basin"), thus the more

depleted Tinaquillo lherzolite (Mg # = 90.3) is probably a more suitable source for Manus MORB. The Tinaquillo lherzolite is similar to the Dick and Fisher (1984) more depleted alpine-type peridotite, which they use for modeling magma genesis of island-arc and back-arc basin lavas. High degrees of melting of this alpine-type peridotite for the petrogenesis of back-arc basin lavas requires water. Water reduces the temperature of melting, therefore, making available more heat for fusion of the peridotite during ascent, potentially resulting in higher degrees of melting (Dick and Fisher, 1984).

The observed rare earth element (REE) patterns of Manus MORB and BABB lavas show that the BABB lavas are enriched in LREE as well as Ba relative to HREE (Fig.10). The enrichment sequence of the LREE from MORB to X-BABB may imply some sort of systematic enrichment of the LREE. This indicates that the observed enrichment is related to the source and that the observed pattern could not be a result of fractionation (which tends to elevate the overall pattern). Alteration effects are negligible owing to the exclusion of all alteration surfaces from the rock chips prior to crushing and analysis. The relative concentration of selected trace elements were used in the Manus MORB and BABB at comparable levels of fractionation. A value of 60 is used for Mg # because it is a close to the Manus MORB and BABB data, therefore, it won't introduce large errors from extrapolation. The slope of each group trend was estimated (taking into account each elements' incompatibility in fractionating phases) and the concentration of the element for each "group" at the intersection of Mg # = 60 was taken. An enrichment factor (E.F.) was calculated by taking the concentration of an element in BABB and dividing it by the concentration in MORB, at Mg # = 60.

$$\text{E.F.} = \frac{\text{concentration of element in BABB at Mg \# = 60}}{\text{concentration of element in MORB at Mg \# = 60}}$$

Mg # is used in the E.F. calculation because it puts everything at the same level of fractionation rather than MgO (which is sensitive to depths of melting). E.F.'s were calculated for Y, Sm, Yb, Na, Ti, V, Ba, Zr, Sr, K, Rb, La and Ce. The BABB group was subdivided into six subsets: one set representing the "initial" enrichment, the second set representing a typical BABB enrichment and the remaining four sets representing the extremely-enriched BABB (the relationship of X-BABB to one another is not well constrained). From the six subsets, thirteen E.F.'s were calculated. They indicate the sequence of element enrichment of the BABB group: Rb > Ba > K > La > Sr > Ti > V > Zr > Y > Yb. Enrichment of the mantle source for BABB must have occurred by some metasomatic event(s) prior to melting. The order of element enrichment bears important evidence whether the metasomatizing agent was an aqueous fluid or a partial melt. In aqueous fluids, the mobility of elements is essentially proportional to ionic radius, with Rb being significantly more mobile than Ba (Tatsumi et al., 1986). Partial melting, on the other hand, inversely correlates the degree of enrichment with bulk solid / melt distribution coefficients; melting enriches Ba more than Rb (Pearce, 1983). It is most likely that the metasomatizing agent for the Manus BABB suite was an aqueous fluid because Rb, which has a larger ionic radius than Ba, is prefentially enriched (Fig.19a).

Crossing of patterns between MORB, BABB and X-BABB occur at Sm (Fig.19a). Within the X-BABB suite, the patterns tend to be subparallel. X-BABB have extreme BABB elemental enrichments and depletions (not previously documented), therefore, if it can be taken as an "end member" source, mixing of X-BABB into MORB sources could give rise to the formation of BABB. The proportion of the X-BABB component to produce BABB can be calculated by:

$$(\text{BABB} - \text{MORB})_i \,/\, (\text{X-BABB} - \text{MORB})_i$$

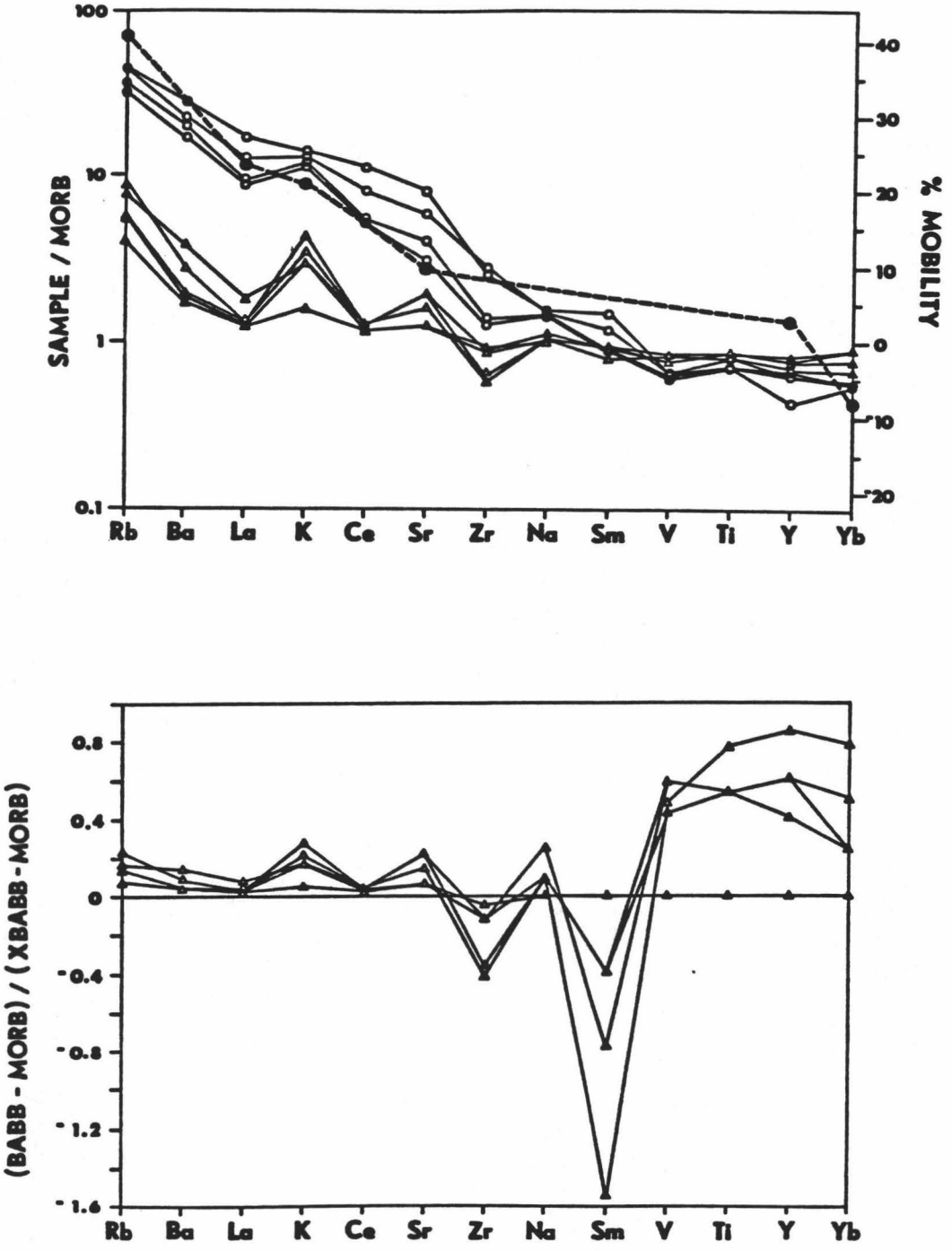

Figure 19. (a) Elemental concentration of Extensional Transform Zone and Manus Spreading Center lavas normalized to Manus Basin MORB plotted against rank order of the element in the BABB source. Mobility of incompatible elements by a fluid phase in a washed serpentine (Tatsumi et al., 1986) is plotted over the BABB trends, shown by solid circles connected with a dashed line. (b) Proportional enrichment of BABB by an averaged X-BABB component plotted against rank order of the element. Symbols are: (o) X-BABB, and (Δ) BABB.

where, i = element. From Figure 19b, the amount of X-BABB component in BABB is about 1.8 % for the elements, Rb to Na; and about 7.3 % for the elements, V to Yb. Zr and Sm depletion in BABB can't be accounted for by mixing of X-BABB into MORB (Figs.9, 19). The relationship of element partitioning into BABB is more complicated than a simple proportional mix of X-BABB into MORB, as shown in Figure 19b. Alternatively, hydrous veined peridotites composed of mica and/or amphibole may be the source of the aqueous fluid phase.

EXTENTS OF MELTING

Extents of melting for basaltic lavas can be constrained by the behavior of most major elements (Jaques and Green, 1980; Fujii and Scarfe, 1985). The concentration of Na_2O is highest at the smallest extents of melting and decreases as the extent of melting increases. Al_2O_3 is also highest at small extents of melting and decreases with larger extents of melting. At lower extents of melting, the concentration of CaO is low and increases steadily with higher extents of melting until clinopyroxene is exhausted as a residual mantle phase. Both FeO^* and MgO depend on pressure of melting as well as extent of melting. Their concentrations, especially FeO^*, increase with increasing pressure. Based on global chemistry/depth correlations, basalts from the shallowest mid-ocean ridge segments are produced by larger extents of melting deeper in the mantle (Klein and Langmuir, 1987). Such high degrees of melting might be expected in the hydrous BABB source region, due to hydrous solidus depression (Yoder and Tilley, 1962; Green, 1973; Mysen and Boettcher, 1975; Mysen and Kushiro, 1977; Wyllie, 1979). The concentration of

FeO^* (Fig.7) in BABB might indicate a higher degree of melting, as expected for hydrous melting. Na_2O concentrations in MORB and BABB aren't very different, but the offset to a slightly lower concentration in BABB at high MgO may also indicate high degrees of melting. The offset of CaO to a higher concentration also indicates a higher degree of melting for the BABB lavas. However, the slightly higher Al_2O_3 in the BABB lavas compared to the MORB lavas could be taken to indicate lower extents of melting for the BABB lavas. From experimental studies done by Fujii and Scarfe (1985) and others it is shown that with increasing extents of melting, the primary melts will become depleted in Al_2O_3. Melting and crystallization behavior of basalt systems interpreted from the ol-di-qtz pseudoternary (Fig.16) and the molar FeO-MgO diagram (Fig.17) suggests that the BABB suite is derived from a lower pressure (~5 kbar) than the MORB suite. This pressure is within the stability field of plagioclase peridotite; melt in this region would increase the concentration of Al_2O_3 of a melt at similar MgO contents compared to melt in the stability field of spinel peridotite.

Major element data allow some quantitative constraints to be placed on the extent of melting to produce BABB and MORB lavas. Na_2O, although not perfectly incompatible in the melt, places reasonable constraints on the extent of melting. Using the melting equation:

$$C_L = C_0 / F(1-D) \qquad (1)$$

where, C_L is the element in the magma, C_0 is the abundance in the source, F is the fraction of melt, and D is the bulk distribution coefficient (assuming D = 0), then the extent of melting is approximately 11% for BABB and 7% for MORB, assuming the Na_2O in the mantle source for both Manus MORB and BABB is about 0.18 (the value for Tinaquillo lherzolite). Using D_{Na} = 0.1 (Hofmann, 1988), the extents of melting for Manus MORB and BABB remain unchanged.

PRESSURE AND TEMPERATURE OF MELTING

The slope for a pyrolite solidus has been investigated by Green (1973). Assuming that the solidus for Tinaquillo lherzolite (presumed Manus MORB source) is not substantially different from the pyrolite solidus, then the lherzolite solidus should be the same as the pyrolite solidus. If erupted magma constitutes an average of pooled melts from the ascending mantle column (Klein and Langmuir, 1987), then pressures inferred from the molar FeO-MgO diagram (Fig.17) represent mean pressures of melting. Calculation of solidus intersection from Klein and Langmuir (1987):

$$P = P_o - 0.707 * (P_o - P_f) \quad (2)$$

$$F = 0.006 * (P_o - P_f) \quad (3)$$

where, P is the mean pressure of melting, P_o is the pressure of intersection of the solidus, P_f is the final pressure of melting, and F is the mean fraction of melting. Combining equations (2) and (3) eliminates P_f, giving:

$$F / 0.006 = P - P_o / -0.707 \quad (4)$$

Assuming P is 10 kbar (from Fig.17) and F is 7 % for the Manus MORB lavas, then the initial pressure of intersection of the solidus is about 18 kbar (Fig.20). At 18 kbar pressure, the temperature of the mantle is about 1350^{o}C; this temperature is slightly higher than that predicted by McKenzie and Bickle (1988) for normal-MORB. This discrepancy may be accounted for by one of two reasons. First, by

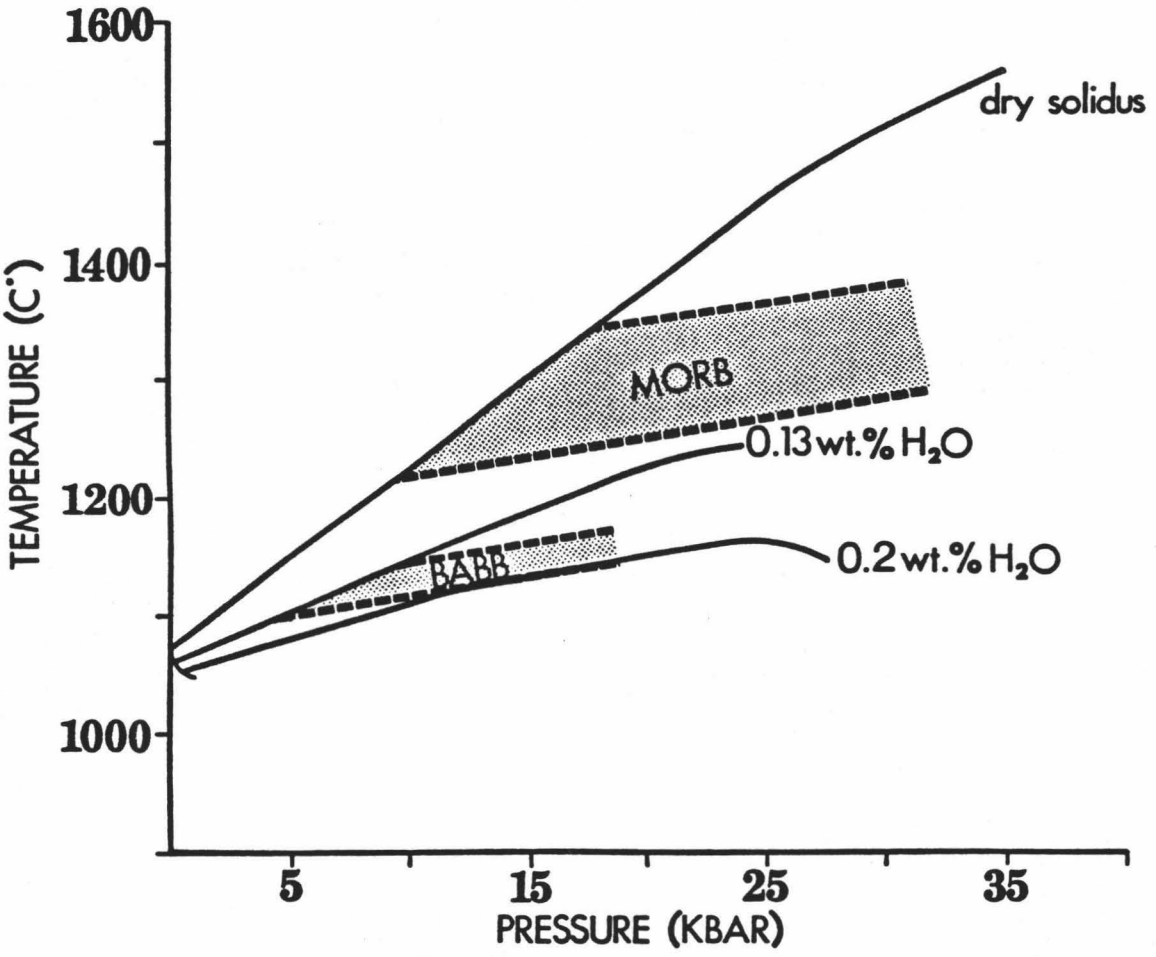

Figure 20. Solidus (temperature/depth) diagram. Estimated 0.13 wt. % H_2O solidus; dry solidus and 0.2 wt. % H_2O solidus from Green (1973). Stippled regions represent MORB and BABB diapir adiabats.

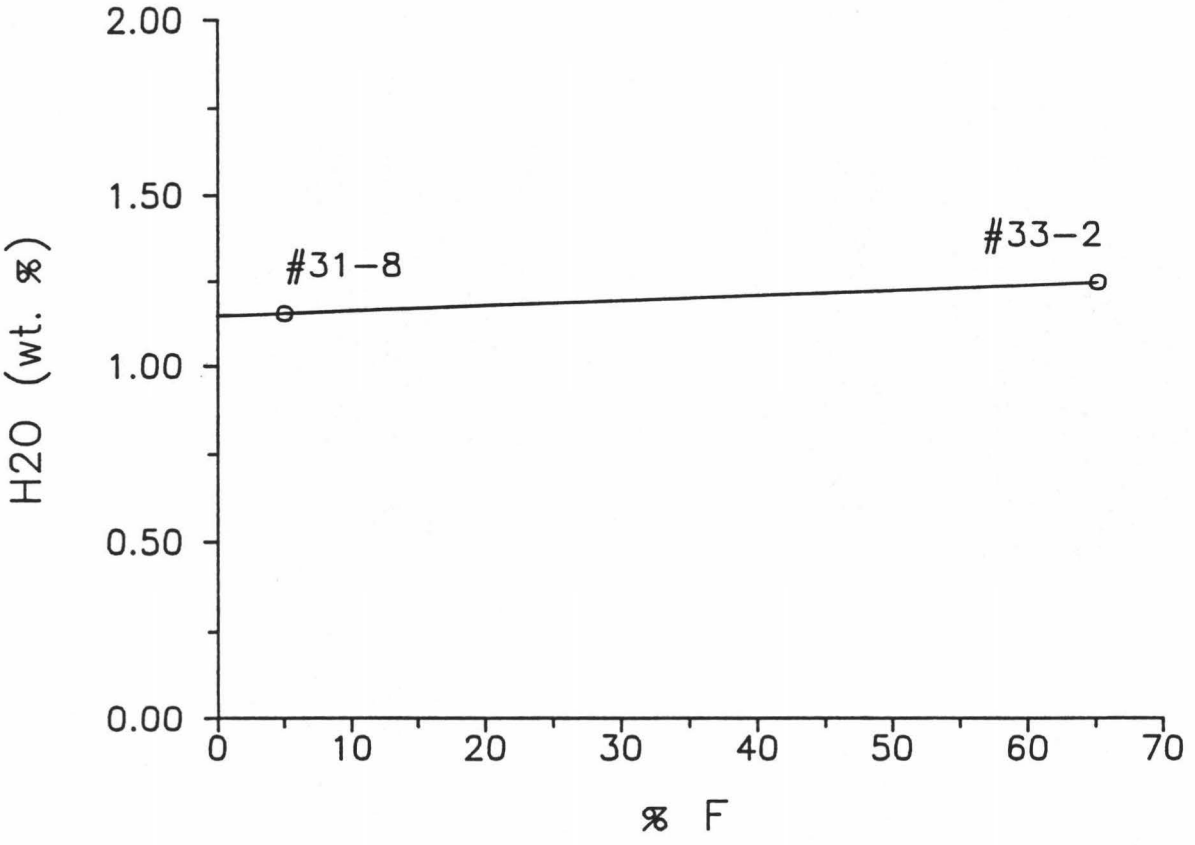

Figure 21. H_2O versus percent fractionation (F), using "corrected" fractionation in Figure 14.

eliminating McKenzie and Bickle's (1988) assumption that all melt produced is extracted and adiabatic melting continues to the surface; then qualitatively, their adiabatic decompression paths would be lowered and temperature-melt thickness curves will be flattened. This would yield a temperature closer to 1280^{o}C. Second, if P (10 kbar) for MORB is actually the mean pressure of solidus intersection (Langmuir and Hanson, 1980), then the average temperature for Manus MORB is about 1240^{o}C. According to McKenzie and Bickle (1988), this temperature is very close to their normal-MORB mantle temperature of 1280^{o}C, and therefore, should make crust about 7 km thick (which is normal). Either hypothesis would yield reasonable pressures and temperatures.

If the solidus for Tinaquillo lherzolite is not substantially different from the pyrolite solidus, then the effect of water on the lherzolite solidus should be the same as its effect on the pyrolite solidus. If BABB's formed by about 11% melting (see "extents of melting") and the amount of H_2O in the liquid is about 1.15 wt. % (Fig.21) and H_2O is perfectly incompatible during melting (D = 0), then the source for BABB would have contained about 0.13 wt. % H_2O before melting, using equation (1) (Fig.20). Calculation of pressure of solidus intersection from Klein and Langmuir (1987), however, assumes 1.2% melt/kbar of pressure of decompression for MORB; McKenzie and Bickle (1988) use 1.0% melt/kbar for MORB. An appropriate value for BABB must take into account water in the melting system; thus, changing the thermodynamics of melting in the ascending column. However, pressures of melting for BABB can be inferred by the molar FeO-MgO diagram (Fig.17); about 5 kbar pressure of melting is inferred for BABB magmas. BABB diapirs melt at lower pressures than MORB and reflect cooler adiabats than MORB diapirs (Fig.20).

V. CONCLUSIONS

The Manus Basin is composed of seven tectonic features of which four are associated with recent lava. These four features are: rift grabens (Southern Rifts), segmented ridges (East Manus Ridges), a spreading center (Manus Spreading Center) and an extensional transform (Extensional Transform Zone). Lavas in the Manus Basin represent three distinct types of magma. Island-arc associated lavas are restricted to the rifts and ridges closest to the New Britain Arc. Farther from the arc, MORB and BABB lava types are erupted from the Manus Spreading Center (MSC) and the Extensional Transform Zone (ETZ). Manus MORB lavas are similar to normal-MORB (N-MORB), but with slightly lower concentrations of incompatible elements, especially TiO_2, Al_2O_3, K_2O, P_2O_5, Rb, Sr, and Ba.

Manus BABB lavas are enriched in incompatible elements, especially Al_2O_3, K_2O, Rb, Sr, Ba, light rareearth elements (LREE) and H_2O, and depleted in FeO^* and TiO_2 compared to Manus MORB. An extremely enriched version of BABB (X-BABB) was recovered from the shalllowest portion of the MSC. X-BABB is distinguished from the lavas of the island-arc association by its moderate Ba/La and LREE enriched pattern (Fig.10), and from other incompatible element enriched back-arc basin lavas (e.g. some Fiji back-arc lavas) by its REE pattern and general depletion in heavy REE and HFS (high field strength) elements, suggestive of a distinctive source character.

Evidence for Transform Fault Effects in the lavas near the transform-ridge intersection is not apparent in the vicinity of the ETZ and MSC. Enrichments in TiO_2 and FeO^* at other intersections is not observed at the ETZ/MSC intersection. This lack in Transform Fault Effects is probably due to the extensional character of

the ETZ, which would create a hotter thermal regime compared to conventional transform faults/mid-ocean ridge intersections.

Lavas within the Manus MORB and BABB suites can be related by fractionation, with the MORB suite experiencing more extensive fractionation relative to the BABB suite. The early appearance of clinopyroxene in the BABB lavas coupled with its close proximity to a 1 atm cotectic (with water), may indicate shallow-level fractionation. X-BABBs follow a cotectic of 2 kbar with 2% H_2O.

The source composition for Manus MORB and BABB is more depleted than N-MORB, similar to Tinaquillo lherzolite rather than pyrolite, which is a typical source composition for N-MORB. The enrichment of LREE and Ba of the Manus BABB in relation to Manus MORB, and the relative amounts of elemental enrichment suggests an aqueous fluid as the BABB metasomatizing agent. Hydrous veins in mantle peridotites (which are rich in large ion lithophile elements) and its subsequent melting could cause the enrichment of these elements. Total volatile contents including H_2O, is greater in Manus BABB compared to Manus MORB. The effect of water lowers the temperature at which BABB magmas intersect the solidus, possibly producing higher extents of melting compared to MORB magmas. Major element data indicates slightly higher extents of melting for BABB than MORB. Quantitative constraints on the extent of melting, using Na_2O, place extent of melting at about 11% for BABB and 7% for MORB. Thus, the preferential shallow eruption depths of BABB compared to the large range of eruptive depths for MORB can possibly be explained by higher extents of melting of the BABB source. Assuming that the mean pressures of melting for Manus BABB and MORB can be inferred from the molar FeO-MgO diagram (Fig.17) and the pseudoternary plot (Fig.16), pressures are about 5 and 10 kbar, respectively. Calculated solidus intersection pressures from Klein and Langmuir (1987) indicate about 18 kbar

pressure for Manus MORB. At this pressure for Manus MORB, mantle temperature and crustal thickness is reasonable. Most workers on arc and back-arc magmatism look to the subducted slab as the source for the metasomatizing agent. In back-arc basins, where the angle of the subducted slab is steep (approximately 70^{o} in the Manus Basin), hydrous fluids must be transported by mantle convection (Toksov and Bird, 1977). Interaction between convected fluids and the mantle may produce mantle-derived peridotites containing hydrous veins. Thus, the migration of large ion lithophile elements in aqueous fluids can produce sources that would yield BABB magmas upon melting. If X-BABB can be taken as an "end member" source (or aqueous fluid source), then mixing of X-BABB into MORB sources may give rise to the formation of BABB, though the mechanics of source mixing is more complicated. Alternatively, melting of a hydrous-veined mantle peridotite composed of mica and/or amphibole could be the source for BABB.

LITERATURE CITED

Aggrey, K., 1989, *Mass spectrometric investigation of the volatile content of glasses from back-arc basins and abyssal seamounts near spreading centers*, Ph.D. Dissertation, University of Hawaii, Honolulu, 247p.

Baker, D.R., and D.H. Eggler, 1983, Fractionation paths of Atka (Aleutians) High-alumina basalts: constraints from phase relations, *J. Volc. Geotherm. Res.*, v.18, p.387-404.

Bender, J.F., C.H. Langmuir, and G.N. Hanson, 1984, Petrogenesis of basaltic glasses from the Tamayo region, East Pacific Rise, *J. Petrol.*, v.25, p.213-254.

Bender, J.F., F.N. Hodges, and A.E. Bence, 1978, Petrogenesis of basalts from the project FAMOUS area: experimental study from 0 to 15 kbar, *Earth and Planetary Science Letters*, v.41, p.277-302.

Both, R., K. Crook, B. Taylor, S. Brogan, B. Chappell, E. Frankel, L. Liu, J. Sinton, and D. Tiffin, 1986, Hydrothermal chimneys and associated fauna in the Manus Back-Arc Basin, Papua New Guinea, *EOS Trans. Amer. Geophys. Union*, v.67, p.489-490.

Boynton, W.V., 1984, Cosmochemistry of the rare earth elements: meteorite studies, in Henderson, P., ed., *Rare Earth Element Geochemistry*, Elsevier, Amsterdam, p.63-114.

Bryan, W.B., 1972, Mineralogical studies of submarine basalts, *Carnegie Inst. Yearbook*, v.71, p.396-403.

Bryan, W.B., L.W. Finger, and F. Chayes, 1969, Estimating proportions in petrographic mixing equations by least-squares approximation, *Science*, v.163, p.926-927.

Byerly, G.R., W.G. Melson, J.A. Nelen, and E. Jarosewich, 1977, Abyssal basaltic glasses as indicators of magma compositions, in Mason, B., ed., *Mineral Sciences Investigations*, Smithsonian Contributions to the Earth Sciences, v.9, p.22-30.

Carr, M., 1985, *IGPET*, Rutgers University, © Terra Softa.

Connelly, J.B., 1974, A structural interpretation of magnetometer and seismic profiler records in the Bismarck Sea, Melanesian Archipelago, *J. Geol. Soc. Aust.*, v.21, p.459-469.

Connelly, J.B., 1976, Tectonic development of the Bismarck Sea based on gravity and magnetic modelling, *Geophys. J. R. astr. Soc.*, v.46, p.23-40.

Cooper, P., and B. Taylor, 1987, Seismotectonics of New Guinea: a model for arc reversal following arc-continent collision, *Tectonics*, v.6, p.53-67.

Davies, H.L., and R.C. Price, 1987, Basalts from the Solomon and Bismarck Seas, *Geomarine Letters*, v.6, p.193-202.

Denham, D., 1969, Distribution of Earthquakes in the New Guinea-Solomon Islands Region, *J. Geophys. Res.*, v.74, p.4290-4299.

Dick, H.J.B., and R.L. Fisher, 1984, Mineralogic studies of the residues of mantle melting: abyssal and alpine-type peridotites, in *Kimberlites*, Elsevier, Amsterdam, v.2, p.295-308.

Falvey, D.A., and T. Pritchard, 1985, Preliminary paleomagnetic results from northern Papua New Guinea: evidence for large microplate rotations, *Trans. Circum-Pacific Council Energy Mineral Resources*, v.3, p.593-600.

Fryer, P., J.M. Sinton, and J.A. Philpotts, 1981, Basaltic glasses from the Mariana Trough, *Init. Rep. of Deep Sea Drilling Project*, v.60, p.601-609.

Fujii, T., and C.M. Scarfe, 1985, Composition of liquids coexisting with spinel lherzolite at 10 kbar and the genesis of MORB, *Contrib. Mineral. Petrol.*, v.90, p.18-28.

Gallo, D.G., and P.J. Fox, 1979, The influence of transform faults on the generation of oceanic lithosphere, *EOS Amer. Geophys. Union*, v.60, p.376.

Garcia, M.O., N.W.K. Liu, and D.W. Muenow, 1979, Volatiles in submarine volcanic rocks from the Mariana Island arc and trough, *Geochim. Cosmochim. Acta*, v. 43, p.305-312.

Gill, J.B., 1976, Composition and ages of Lau Basin and Ridge volcanic rocks: implications for evolution of inter-arc and remnant arc, *Geol. Soc. Amer. Bull.*, v.87, p.1384-1395.

Goles, G.G., 1977, Instrumental methods of neutron activation analysis, in Zussman, J., ed., *Physical Methods in Determinative Mineralogy*, 2nd edition, Acad. Press, London, U.K., p.343-370.

Green, D.H., 1973, Contrasted melting relations in a pyrolite upper mantle under mid-ocean ridge, stable crust and island arc environments, *Tectonophysics*, v.17, p.285-297.

Green, T.H., and A.E. Ringwood, 1968, Genesis of the calc-alkaline igneous rock suite, *Contrib. Mineral. Petrol.*, v.18, p.105-162.

Grove, T.L., and M.B. Baker, 1984, Phase equilibium controls on the tholeiitic versus calc-alkaline differentiation trends, *J. Geophys. Res.*, v.89, p.3253-3274.

Grove, T.L., D.C. Gerlach, and T.W. Sando, 1982, Origin of calc-alkaline series lavas at Medicine Lake Volcano by fractionation, assimilation and mixing, *Contrib. Mineral. Petrol.*, v.80, p.160-182.

Hanson, G.N., and C.H. Langmuir, 1978, Modelling of major elements in mantle-melt systems using trace element approaches, *Geochim. Cosmochim. Acta*, v.42, p.725-741.

Hart, S.R., W.E. Glassley, and D.E. Karig, 1972, Basalts and seafloor spreading behind the Mariana island arc, *Earth and Planetary Science Letters*, v.15, p.12-18.

Hawkins, J.W., 1974, Geology of the Lau Basin, a marginal sea behind the Tonga Arc, in Burke, C., and C. Drake, eds., *Geology of Continental Margins*, Springer-Verlag, Berlin, p.505-520.

Hawkins, J.W., and R. Batiza, 1975, Tholeiitic basalt from an active spreading center on the North Fiji Plateau $15^{o}30'$S, $173^{o}30'$E, *EOS Trans. Amer. Geophys. Union*, v.56, p.1078.

Hawkins, J.W., and J.T. Melchior, 1985, Petrology of Mariana Trough and Lau Basin basalts, *J. Geophys. Res.*, v.90, p.11431-11468.

Hofmann, A.W., 1988, Chemical differentiation of the Earth: the relationship between mantle, continental crust and oceanic crust, *Earth and Planetary Science Letters*, v.90, p.297-314.

Jaques, A.L., and D.H. Green, 1980, Anhydrous melting of peridotite at 0-15 kbar pressure and the genesis of tholeiitic basalts, *Contrib. Mineral. Petrol.*, v.73, p.287-310.

Johnson, T., and P. Molnar, 1972, Focal mechanisms and plate tectonics of the southwest Pacific, *J. Geophys. Res.*, v.77, p.5000-5032.

Klein, E.M., and C.H. Langmuir, 1987, Ocean ridge basalt chemistry, axial depth, crustal thickness and temperature variations in the mantle, *J. Geophys. Res.*, v.92, p.8089-8115.

Krause, D.C., 1973, Crustal plates of the Bismarck and Solomon Seas, in *Oceanography of the South Pacific 1972*, comp. R. Fraser, New Zealand National Commission for UNESCO, Wellington.

Kushiro, I., 1969, The system forsterite-diopside-silica with and without water at high pressures, *Amer. J. Sci.*, v.267, p.269-294.

Kushiro, I., 1972, Effect of water on the composition of magmas formed at high pressures, *J. Petrol.*, v.13, p.311-334.

Langmuir, C.H., and J.F. Bender, 1984, The geochemistry of oceanic basalts in the vicinity of transform faults: observations and implications, *Earth and Planetary Science Letters*, v.69, p.107-127.

Langmuir, C.H., and G.N. Hanson, 1980, An evaluation of major element heterogeneity in the mantle sources of basalts, *Phil. Trans. R. Soc. Lond.*, v.297, p.383-407.

Malahoff, A., and D.R. Bracey, 1974, Crustal evolution of the Bismarck Sea, *EOS Trans. Amer. Geophy. Union*, v.55, p.676.

Mallonee, R., 1989, *Extensional responses to transtension in the Manus Backarc*, M.S. Thesis, University of Hawaii, Honolulu, p.

Mattey, D., B. Marsh, and J. Tarney, 1981, The geochemistry, mineralogy and petrology of basalts from the West Philippine and Parece Vela basins and from the Palau-Kyushu and West Mariana ridges, Deep Sea Drilling Project leg 59, *Init. Rep. Deep Sea Drill. Proj.*, v.59, p.753-800.

McKenzie, D., and M.J. Bickle, 1988, The volume and composition of melt generated by extension of the lithosphere, *J. Petrol.*, v.29, p.625-679.

Mysen, B.O., and A.L. Boettcher, 1975, Melting of a hydrous mantle, I, Phase relations of natural peridotite at high pressures and temperatures with controlled activities of water, carbon dioxide and hydrogen, *J. Petrol.*, v.16, p.520-548.

Mysen, B.O., and I. Kushiro, 1977, Compositional variations of coexisting phases with degree of melting of peridotite in the upper mantle, *Amer. Mineral.*, v.62, p.843-865.

Muenow, D.W., N.W.K. Liu, M.O. Garcia, and A.D. Saunders, 1980, Volatiles in submarine volcanic rocks from the spreading axis of the East Scotia Sea back-arc basin, *Earth and Planetary Science Letters*, v.47, p.272-278.

Norrish, K., and B.W. Chappell, 1977, X-ray fluorescence spectrometry, in Zussman,J.,ed., *Physical Methods in Determinative Mineralogy*, 2nd edition, Acad. Press, London, U.K., p.201-272.

Norrish, K., and J.T. Hutton, 1969, An accurate x-ray spectrographic method for the analysis of a wide range of geologic samples, *Geochim. Cosmochim. Acta*, v.33, p.431-451.

Pearce, J.A., 1983, Role of the sub-continental lithosphere in magma genesis at active continental margins, in Hawkesworth, C.J., and M.J. Norry, eds., *Continental Basalts and Mantle Xenoliths*, Shiva, Nantwich, U.K., p.230-249.

Philpotts, A.R., and C.L. Lewis, 1987, Pipe vesicles - an alternate model for their origin, *Geology*, v.15, p.971-974.

Perfit, M.R., and D.J. Fornari, 1983, Geochemical studies of abyssal lavas recovered by DSRV Alvin from Eastern Galapagos Rift, Inca Transform, and Ecuador Rift 2. Phase chemistry and crystallization history, *J. Geophys. Res.*, v.88, p.10530-10550.

Ripper, D., and K.F. McCue, 1983, The seismic zone of the Papuan fold belt, *BMR J. Austr. Geol. Geophys.*, v.8, p.147-156.

Roeder, P.L., and R.F. Emslie, 1970, Olivine-liquid equilibrium, *Contrib. Mineral. Petrol.*, v.29, p.275-289.

Simkin, T., and J.V. Smith, 1970, Minor-element distribution in olivine, *J. Geol.*, v.78, p.304-325.

Sinton, J.M., and P. Fryer, 1987, Mariana Trough lavas from 18°N: Implications for the origin of back-arc basin basalts, *J. Geophys. Res.*, v.92, p.12782-12802.

Sinton, J., L. Liu, B. Taylor, and B. Chappell, 1986, Petrology, magmatic budget, and tectonic setting of Manus Back-Arc Basin lavas, *EOS Trans. Amer. Geophys. Union*, v.67, p.377.

Sinton, J.M., R.C. Price, K.T.M. Johnson, H. Staudigel, and A. Zindler, 1987, Petrology and geochemistry of submarine lavas from the Lau and North Fiji Back-Arc Basins, *Circum-Pacific Council for Energy and Mineral Resources Earth Science Series*, in press.

Sinton, J.M., D.S. Wilson, D.M. Christie, R.N. Hey, and J.R. Delaney, 1983, Petrological consequences of rift propagation on oceanic spreading ridges, *Earth and Planetary Science Letters*, v.62, p.193-207.

Stolper, E., 1980, A phase diagram for mid-ocean ridge basalts: preliminary results and implications for petrogenesis, *Contrib. Mineral. Petrol.*, v.74, p.13-27.

Takahashi, E., and I. Kushiro, 1983, Melting of a dry peridotite at high pressures and basalt magma genesis, *Amer. Mineral.*, v.68, p.859-879.

Tarney, J., A.D. Saunders, and S.D. Weaver, 1977, Geochemistry of volcanic rocks from the island arcs and marginal basins of the Scotia Sea region, in Talwani, M., and W.C. Pitman, eds., *Island Arcs, Deep Sea Trenches and Back-arc Basins*, *Amer. Geophys. Union*, Washington, p.367-377.

Tatsumi, Y., D.L. Hamilton, and R.W. Nesbitt, 1986, Chemical characteristics of fluid phase released from a subducted lithosphere and origin of arc magmas: evidence from high-pressure experiments and natural rocks, *J. Volc. Geotherm. Res.*, v.29, p.293-309.

Taylor, B., 1979, Bismarck Sea: Evolution of a back-arc basin, *Geology*, v.7, p.171-174.

Taylor, B., and G.D. Karner, 1983, On the evolution of marginal basins, *Rev. Geophys. Space Physics*, v.21, p.1727-1741.

Taylor, B., R. Mallonee, K. Crook, and J. Sinton, 1987, The Manus microplate, *EOS Trans. Amer. Geophys. Union*, v.68, p.1476.

Taylor, B., J. Sinton, and K. Crook, 1986, Extensional Transform Zone, Sulphide Chimneys and Gastropod Vent Fauna in the Manus Back-Arc Basin, *EOS Trans. Amer. Geophys. Union*, v.67, p.377.

Taylor, B., J. Sinton, L. Liu, and K. Crook, 1986, Extensional Transform Zone, Manus Back-Arc Basin, *EOS Trans. Amer. Geophys. Union*, v.67, p.1228.

Toksov, M.N., and P.Bird, 1977, Formation and evolution of marginal basins and continental plateaus, in Talwani, M., and W.C. Pitman, eds., *Island Arcs, Deep Sea Trenches and Back-arc Basins, Amer. Geophys. Union*, Washington, p.367-377.

Vogt, P.R., and G.L. Johnson, 1975, Transform faults and longitudinal flow below the midoceanic ridge, *J. Geophys. Res.*, v.80, p.1399-1428.

Walker, D., T. Shibata, and S.E. DeLong, 1979, Abyssal tholeiites from the Oceanographer Fracture Zone, II, Phase equilibria and mixing, *Contrib. Mineral. Petrol.*, v.70, p.111-125.

Watts, A.B., J.K. Weissel, and R.L. Larson, 1977, Sea-floor spreading in marginal basins of the western Pacific, *Tectonophysics*, v.37, p.167-181.

Williams, H., F.J. Turner, and C.M. Gilbert, 1982, *Petrography: an introduction to the study of rocks in thin sections*, W.H. Freeman and Company, San Fransisco, p.40.

Wright, T.L., and P.C. Doherty, 1970, Linear programming and least squares computer method for solving petrologic mixing problems, *Geol. Soc. Amer. Bull.*, v.81, p.1995-2008.

Wyllie, P.J., 1979, Magmas and volatile components, *Amer. Mineral.*, v.64, p.469-500.

Yoder, H.S., Jr., and C.E. Tilley, 1962, Origin of basalt magmas: an experimental study of natural and synthetic rock systems, *J. Petrol.*, v.3, p.342-532.